

University of Groningen

The Cosmic-Ray Dominated Midplane of Protoplanetary Disks

Chaparro Molano, German

IMPORTANT NOTE: You are advised to consult the publisher's version (publisher's PDF) if you wish to cite from it. Please check the document version below.

Document Version

Publisher's PDF, also known as Version of record

Publication date:

2013

[Link to publication in University of Groningen/UMCG research database](#)

Citation for published version (APA):

Chaparro Molano, G. (2013). The Cosmic-Ray Dominated Midplane of Protoplanetary Disks: The Solar System Connection. Groningen: s.n.

Copyright

Other than for strictly personal use, it is not permitted to download or to forward/distribute the text or part of it without the consent of the author(s) and/or copyright holder(s), unless the work is under an open content license (like Creative Commons).

Take-down policy

If you believe that this document breaches copyright please contact us providing details, and we will remove access to the work immediately and investigate your claim.

Downloaded from the University of Groningen/UMCG research database (Pure): <http://www.rug.nl/research/portal>. For technical reasons the number of authors shown on this cover page is limited to 10 maximum.



rijksuniversiteit
 groningen

**The Cosmic-Ray Dominated Midplane
 of Protoplanetary Disks
 The Solar System Connection**

Proefschrift

ter verkrijging van het doctoraat in de
 Wiskunde en Natuurwetenschappen
 aan de Rijksuniversiteit Groningen
 op gezag van de
 Rector Magnificus, dr. E. Sterken,
 in het openbaar te verdedigen op
 vrijdag 17 mei 2013
 om 11.00 uur

door

Germán Chaparro Molano
 geboren op 6 augustus 1984
 te Bogotá, Colombia

Promotor:

Prof. dr. I. Kamp

Beoordelingscommissie:

Prof. dr. H. Linnartz

Prof. dr. T. Millar

Prof. dr. M. Spaans

ISBN 978-90-367-6244-1

ISBN 978-90-367-6245-8 (electronic version)

*Uno, busca lleno de esperanzas
el camino que los sueños
prometieron a sus ansias.
Sabe que la lucha es cruel
y es mucha, pero lucha y se desangra
por la fe que lo empecina...*

Enrique Santos Discépolo,
Uno (Tango de Mariano Mores)

A las tres mujeres de mi vida,
Adriana, Mary, Violeta.
Tanto amor.

Image and cover design by Adriana García Gaitán
www.adriana-garcia.com

©2013 G. Chaparro Molano

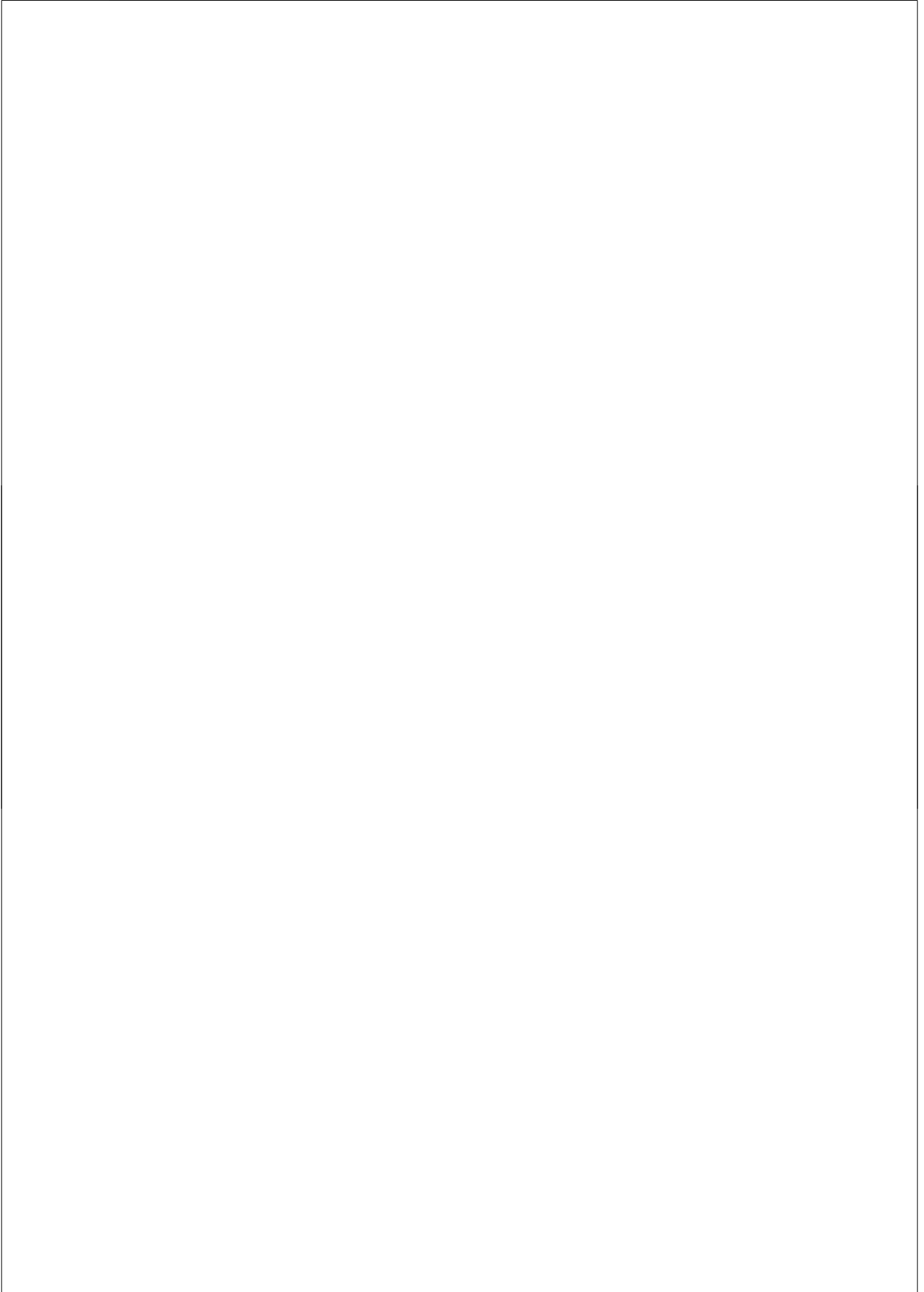
Contents

1	Introduction	1
1.1	Formation of the Solar System	2
1.1.1	From dust to planets	4
1.1.2	Meteorites and comets	6
1.1.3	The minimum mass solar nebula	7
1.2	Observations of disks	8
1.2.1	Accretion rate and the ages of disks	10
1.2.2	Dust in protoplanetary disks	11
1.2.3	Spectral Energy Distributions	12
1.2.4	General classification of young stars	15
1.3	Disk models	16
1.3.1	Vertical density structure	16
1.3.2	Gravitational stability of the disk	20
1.3.3	Radial temperature structure	20
1.3.4	Dust temperature	22
1.3.5	Rotational speed of the gas	23
1.3.6	Mechanism for accretion	24
1.3.7	Evolution of an accretion disk	25
1.4	Chemistry in disks	26
1.4.1	Time-dependent chemistry	28
1.5	Cosmic rays	30
1.5.1	Cosmic ray-induced UV photons	31
1.6	This thesis	33
2	The role of OH in the chemical evolution of protoplanetary disks I. The comet-forming region	35

Contents

2.1	Introduction	37
2.2	Disk Model	39
2.3	Cosmic rays	42
2.3.1	Impact on chemistry	42
2.3.2	Cosmic ray-induced UV photon flux	44
2.3.3	Cosmic ray-induced UV photodissociation	46
2.4	Chemical model	47
2.4.1	Adsorption	48
2.4.2	Desorption	49
2.5	Gas-grain chemistry model	52
2.5.1	Initial conditions	53
2.5.2	Chemistry benchmarking at 1 AU	54
2.6	Chemistry in the comet-formation zone	54
2.6.1	Chemical pathways	54
2.6.2	The effect of CRUV enhancement	60
2.7	Alternative H ₂ O photodesorption mechanism	62
2.8	Discussion	63
2.8.1	Implications for comet formation	63
2.9	Conclusions	65
3	The role of OH in the chemical evolution of protoplanetary disks II. Gas-rich environments	67
3.1	Introduction	69
3.2	Methodology	71
3.3	Gas-rich regions	71
3.4	Cosmic-ray-induced processes	74
3.4.1	CRUV emission probability profile	76
3.4.2	CRUV gas opacity	77
3.5	Chemical model	79
3.6	Results	80
3.6.1	Chemistry at 1 AU	83
3.6.2	Chemistry at 3-5 AU	89
3.6.3	Chemistry at 7-8 AU	90
3.7	Discussion	90

3.7.1	The role of OH	92
3.7.2	Survival of SiO in the $A_V = 1$ region	93
3.8	Conclusions	94
	Appendix: Cross-section data	96
4	Chemical evolution of the cosmic-ray dominated midplane of protoplanetary disks	99
4.1	Introduction	101
4.2	Cosmic-ray-induced UV photoprocesses	102
4.3	Model description	115
4.4	Results	116
4.4.1	Time dependent models	116
4.4.2	Comparison with Model SS	121
4.4.3	Disk ice content	122
4.5	Conclusions	123
	Appendix: Jacobian for CRUV photoprocesses	127
5	Modeling the layering of ices in protoplanetary disks	131
5.1	Introduction	133
5.2	Spherical dust grain growth	135
5.3	Model	137
5.4	Results	138
5.5	Conclusions	139
	Nederlandse Samenvatting	145
	Resumen en Español	153
	Acknowledgments	167



1

Introduction

*Inevitably the myths woven by us, though they contain error,
will also reflect a splintered fragment of the true light, the eternal truth.*
— J.R.R. Tolkien —

The most conspicuous clue toward unraveling the mystery of the formation of the Solar System is the fact that the orbits of planets are largely co-planar, rotating all in the same direction. This commonality suggests that the primordial matter that clumped into planets had a thin, rotating disk-like shape. But how does the formation of the Sun fit with the formation of the planets?

Dating of Solar System bodies together with current observations of young stars suggests that the Sun must have formed at the same time as the primordial disk. This means that the Sun and its planets share a common origin: a primordial, tens of light-years across, millions of solar masses heavy, *molecular cloud* made of gas and dust. The gravitational collapse of a fragment of this cloud gave birth to the Sun along with its circumstellar disk, which later evolved into the Solar System as we know it. This model for the formation of the Solar System is historically known as the *nebular hypothesis*. The name comes from the theory developed by Swedenborg, Kant and Laplace in the 18th century (Woolfson 1993), who argued that the collapse of a single nebula could have given birth to the Solar System.

1. Introduction

In general, observations of young stars with their own circumstellar, or *protoplanetary* disks suggest that this formation process is not unique to our Solar System. Solar-mass stars surrounded by a disk are conventionally known as *T Tauri stars*. Generally, a young star surrounded by μm - to mm-sized dust will show an infrared (IR) excess which extends to sub-mm observations. Most T Tauri stars show strong $\text{H}\alpha$ emission, which is an optical tracer of active accretion of gas from the protoplanetary disk onto the stellar surface (Calvet & Hartmann 1992). The accretion luminosity can be related to the mass accretion rate \dot{M} (Gullbring et al. 1998), which yields values in the range of $10^{-7} - 10^{-9} M_{\odot}/\text{yr}$, corresponding to actively accreting disks and passive disks, respectively.

It is often convenient to think about the gas and dust in the disk as two separate phases of matter, without worrying too much about the chemical composition of the disk. However, this simplification keeps us away from understanding many details that link protoplanetary disk research with the formation and chemical composition of the Solar System. Thus, we can weave together the theories and observations of the chemical and physical evolution of protoplanetary disk along with Solar System research into a formation model for the Solar System.

1.1 Formation of the Solar System

In the last 30 years, the improvement of observations of young stars together with data from decades of Solar System exploration have led to the refinement of our theories of formation and evolution of the Solar System (Cameron 1995; Fegley 2000). The formation of the Solar System was a gradual process, which took about 10^7 yr (Stahler & Palla 2005). It started with a molecular cloud fragment that became gravitationally unstable and collapsed isothermally under its own gravitational pull (Shu et al. 1987). The gravitational potential energy that must be disposed of in order to achieve this collapse heated up the gas at the center of the previously starless cloud and formed the proto-Sun. In this early stage, the Sun was not a star yet, but a first core, with a mass M of about $5 \times 10^{-2} M_{\odot}$ and a radius R of about 5 AU. Its temperature was set by the balance between the thermal and gravitational potential energy given by the virial theorem, $U_{\text{grav}} = -2U_{\text{therm}}$:

$$-\frac{3}{5} \frac{GM^2}{R} = -2 \frac{3}{2} \frac{kTM}{\mu m_{\text{H}}}. \quad (1.1)$$

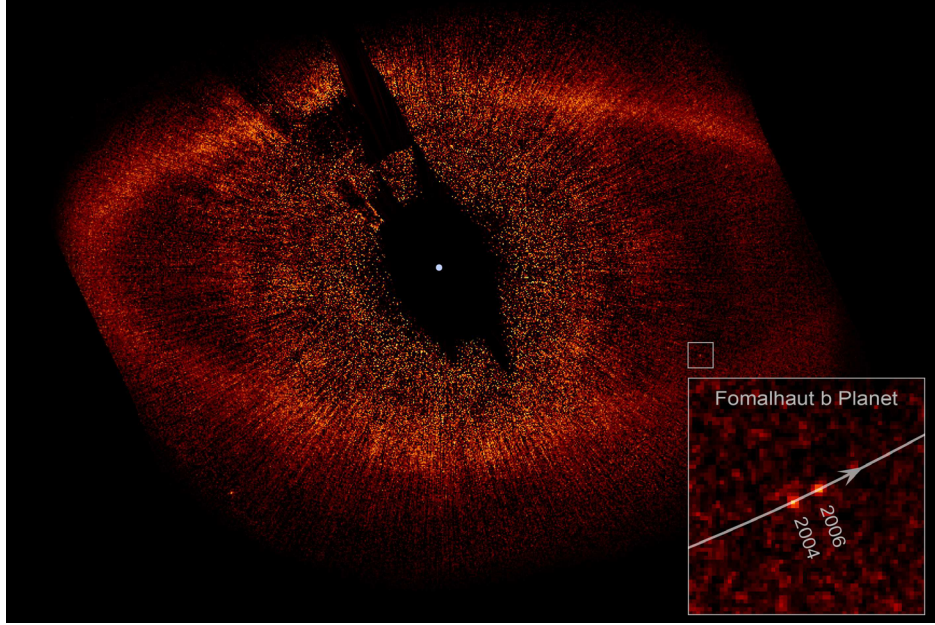


Figure 1.1: Coronagraph of the debris disk and planet orbiting Fomalhaut (Image credit: ESA).

Here $\mu \approx 2.4$ is the mean molecular weight of the gas. For these values, the temperature of the core can be estimated to be:

$$T \approx 520 \text{ K} \left(\frac{M}{5 \times 10^{-2} M_{\odot}} \right) \left(\frac{R}{5 \text{ AU}} \right)^{-1}. \quad (1.2)$$

This core was completely obscured by an envelope of dust and gas, hundreds of AU wide, which still served as the mass reservoir for building up the Sun. As mass accretion continued, the gravitational energy of the collapse generated temperatures of the order of 2000 K, which is the critical temperature at which molecular hydrogen in the gas is collisionally dissociated. This slowed down the core growth while creating an inner reservoir of atomic hydrogen. After this, the core expanded until it became unstable again, which led to a second collapse. When the core density reached the critical density value of $\rho \sim 0.01 \text{ g/cm}^{-3}$, hydrogen could be ionized, and the core became optically thick. At this point, the accretion and internal luminosity supported the core against the gravitational contraction and it became a *protostar*.

In general the net angular momentum of a collapsing cloud is nonzero, which

1. Introduction

means that all the material that did not reside close to the axis of rotation of the cloud did not immediately fall to the center of the collapse. Leftover material from the initial collapse then became part of a thick, enveloping disk. Thermal and radiative stellar winds driven by accretion events (Davis & Eisloffel 1995; Evans et al. 2009) generated outflows that carved away the envelope in a timescale of $10^4 - 10^5$ yr, leaving behind a thin accreting disk. At this point, the Sun is considered to be a *pre-main-sequence* star, characterized by the fact that its energy budget comes from gravitational contraction and not from H burning. As soon as the Sun was able to ignite H burning it became a Main Sequence star.

After the thick envelope was gone, radiation from the Sun heated up the gas in the disk surface until the gas thermal velocity was higher than the escape velocity at its location, which caused it to dissipate. This process, known as *photo-evaporation* is driven by stellar X-rays (Gorti & Hollenbach 2009), EUV in the inner disk (Hollenbach et al. 1994), and FUV in the outer disk (Gorti & Hollenbach 2008). The estimated mass-loss rate for gas dispersal ranges from 10^{-8} to $10^{-10} M_{\odot}/\text{yr}$, approximately 100 times lower than estimated mass accretion rates (Hartigan et al. 1995). Currently, there is no consensus that photoevaporation was the main cause of gas dispersal for the Solar System. In general, it is only one of several possibilities: stellar winds, external winds, interaction with planets (Machida et al. 2006), Magneto-Hydrodynamical (MHD) turbulences (Suzuki & Inutsuka 2009) are also likely candidates.

After the gas dissipated, leftover dust and debris were in the process of growing into planets. At this evolutionary stage, the disk is called a *debris disk*. In fact, fully-formed exoplanets have been observed immersed in debris disks (Kalas et al. 2008), as Fig. 1.1 shows.

1.1.1 From dust to planets

Finding a solution to the problem of how to grow planets from the primordial dust and gas in the disk is limited mostly by observations (Henning 2008). Even though μm and sub-mm dust can be observed in the infrared and Earth-sized exoplanets can be detected by direct imaging (Kalas et al. 2008), radial velocity measurements (Bouchy et al. 2005), and transits (Agol et al. 2005) (among other methods), the intermediate stages of planet formation are virtually undetectable. Current models of grain growth and planet formation are largely based on laboratory experiments (Blum 2010) and theoretical considerations (Greenberg et al. 1991; Dominik et al. 2007).

Dust in the primordial disk is able to grow by a process known as *coagulation*, in

1.1 Formation of the Solar System

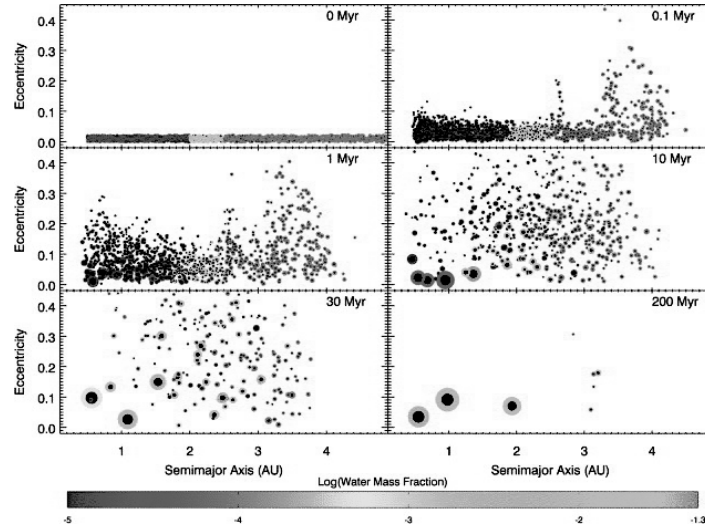


Figure 1.2: Evolution of a simulation of terrestrial planet formation. The color of each body shows its water content, and the dark circle inside each body shows the size of its iron core. At the end of the simulation, a water-rich 2 Earth-mass planet has formed at 0.98 AU in the habitable zone. Figure and (modified) caption from Raymond et al. (2006).

which dust particles agglomerate thanks to microscopic adhesion forces after slow collisions, typically of the order of 1 m/s (Blum 2010). This process combined with *dust settling*, in which dust initially located above the plane of rotation of the disk drifts vertically toward this plane, initiates the growth of micron-sized particles into meter-sized bodies (Ormel et al. 2010). If dust settling is taking place, local gravitational instabilities can accelerate the process of coagulation (Goldreich & Ward 1973), which leads to the formation of kilometer-sized objects known as *planetesimals*, which are the building blocks of planets.

The collision cross-section for large planetesimals ($r > 10$ km) is enhanced due to their gravitational field. This enhancement is known as *gravitational focusing*. At this stage, a process known as *runaway growth* takes place, where large seed bodies ($r > 10$ km) are formed from the coalescence of smaller planetesimals. These seed bodies then experience *oligarchic growth*, where larger bodies grow faster than smaller bodies, forming Earth-sized ($r \sim 1000$ km) rocky planets. The gravitational sphere of influence of a rocky planet is defined by the Hill radius:

$$r_{\text{Hill}} = \left(\frac{m}{3M} \right)^{1/3} r. \quad (1.3)$$

1. Introduction

Here r is the radial distance to the Sun, and m , M are the masses of the seed planet and the Sun, respectively. The *feeding zone* is then defined as the annulus (ring-like segment) in which small planetesimals are accreted onto the seed planet (Greenberg et al. 1991). At distances below the critical radius where the disk temperature is high enough to prevent the formation of ices¹, pure rocky planets such as the Earth are formed. Figure 1.2 shows the results of a simulation of the formation of terrestrial planets from ~ 0.1 Earth mass planetesimals (Raymond 2006). For seed planets located outside the snow line, the scale height of the disk at the orbital radius is larger, and therefore they can accrete more mass than rocky planets, reaching masses of the order of 10 Earth masses. For such massive seed planets, further accretion of gas located within the feeding zone onto the seed planet leads to the formation of the gaseous Jovian planets. In general, planets can form while dynamically clearing the dust on a timescale of up to a few 100 Myr.

1.1.2 Meteorites and comets

Meteorites and comets are Solar System bodies that were originally part of the protoplanetary disk from which planets were formed. However, for them the process of growth from dust to planets stopped before they were able to form a larger object.

Meteorites can be broadly classified in three classes, according to their composition: Stony, Iron, and Stony-Iron meteorites (Shaw 2006). Stony meteorites are by far the most common type (80 – 90%) followed by Iron (4 – 20%). Stony meteorites in turn are divided into two major subclasses, chondritic or achondritic. The term *chondritic* refers to the presence of *chondrules*, which are primordial silicate dust aggregates that experienced thermal processing ($T \approx 1600$ K) during their formation, and range in size from a few μm to ~ 1 cm. Some chondritic meteorites also contain phyllosilicate clays, which are interpreted as evidence of a process called *aqueous alteration*, in which the exposure of chondrules to high water vapor pressures forms phyllosilicates on the exposed area (Bischoff 2001). Such evidence of high water vapor pressure and high temperatures during their formation, along with few signs of posterior chemical processing suggest that chondrules were formed in the Solar protoplanetary disk. Thus, the presence of chondrules in a meteorite suggests that they did not experience further thermal processing, and remained freely-floating objects during and after the formation of the Solar System. On the other hand, Achondritic and Iron meteorites show signs of thermal processing and differentiation, which means that their origin is the fragmentation of a larger parent body, such as a planet

¹This region is also known as the *snow line*, which for the Solar System is located at distances of about 4 AU from the Sun.

1.1 Formation of the Solar System

or a large asteroid.

An important sub-class of chondritic meteorites are *carbonaceous* chondrite meteorites, which contain a rich variety of organic compounds (~2% by mass in the Murchison meteorite), forming a layer between chondrules. These meteorites also show calcium- and aluminium-rich inclusions, which were formed at very high temperatures ($T > 2400$ K). Isotope dating of these inclusions show that they cooled down at a very early stage of the Solar System formation, and a few million years before chondrules were formed (Amelin et al. 2002). This suggests that they are some of the earliest remnants of the original collapse that gave birth to the Solar System. Dust which can be dated to an even earlier epoch before the primordial collapse is known as *presolar dust*. This type of dust has been found in meteorites (Lodders & Amari 2005), although its chemical composition shows that it is not representative of interstellar dust (Li & Mann 2012). This suggests that most interstellar dust in the parent cloud was chemically altered during the collapse phase.

Comets are similar in mineral composition as some chondritic meteorites, but they also contain ices such as H₂O, CO, CO₂, and many organic species. Because of their ice content, it is thought that they were formed beyond the snow line of the Solar protoplanetary disk, near the current Jupiter orbit. Earth- and space-based measurements of the composition of cometary ices show a very good correlation with the corresponding interstellar abundances (Bockelée-Morvan 2010). However, this correlation breaks down for CO₂ and CH₄, which are species that are detected in comets and are not very abundant in the interstellar medium. This, along with isotope dating of cometary matter sampled by the Stardust mission (McKeegan et al. 2006), rules out an interstellar origin for comets. However, the question of whether cometary ices are formed first in the gas phase and then adsorbed onto the primordial dust or are entirely a product of surface chemical reactions by radicals (A'Hearn et al. 2012), remains open.

1.1.3 The minimum mass solar nebula

If we picture the birth of our Solar System as I described it, with a circumstellar disk remaining after the original cloud has collapsed into a star, we can construct a simple yet sturdy model for estimating the mass of the early disk surrounding the Sun from the current state of the planets of the Solar System. The resulting model from this procedure is called the Minimum Mass Solar Nebula (MMSN) (Weidenschilling 1977), even though it is not a nebula at all, but a disk.

We would first form a disk that is composed of 8 annuli where each of them corre-

1. Introduction

sponds to the feeding zone of a planet (Section 1.1.1), delimited by the orbital separation of the planets up to the orbit of Neptune². Thus, the center of the first annulus would be located roughly at the orbital radius of Mercury (0.3 AU) and would extend to halfway between Mercury and Venus (0.5 AU). This means that the inner radius of this annulus would be located at 0.1 AU. If we were to give each annulus the mass of each planet, the density distribution would be very discontinuous. This is because only heavy elements remain when the rocky planets are forming. To compensate this effect, we correct for the light element abundances that did not participate in the coagulation of solids in the case of rocky planets and only partially for the gas and ice giants. The amount of matter added to each annulus is in proportion to the Solar abundances of the elements.

The reconstructed surface density of the resulting disk follows a power law (for $0.1 \text{ AU} < r < 30 \text{ AU}$) that yields a disk mass of $0.01 M_{\odot}$ (Hayashi 1981):

$$\Sigma(r) = 1700 \left(\frac{r}{1 \text{ AU}} \right)^{-1.5} \text{ g cm}^{-2} . \quad (1.4)$$

Even though the MMSN model yields very valuable information about the amount of mass (and its distribution) that we can expect in other protoplanetary disks, it has many issues that limit its use. One of such limitations is its incompatibility with planetary migration scenarios such as the one proposed in the Nice model (Tsiganis et al. 2005; Morbidelli et al. 2005; Gomes et al. 2005). A denser MMSN disk with a steeper power law such as the one proposed by Desch (2007) might give a better estimate, although its compatibility with the Nice model is still under question, as planet-disk interactions for Jovian planets would cause them to fall towards the Sun (Crida 2009).

1.2 Observations of disks

In 1983, the Infra-Red Astronomical Satellite (IRAS) was the first large-scale attempt to observe galactic and extragalactic sources that were strong in the infrared. From this survey, a few young stars showed a strong infrared excess, which was hypothesized to be caused by a shroud of warm, μm -sized dust surrounding the stars.

One of the first stars to have their IR excess interpreted as a signature of a disk of circumstellar dust was β Pictoris. In 1984 it became the first star to have its disk observed optically (Smith & Terrile 1984) at the Las Campanas Observatory in Chile.

²Sorry, Pluto.

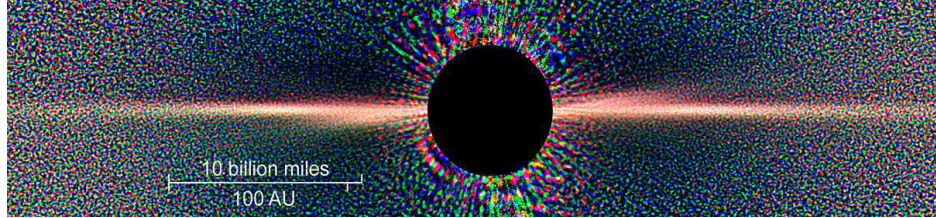


Figure 1.3: Hubble Space Telescope image of the β Pic circumstellar disk (Image credit: ESA).

Before achieving direct imaging of circumstellar disks the suspicion was that only a disk-like geometry could explain the characteristic IR signature of these stars, although a consensus was not reached³.

More observations of young, solar-mass stars endowed with circumstellar disks showed that β Pic was representative of gas-poor, debris disks. On the other hand, stars with gas-rich circumstellar disks were found to be their younger counterparts, now known as T Tauri stars. T Tauri stars show a much stronger IR excess, which is explained by the presence of a massive circumstellar disk of gas and dust. In these stars extinction is always larger in the optical than in the IR. Since the disk is geometrically thin, the extinction in the optical in the line of sight towards the star is low; however, the material in the disk is optically thick (high extinction) and intercepts a fraction of the stellar light (depending on the height of the inner rim and on how large the flaring angle is), absorbs it and re-emits it at IR wavelength. This re-emission occurs at all angles and so we receive as observers IR emission into our line of sight. In these sources we can see the star in the visual almost as clearly as if the material causing the IR excess was not there at all. This is only possible when the material is not isotropically distributed around the star, but in a flat disk-like shape.

The object known as T Tauri has since become the prototype for all pre-main-sequence, solar-mass stars surrounded by a disk of dust and gas. It is one of many such stars found in Taurus-Auriga, a star forming region located at a distance of 140 pc. Besides T Tauri stars, this region also shows objects known as *dark clouds*, only seen in the far IR. Dark clouds which suspected to harbor protostars in their center are known as *hot corinos*: the infrared signature of obscuring material being heated by a star gives them away. On the other hand, Herbig Ae/Be stars are similar to T

³After all, in 1984 there were only four stellar sources (including β Pic) suspect of having circumstellar dust.

1. Introduction

Table 1.1: Characterizing the protoplanetary disk with observations

Type of Observation	What it measures
Infrared emission (continuum)	Signature of disk and envelope: warm dust near the star (300-1000 K).
Direct optical imaging	Shape of the surface of the disk.
H α , Br γ , He line emission	Presence of gas accretion activity.
High energy radiation	FUV and X-rays are signatures of accretion events near the stellar surface, stellar activity and funnel flows.
Millimeter/sub-mm (continuum)	Optically thin, cold dust (10-30 K) in the outer disk, beneath the disk surface.
Sub-mm line emission	Measure the disk rotation and probe the vertical disk structure (^{12}CO , ^{13}CO).
IR emission lines	Probe chemical activity on the disk surface (CO, HCN, C $_2$ H $_2$, OH, H $_2$ O, CO $_2$, etc.).
10 and 20 μm silicate feature	Probes of the sizes of warm silicate dust located on top of the continuum emitting dust on the disk surface.
PAH line emission	UV excited Polycyclic Aromatic Hydrocarbons (PAHs) emit in IR via stretching and bending of their carbon chains (Kamp 2011).
69 μm forsterite feature	Probes the temperature of iron-poor crystalline silicate dust and its iron content.

Tauri stars but heavier ($M > 2M_{\odot}$).

As observations of disks get increasingly more detailed, modelers strive for increasing complexity in the physical and chemical processes in their models. Table 1.1 lists what different observations can tell us about protoplanetary disks.

1.2.1 Accretion rate and the ages of disks

The H α accretion signature in T Tauri stars has been used by Fedele et al. (2010) to estimate the average timescale of gas accretion, i.e. the average lifetime of the gas in the disk. They counted the fraction of stars showing H α accretion lines in individual stellar clusters and plotted this number against the average age of the cluster, which is determined by other means. The results are shown in Fig. 1.4. It is clear that after 10

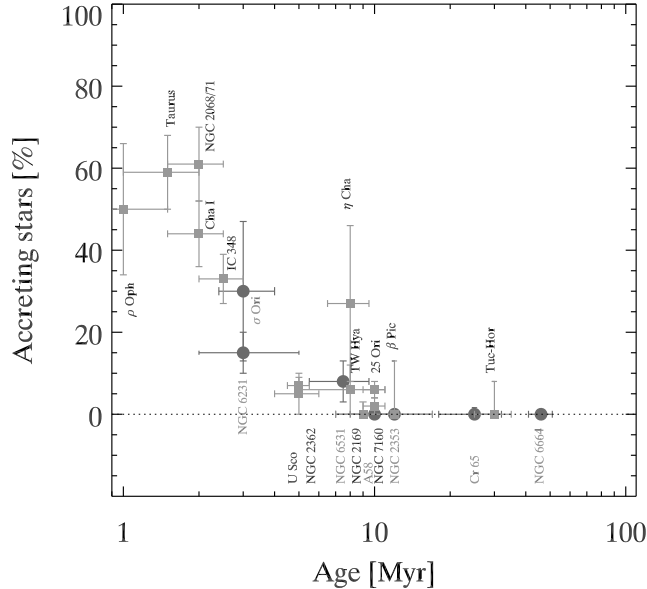


Figure 1.4: Fraction of accreting stars per cluster as a function of age. Figure taken from Fedele et al. (2010).

million years the gas has dissipated from the innermost regions of the disk. ISO and Spitzer surveys of the fraction of stars with near-IR excess in clusters, which traces the dust in the inner disk (Hernández et al. 2008), together with sub-mm observations showing evidence of disk dispersal of dust in the outer disk (Williams & Cieza 2011) seem to agree with this figure.

1.2.2 Dust in protoplanetary disks

Circumstellar dust is very efficient at absorbing stellar radiation. This causes it to get warm (300-1000 K), and to re-emit some of its newly-acquired thermal energy in the near- to mid-infrared (1-8 μm) according to Wien's displacement law. Emission at these wavelength is dominated by grains of a few μm in size. The reason is that for spherical dust grains, the Mie theory predicts that the dust emissivity ϵ is almost 1 for wavelengths smaller than the size of the dust, and it goes as λ^{-1} for longer wavelengths (Tielens 2005). This means that the near- to mid-IR warm dust signature is emitted preferentially by dust grains larger than a few μm , as shown in Fig. 1.5. Larger grains (mm-sized) contribute much less, as the opacity is dominated by smaller grains by virtue of their higher surface area per volume.

1. Introduction

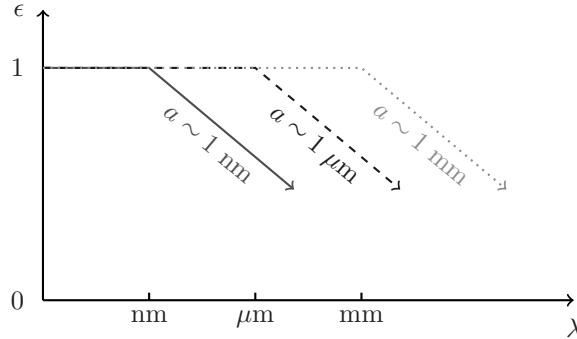


Figure 1.5: Emissivity as a function of wavelength for small, round dust grains of average size 1 nm, 1 μm , and 1 mm.

Using a similar argument we can conclude that the source of millimeter and sub-millimeter emission by colder dust (20 K) is preferentially from millimeter-sized dust. If the protoplanetary disks are optically thin at these wavelengths, the observations are tracing dust that lays beneath the disk surface, possibly down to the disk midplane.

A simple approximation for the dust grain size distribution is to use a power law $f(a) \propto a^{-p}$ over a range $a_{\min} < a < a_{\max}$. The power law index p usually takes a value in the range 2.5–3.5, corresponding to a distribution favoring more large-sized grains or more small-sized grains, respectively. In protoplanetary disks, primordial dust grains are expected to coagulate and grow in size (Dominik et al. 2007; D’Alessio et al. 2001; Blum 2010). For this reason, dust size distributions for protoplanetary disks are modeled using on average larger grains than in molecular clouds. However, the shape of the power law and the exact values for a_{\min} and a_{\max} are unknown for the most part. In general, dust parameters might vary widely from disk to disk, and in some cases vary within a single disk: Isella et al. (2010) spatially resolved the dust in the protoplanetary disks of the young stars RY Tau and DG Tau and found a change in the dust opacity power law index as a function of radius, which is caused by different dust populations in different regions of the disk.

1.2.3 Spectral Energy Distributions

Spectral Energy Distributions (SEDs), are the protoplanetary disk astronomer’s best friend. Unlike in a normal spectrum, flux density is plotted rather than flux in the

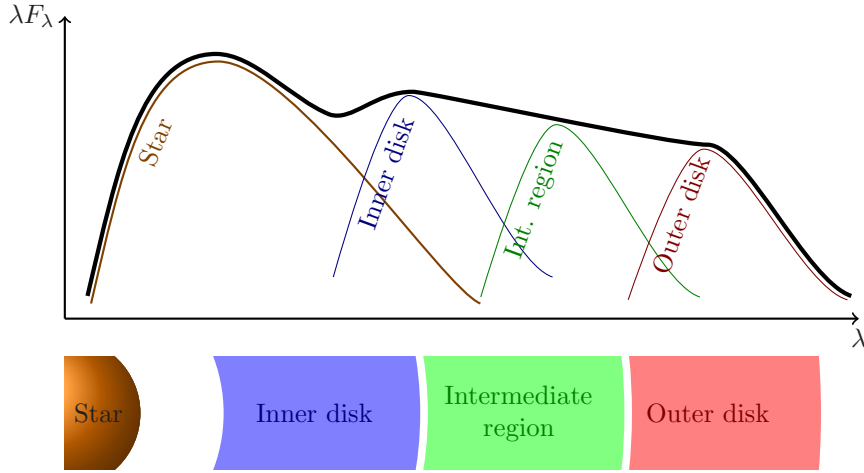


Figure 1.6: Multi-color SED of a protoplanetary disk+star.

vertical axis. The reason is that the flux density λF_λ measures the energy per wavelength (or frequency) interval, showing the main black body temperature components of the source in a comparable way. The SED of a star without a disk would show only the black body spectrum of the star, whereas the SED of an embedded protostar only shows the emission from a cold black body (the dust completely hiding the protostar). For a T Tauri star, two main components are seen: the black body emission of the star and the black body emission of the protoplanetary disk. The disk component of the SED of a T Tauri star is not that of a single temperature black body because the circumstellar material is radiating at different temperatures depending on the distance of the material from the central star.

Let us consider how the different temperature components of the disk will contribute to its emission spectrum. To do this, we integrate over the emission of each annuli of the disk at a radius r :

$$F_\lambda = \int_{r_{\text{in}}}^{r_{\text{out}}} I_\lambda(T_{\text{disk}}(r)) r dr . \quad (1.5)$$

If the emitting region of each annuli behaves like a black body at a temperature $T_{\text{disk}}(r)$, we can assume that $I_\lambda = B_\lambda$, where B_λ is the black body spectral radiance. This means that the power spectrum will have three main components:

- **Short wavelengths** The power spectrum corresponds to the black body emission of the inner region of the disk (where $T \simeq T_{\text{disk}}(r_{\text{in}})$), also known as the

1. Introduction

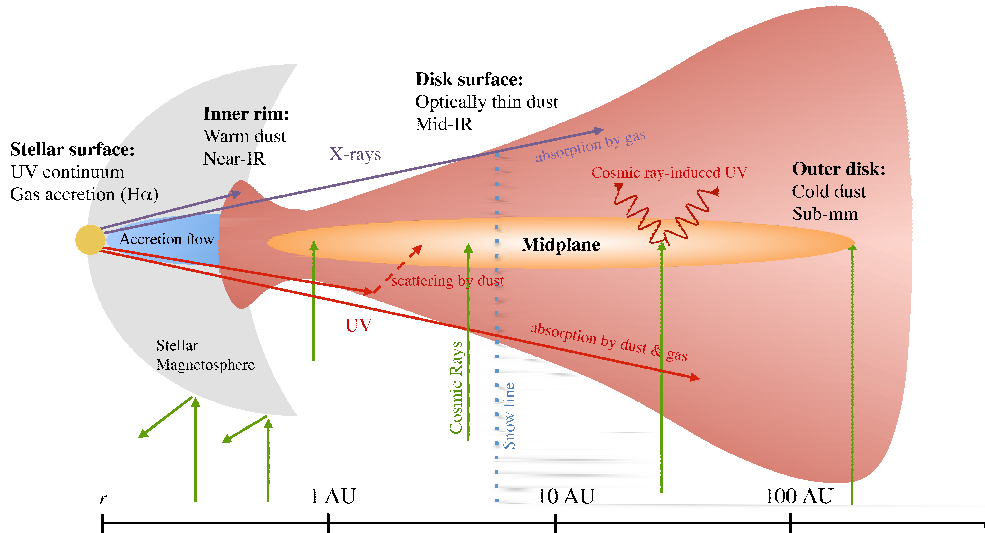


Figure 1.7: Disk structure and main emission features. Figure based on Dullemond & Monnier (2010).

inner rim.

- **Intermediate wavelengths** The shape of the intermediate power spectrum depends on the temperature profile of the disk, and is in general optically thick, i.e. the radiation comes from the disk surface.
- **Long wavelengths** The power spectrum behaves according to the Rayleigh-Jeans law, although the radiation is optically thin, i.e. it comes from deep below the disk surface. This corresponds to sub-mm observations.

Combining those components we obtain the SED of a simple disk model, which shows the overall shape of the IR excess (Figure 1.6). More sophisticated models (see Section 1.3.4) include the contribution of a possibly flaring surface layer (Chiang & Goldreich 1997) fit more closely the SED of actual T Tauri stars.

From the general properties and specific features of the SED, it is possible to reconstruct the structure of a disk from a multi-zone point of view, putting together observations at different wavelengths covering near-IR to mm disk emission (Figure 1.7).

1.2.4 General classification of young stars

The T Tauri phase of a young stellar object is only one step in the evolutionary track that takes an embedded protostar and turns it into a full-fledged planetary system. We define a classification of the different evolutionary stages, even though young stars are so diverse that this task seems foolhardy at times. However, the most widely accepted attempt is known as the Lada classification (Lada 1987), which is based on the assumption that the observed infrared excess in the SED can be used as a rough measure of the evolutionary stage of the system.

For young stars, the SED usually corresponds to a multi-color black body. In other words, there are separate components of the system at different temperatures which can contribute to the power spectrum. A measure of the distribution of the circumstellar material is given by the slope of the infrared excess α_{IR} :

$$\alpha_{\text{IR}} = \frac{d \log(\lambda F_{\lambda})}{d \lambda}. \quad (1.6)$$

Thus, the Lada classification encompasses the typical evolutionary history of most young stars into four (five) separate categories:

- **Class 0.** These deeply embedded protostars cannot be seen at all in the visible spectrum. They are detectable only because of their heavily extinguished far IR signature, typical of a cold black body.
- **Class I.** In these systems the star is visible, but its envelope is still in active infall and shadows a significant part of the stellar emission. Thus, they show a nearly flat IR power spectrum ($-0.3 < \alpha_{\text{IR}} < 0$), corresponding to an extended circumstellar envelope. Outflows are very active in this stage.
- **Class II.** At this stage, the envelope has all but disappeared and the star is perfectly visible, leaving behind an accretion disk which re-emits a significant fraction of the stellar radiation, with plenty of detectable gas and dust. They also show an IR excess, although less pronounced than in Class 0 & I objects ($-1.6 < \alpha_{\text{IR}} < -0.3$). These are what we call *Classical T Tauri Stars* (CTTS). Their SEDs show a multicolor black body power spectrum corresponding to ring-like regions of a circumstellar disk which are at different temperatures.
- **Class III.** Also known as stars with debris disks or *Weak-lined T Tauri Stars* (WTTS), these objects show only a small amount of circumstellar dust and almost no gas left over. Their IR excess is reduced to the contribution of the dust, and as such they show an almost monochromatic black body in their SEDs ($\alpha_{\text{IR}} < -1.6$). These objects are on their way to become

1. Introduction

- **Planetary systems.** These are stars accompanied by their own cohort of planets (that's us!). As the planets have cleared up most of the remaining dust, there is no significant IR excess to be measured.

It should be noted here that this classification is actually a continuum, as the evolution of a protoplanetary disk is not a discrete process. This classification excludes pathological objects such as asymmetric disks or disks with gaps.

1.3 Disk models

In order to understand what protoplanetary disk evolution can teach us about our own Solar System (and vice versa), we need consistent thermo-chemical models for protoplanetary disks. More specifically, if we want to understand the chemistry in the disk we need to understand the hydrodynamic structure of the disk first, as many chemical reactions depend on the local temperature and density conditions in which they take place. Thus, I will give a brief summary of the physical principles that govern the structure of protoplanetary disks. The aim of this is to obtain a temperature and density spatial profile that is consistent with hydrostatic equilibrium. We can then use this disk structure to minimize the amount of assumptions for our further chemical studies.

1.3.1 Vertical density structure

For estimating the vertical density structure we need two assumptions:

- The disk is geometrically thin: observations suggest that the disk cools radiatively very efficiently, which causes pressures which are not high enough to vertically support a geometrically thick disk. Thus, the ratio between the vertical and radial scales is very small.
- The disk is not self-gravitating: the dominant gravitational component is that of the star.

A disk that follows the MMSN prescription (Section 1.1.3) satisfies both of these conditions (Armitage 2010).

A mass element dm located at a height z and a radius r in the disk will feel only two vertical forces, the pressure-gradient force and the vertical component of the stellar gravitational force for a star of mass M :

$$F_G = \frac{GMdmz}{(r^2 + z^2)^{3/2}}, \quad (1.7)$$

Table 1.2: Typical values for the physical properties of different stages of young stars according to the Lada classification, compiled from Stahler & Palla (2005); Visser (2009); Armitage (2010); Kamp & Spaans (2012) unless otherwise noted. Notes: (a) 1 AU values, estimated for a T Tauri disk model with a stellar mass of $1 M_{\odot}$ and a $0.01 M_{\odot}$ disk with a surface density power law index of 1.5, from (Woitke et al. 2009). Data compiled from (b) Teixeira et al. (2007), (c) Maret et al. (2004), (d) Andrews & Williams (2007),

Type	Outer radius	Mass (M_{\odot})	Density (cm^{-3})	Temperature (K)
Parent cloud	10-100 pc	$10^3 - 10^7$	$10^2 - 10^3$	10-20
Starless core	0.3-3 pc	> 50	$10^3 - 10^4$	10-100
Class 0 (Envelope) ^b (Core) ^c	500 AU > 5 AU	> 0.5 0.01	$10^5 - 10^6$ $10^6 - 10^7$	30-70 500
Class I ^d	1000 AU	Envelope: 0.015 Protostar: < 0.5	10^{12} at 1 AU (midplane)	> 2000 (protostar)
Class II	30-300 AU	Disk: 0.005 – 0.01 ^d Star: 0.5 – 2	Midplane ^a : 10^{14} Disk surface ^a : 10^6	Midplane ^a : 100 Disk surface ^a : 300
Class III ^d	30-300 AU	Disk: $10^{-5} - 10^{-4}$ Star: 0.5 – 2	–	–

1. Introduction

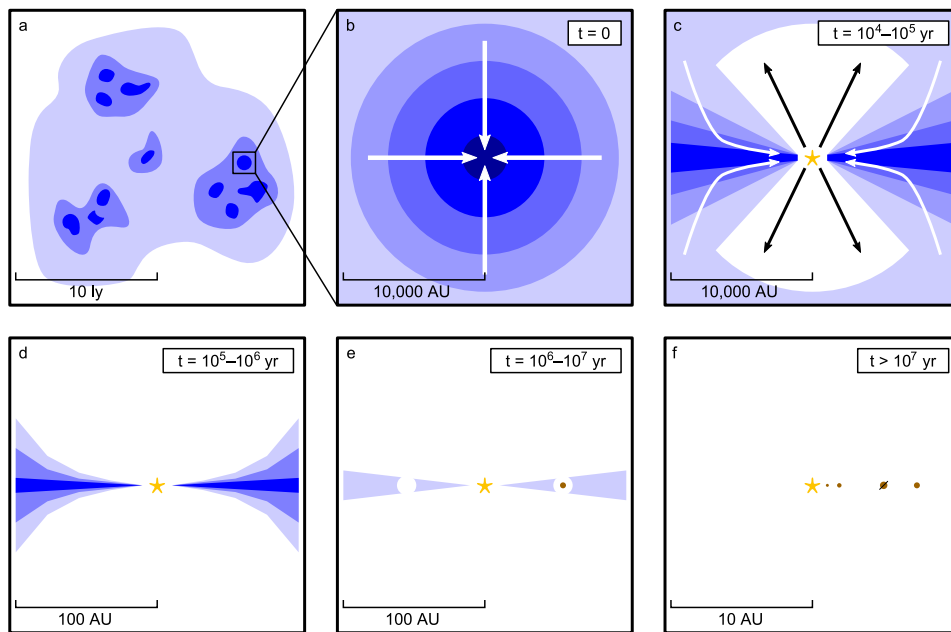


Figure 1.8: The formation of the Solar System. The parent molecular cloud is fragmented (a), and one of such fragments becomes a dark core (b), which forms a *protostar* at the center of the collapse (Class 0 object). Within the core, a disk forms around the protostar (Class I object), conserving the initial angular momentum of the collapsing cloud. At this stage, the protostar is obscured by the optically thick envelope (c). A thin accretion disk (Class II object) is left after the envelope is carved by outflows (d). After accretion and photoevaporation a debris disk is formed (e), and planets are already observable (Class II object). Finally, planets clear the disk of the remaining dust and a planetary system has been born (f). Figure taken from Ioppolo (2010), modified from the original in Visser (2009), based on Hogerheijde (1998).

which in the $z/r \ll 1$ limit reduces to:

$$F_G = \frac{GMdmz}{r^3} = \Omega^2 dm z . \quad (1.8)$$

Here $\Omega = \sqrt{GM/r^3}$ is the Keplerian angular velocity. On the other hand, if the mass element dm is at a density ρ , it feels a pressure dP over an area dA :

$$F_P = dP dA = \frac{1}{\rho} \frac{dP}{dz} \rho dz dA = \frac{1}{\rho} \frac{dP}{dz} dm . \quad (1.9)$$

Here dP/dz is the pressure gradient that expands the gas vertically. Assuming a vertically isothermal gas, pressure is proportional to density and the sound speed of the gas c_s squared:

$$P = c_s^2 \rho . \quad (1.10)$$

Thus, the pressure-gradient force can be written as:

$$F_P = \frac{c_s^2}{\rho} \frac{d\rho}{dz} dm . \quad (1.11)$$

In hydrostatic equilibrium, both forces are balanced:

$$\frac{c_s^2}{\rho} \frac{d\rho}{dz} = \Omega^2 z . \quad (1.12)$$

Solving for ρ we find:

$$\rho = \rho_0 e^{-z^2/2h^2} . \quad (1.13)$$

Here h is the vertical density scale height, or simply *scale height*:

$$h = \frac{c_s}{\Omega} . \quad (1.14)$$

This relation implies that in general the sound speed (and by extension, the temperature) can have a non-trivial radial distribution. The density at $z = 0$, ρ_0 is found by integrating the density over the entire z range, thus obtaining the surface density Σ for a given r :

$$\Sigma(r) = \int_{-\infty}^{\infty} \rho dz = \frac{\sqrt{2\pi}}{h} \rho_0 . \quad (1.15)$$

Thus:

$$\rho_0 = \frac{\Sigma}{\sqrt{2\pi}} . \quad (1.16)$$

The surface density can be scaled to the encircled disk mass at a radius r :

$$M_{\text{disk}}(r) = \pi r^2 \Sigma . \quad (1.17)$$

Thus:

$$\rho_0 = \frac{1}{\sqrt{2\pi^3}} \frac{M_{\text{disk}}(r)}{r^2} . \quad (1.18)$$

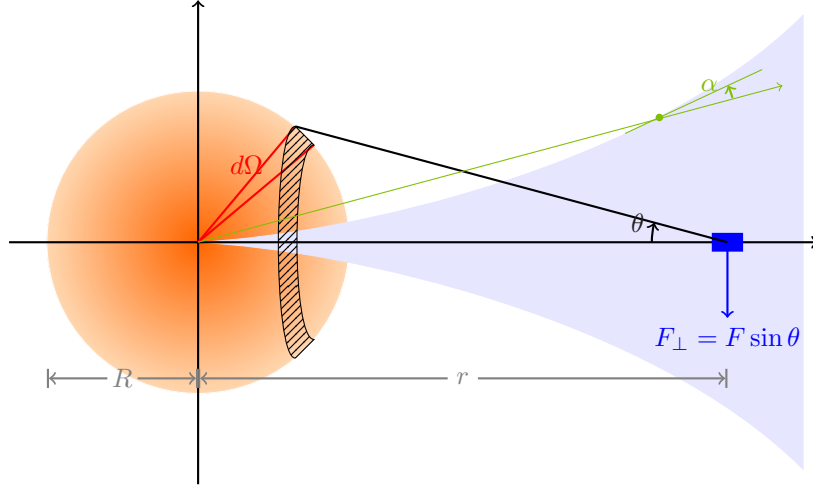


Figure 1.9: Diagram for calculating the temperature structure of a flat and a flaring disk.

1.3.2 Gravitational stability of the disk

An important concern that we can raise at this point is whether the gravitation of the disk itself is indeed negligible. The gravitational field of the disk is that of a thin sheet, which by Gauss' law is $2\pi G \Sigma$. This field must be lower than the gravitational field of the star at the scale height h :

$$2\pi G \Sigma < \frac{GMh}{r^2}. \quad (1.19)$$

Using Eq. (1.17) we obtain the following disk-to-star mass ratio condition:

$$\frac{M_{\text{disk}}}{M} < \frac{h}{2r}. \quad (1.20)$$

To an order of magnitude, our thin disk assumption tells us (and observations agree) that $h/r \lesssim 0.1$. This means that by having a disk mass lower than $\sim 10\%$ of the stellar mass we can avoid the issues of a self-gravitating disk. The previous analysis is roughly equivalent to the stability condition given by the Toomre parameter, $Q = \frac{c_s \Omega}{\pi G \Sigma} < 1$.

1.3.3 Radial temperature structure

In order to obtain the radial temperature profile of the disk, let us start with the simplest assumption about the heating mechanism: a star with radius R uniformly illuminates an infinitely thin, flat disk, while neglecting the effects of accretion heating.

If the disk is in hydrostatic equilibrium, the effects of radiation heating can change the vertical structure of the disk.

A ring-like element of the surface of the star has a solid angle $d\Omega$. This solid angle is given by the angular size $d\theta$ as perceived from an area element on the disk surface located at a radius r , corresponding to the blue rectangle in Fig. 1.9:

$$d\Omega = 2 \sin \theta d\theta , \quad (1.21)$$

after integration over half of the azimuthal angle range (one-side illumination). The area element on the disk is illuminated by the vertical component of the stellar photon flux dF emitted by the ring-like element on the star:

$$dF_{\text{disk}} = dF_{\perp} = dF \sin \theta . \quad (1.22)$$

The flux element dF is given by the stellar luminosity L and the solid angle $d\Omega$:

$$dF = L d\Omega = 2L \sin \theta d\theta . \quad (1.23)$$

We integrate the flux received by the disk over all possible viewing angles, from 0 to $\theta_m = \sin^{-1}(R/r)$:

$$F_{\text{disk}} = 2L \int_0^{\theta_m} \sin^2 \theta d\theta = L (\theta_m - \sin \theta_m \cos \theta_m) . \quad (1.24)$$

In the $r \gg R$ limit, this reduces to:

$$F_{\text{disk}} = \frac{2}{3} L \left(\frac{R}{r} \right)^3 . \quad (1.25)$$

Considering that the received radiation is the main source of heating for the disk, we can deduce the radial temperature profile of the disk with the help of the Stefan-Boltzmann law:

$$T_{\text{disk}} \propto F_{\text{disk}}^{1/4} \propto r^{-3/4} . \quad (1.26)$$

Although this is interesting on its own, the surprise comes when we remember that the scale height is proportional to the sound speed, and therefore to $T_{\text{disk}}^{1/2}$:

$$h \propto \frac{T_{\text{disk}}^{1/2}}{r^{3/2}} , \quad (1.27)$$

which in combination with Eq. (1.26) yields,

$$h/r \propto r^{1/8} . \quad (1.28)$$

1. Introduction

Here the relative vertical scale of the disk is increasing with radial distance! This means that the disk is not flat at all, but it presents a flared shape to incoming radiation.

A flared disk will present a larger front to incoming radiation, which means that its surface will be heated more efficiently. For this reason we need to take the flaring effect into consideration if we want to obtain a consistent temperature profile. In order to do this, we define the grazing angle α as the angle that a flaring area element of the disk makes with the direction of the incoming radiation from the star (Figure 1.9). In the $r \gg R$ limit, this grazing angle is of the order of h/r . If the grazing angle is low (which it usually is), the received flux is approximated by a simple inverse square radius relation:

$$F_{\text{disk}} \propto \frac{\alpha}{r^2} . \quad (1.29)$$

Following Eq. (1.26), the adjusted temperature follows the Stefan-Boltzmann law:

$$T_{\text{disk}} \propto \left(\frac{\alpha}{r^2} \right)^{1/4} = T_{\text{disk}}^{1/8} r^{-3/8} . \quad (1.30)$$

Solving for T_{disk} we obtain a new temperature profile consistent with flaring, although flatter than the original profile obtained in Eq. (1.26) (Chiang & Goldreich 1997):

$$T_{\text{disk}} \propto r^{-3/7} . \quad (1.31)$$

1.3.4 Dust temperature

If sub-mm and μm dust is present in the disk surface, the optically thin layer of a flaring disk is also very thin compared to the disk scale height. This layer is then able to re-emit stellar radiation into the disk interior, which will be heated by absorption of this radiation. Therefore the interior dust layer will be cooler than the surface dust layer. In order to estimate the temperature profiles we have to consider the heating balance of both layers.

The surface dust layer. This optically thin layer is directly irradiated by the star, which means that we can obtain a temperature profile for T_{dust} from the balance between stellar heating and radiative cooling of dust:

$$\frac{Q_{\text{heat}}}{Q_{\text{cool}}} = \frac{\pi a^2 \epsilon F}{4\pi a^2 \epsilon_{\text{dust}} F_{\text{dust}}} = 1 . \quad (1.32)$$

Here the stellar flux at r is $F \propto T^4 (R/r)^2$, the dust radiative cooling flux is $F_{\text{dust}} \propto T_{\text{dust}}^4$, ϵ is the emissivity for dust absorption of the stellar radiation, and ϵ_{dust} is the

emissivity of dust emission. The heating/cooling balance equation reduces to:

$$\frac{T_{\text{dust}}}{T} = \left(\frac{\epsilon}{\epsilon_{\text{dust}}} \right)^{1/4} \left(\frac{R}{2r} \right)^{1/2}. \quad (1.33)$$

At wavelengths higher than the average dust size a , $\epsilon \propto \lambda^{-1}$, which near the peak of thermal radiation means that $\epsilon \propto T$ by Wien's displacement law. Solving for T_{dust} we obtain a power law for the temperature structure of the surface dust layer:

$$T_{\text{dust}} \propto r^{-2/5}. \quad (1.34)$$

The interior dust layer. This layer is heated by radiation from the star, as the surface layer is optically thin. Here the temperature of the gas and dust is coupled because of collisions between the gas and dust. Therefore, the dust temperature follows the same profile as in Eq. (1.31).

1.3.5 Rotational speed of the gas

Due to the presence of the gradient-pressure force acting radially, we cannot realistically expect the disk material to be rotating at Keplerian speeds. This is evident when writing down the radial force balance on a rotating disk element:

$$F_G + F_{P,\text{radial}} = m \frac{v_{\text{rot}}^2}{r}. \quad (1.35)$$

As the disk is accreting, the pressure gradient is usually negative, and the rotational speed of the gas will be sub-Keplerian:

$$\frac{v_{\text{rot}}}{r} \lesssim \sqrt{\frac{GM}{r}} = v_K. \quad (1.36)$$

Since there is an offset between the rotation of the disk material and the Keplerian velocity, small dust grains that efficiently couple to the gas will follow the gas, while larger planetesimal can de-couple and will feel a drag effect, or headwind which causes them to fall toward the star (Weidenschilling 1980). The typical radial drift speeds for meter-sized objects can be of the order of 100 m/s (Blum 2010). At such high speeds, collisions between meter-sized bodies will fragment them, thus impeding the formation of larger objects. This issue is referred to as the *meter-size barrier*, and is an unsolved puzzle in the field of planet formation.

1.3.6 Mechanism for accretion

Accretion is the commonly accepted process by which disks channel matter onto the star and thus build up the stellar mass. After a star is formed and most of the envelope is gone (Class II source) the disk material must find a way to lose angular momentum to accrete onto the central star.

It is clear that a torque-creating friction mechanism must play a role in transferring angular momentum from the inner to the outer disk. What is not clear, though, is the exact nature of this mechanism. Small-scale friction, such as molecular viscosity, yields a timescale for accretion that is too long, and thus incompatible with the observed disk lifetime. Large scale turbulence, where large clumps of matter in the disk interact with each other, may present a better solution to the accretion problem.

As the largest possible clump of matter in the disk cannot be wider than the disk scale height, and the turbulent speed cannot be higher than the sound speed, a simple yet effective prescription for this large-scale viscosity is given by the following expression:

$$v = \alpha h c_s . \quad (1.37)$$

This is called the Shakura-Sunyaev alpha-prescription for turbulent viscosity (Shakura & Sunyaev 1973), and it was originally conceived to model X-ray binary disks. Here, α is a free parameter that can be used to scale the viscosity to match the observed disk lifetimes derived from accretion rates.

Using a parametrization, we avoid the question about the nature of the interaction that gives rise to the turbulent viscosity. There are a couple of promising ideas, but none of them are entirely understood. Currently, there is no way to directly observe the mechanism behind the turbulence as it occurs on very small scales. However, Guilloteau & Dutrey (1998) attempted to measure this effect from line profiles in the sub-mm, showing that turbulent velocities are below 1 km/s by disentangling the rotational broadening and turbulent broadening of the $^{12}\text{CO}, J=1 \rightarrow 0$ line.

The main candidate for this viscosity is Magneto-Rotational Instabilities (MRI) (Balbus & Hawley 1991). In this picture, material that has been ionized by stellar radiation interacts with the magnetic field of the star. Two parcels of material located at different radii from the star will tangle and stretch the magnetic field lines causing friction, which can be understood as a simple spring connecting both parcels. This way, the parcel closest to the star will lose angular momentum to the adjacent parcel, and will fall toward the star. The outer parcel gains angular momentum and moves to

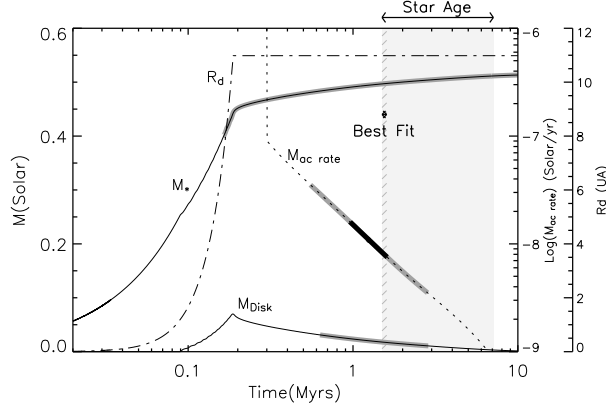


Figure 1.10: Evolution of star mass and disk mass as a function of time with masses in solar units (corresponding axis to the left). The accretion rate onto the central star is shown as a dotted line (corresponding axis: first to the right). The evolution of the centrifugal radius is shown as a dash-dotted line (corresponding axis: far-right). Figure and caption taken from (Hueso & Guillot 2005).

a higher orbit, where it may lose angular momentum to another parcel. The disk will spread because of this angular momentum transport.

1.3.7 Evolution of an accretion disk

Turbulent viscosity in the disk will create a torque which redistributes angular momentum from the inner to the outer disk. This effect will cause a change in the shape of the surface density distribution of the disk. Solving the fluid continuity equation along with the radial component of the angular momentum conservation equation we can obtain a formula for the evolution of the surface density distribution (Pringle 1981):

$$\frac{\partial \Sigma}{\partial t} = \frac{3}{R} \frac{\partial}{\partial R} \left[R^{1/2} \frac{\partial}{\partial R} (v \Sigma R^{1/2}) \right]. \quad (1.38)$$

A simple inspection of this formula reveals that this is actually a diffusion equation. This is evidenced when an narrow ring of material at a distance r_0 is set as initial condition for Eq. (1.38). An initial narrow concentration of matter will diffuse downwards and toward $r = 0$ (Crida et al. 2007). The evolution of an actively accreting disk will then allow for an early distribution of matter (e.g. $\Sigma \propto r^{-1}$) to flatten at a later stage (e.g. $\Sigma \propto r^{-1/2}$), corresponding to the effect of angular momentum transport.

1. Introduction

In the disk midplane, especially the inner few AU, viscous heating can dominate the energy balance of gas and dust if accretion rates are high. As soon as accretion rates are low, diffusion of stellar radiation sets the midplane temperatures. Figure 1.10 shows a model of the evolution of an accreting disk and star.

1.4 Chemistry in disks

Early observations of complex molecules in the interstellar medium such as CH, CN, CH⁺ (Herbig 1968), NH₃ (Cheung et al. 1969), H₂O (Cheung et al. 1968), H₂CO (Snyder et al. 1969), and CO (Wilson et al. 1970) puzzled astronomers, as their formation in such cold, empty environment could not be fully explained at the time. This motivated the development of astrochemically relevant models that could explain the growing number (and complexity) of observed chemical species (Solomon & Klemperer 1972). In recent years, more complex chemical networks (Woodall et al. 2007) have been used to study the chemical composition of protoplanetary disks. Early 1D models considered both gas-phase reactions and surface reactions such as ad/desorption onto the surface of dust grains time-dependent chemistry (Aikawa et al. 1997a) and steady state chemistry (Willacy et al. 1998), while focusing on layering of chemical species in the disk. This was taken further in full 2D steady-state models of the chemistry (Semenov et al. 2010; Walsh et al. 2010) and 1D time-dependent models including surface chemical reactions Semenov et al. (2010). More recent 2D models have become even more sophisticated: Visser et al. (2009) kept track of the chemical evolution in individual parcels of collapsing cloud material during the disk formation phase, Semenov & Wiebe (2011) considered the effects of turbulent transport processes on the chemical evolution, while Woitke et al. (2009) solved the steady-state chemistry iteratively, in a way that is consistent with the hydrostatic structure of the disk, the full 2D radiative transfer, and the heating and cooling balance. The impact of X-ray processes on the disk chemistry has been studied recently by Aresu et al. (2011); Walsh et al. (2012) and Meijerink et al. (2012).

The chemical structure of protoplanetary disks can be roughly divided in three layers (Aikawa et al. 2002; Bergin et al. 2007). In the disk surface, stellar UV radiation creates a hot ($T > 1000$ K) layer of ionized and atomic species (C⁺, C, N, H, O). Beneath this layer, molecules (H₂, CO, HCN, OH, H₂O, CO₂, N₂) are formed in the gas phase and survive thanks to the warm ($T > 100$ K) temperatures. In the inner disk, a rich neutral-neutral chemistry dominates the picture, while in the outer disk ion-molecule reactions can occur due to some stellar UV photons still being able to penetrate. In the cold ($T < 80$ K) midplane, many gas-phase species condensate onto

dust grains (CO, CH₄, CO₂), although this depends strongly on the local temperature. It is in this region where simple organic molecules detected in comets such as CH₄ and H₂CO (Bockelée-Morvan 2010) are formed. Vertical mixing could make detection of organic molecules originally formed in the midplane possible for currently developing instrumentation such as H₂CO (Henning & Semenov 2008).

As I mentioned above in Section 1.3, the physical, thermal and radiative structure of the disk defines the laboratory in which we will explore the chemistry. The recipe is pretty straightforward. Find a big database of astrophysically relevant chemical reactions such as UMIST (Woodall et al. 2007) or KIDA (Wakelam et al. 2012), choose your desired number of species N_{species} , and solve the resulting chemical rate equations. The number of species chosen here depends on the desired complexity for the model. In the case of the UMIST06 database, 420 chemical species and 4572 chemical reactions are available, from which a smaller number of species can be selected, limited by the maximum number of elements and atoms-per-molecule that the model requires for comparing with observations. In this system of coupled differential equations, the expression for the rate of change of the density n_i of species i has the following general form:

$$\frac{dn_i}{dt} = R_i^+ - R_i^- . \quad (1.39)$$

Here the right hand side terms refer to all rates that produce or destroy a given species i . Given that our goal is to understand the chemical processing of the primordial disk material, both gaseous and solid, we need to understand the relation between the gas and the dust grains. For this reason we need to take into account grain surface processes such as ad/desorption of species in addition to gas-phase reactions, taking ice species as separate from their gas-phase counterparts in the chemical rate equation. Adsorption occurs when a gas species condenses onto the ice mantle on the surface of a dust grain. Desorption is the opposite process, where an ice phase species evaporates from the surface of dust grains.

For a two-body reaction $l = 1, N_{\text{reactions}}$ between species i and species j (Table 1.3), the reaction rate is calculated with the use of the rate constant k and the densities $n_{i,j}$:

$$R_{lij} = k_{lij} n_i n_j . \quad (1.40)$$

The rate constant is calculated from experimental measurements or theoretical estimates of the collision frequency, the steric factor and the activation energy of the reaction according to the Arrhenius law. In the UMIST (Woodall et al. 2007) format

1. Introduction

Table 1.3: List of common two-body reaction types in astrochemical networks (Shaw 2006)

Reaction type	General form
Neutral-neutral	$A+B \rightarrow AB$
Radiative association	$A+B \rightarrow AB + \text{photon}$
Neutral exchange	$AB+D \rightarrow A+BD$
Ion-molecule	$AB+D^+ \rightarrow A+BD^+$
Charge transfer	$AB+D^+ \rightarrow AB^++D$
Radiative recombination	$A^++e^- \rightarrow A + \text{photon}$
Radiative association	$A+e^- \rightarrow A^-$
Dissociative recombination	$AB+e^- \rightarrow A+B^-$, or $AB^++e^- \rightarrow A+B$
Negative ion	$A+A^- \rightarrow A_2+e^-$, or $A+B^- \rightarrow AB+e^-$

the rate constant is calculated according to the following parametrization:

$$k = \alpha \left(\frac{T}{300} \right)^\beta e^{-\gamma/T}. \quad (1.41)$$

Photodissociation/ionization and ad/desorption of species are reactions involving only one species i (Table 1.4), for which their rate is calculated as:

$$R_{li} = k_{li} n_i \quad (1.42)$$

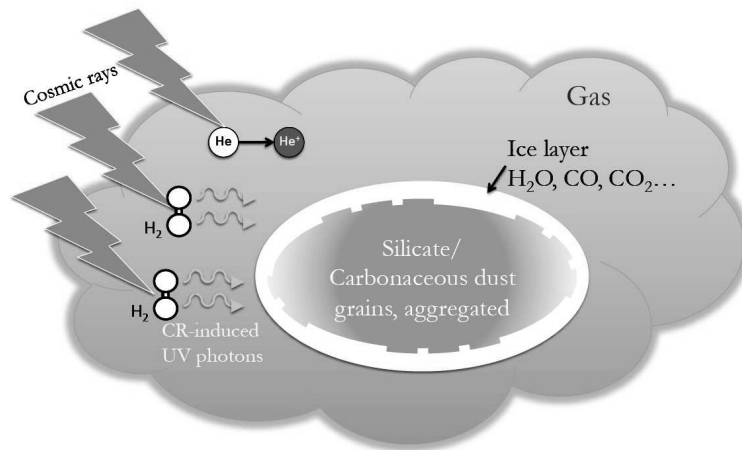
Photoprocess rates scale with the intensity and shape of the local radiation field, and the cross-section for absorption of a UV photon. Ad/desorption rates depend on the local thermal/radiation conditions, binding energy and/or dust size distribution. Three main desorption processes are considered here: *thermal desorption* is the evaporation of an ice species from the grain surface due to temperature effects, *photodesorption* occurs when an ice species leaves the ice mantle after a UV photon strikes the grain surface, and *cosmic-ray desorption* occurs after a temporary heating event caused by a cosmic ray impact on the dust grain.

1.4.1 Time-dependent chemistry

It is straightforward to derive the equilibrium solution for the chemical rate equation, as all that is required is to set the left hand side to zero and solve the jacobian of the ODE to find the steady-state abundances. Unfortunately this solution gives a bad approximation in the disk midplane (Woitke et al. 2009). Here the temperature and

Table 1.4: List of photoprocesses and ad/desorption reaction types in astrochemical networks (Woitke et al. 2009)

Reaction type	General form
Photoionization	$A + \text{photon} \rightarrow A^+ + e^-$
Photodissociation	$AB + \text{photon} \rightarrow A + B$
Adsorption	$A \rightarrow A_{\text{ice}}$
Thermal desorption	$A_{\text{ice}} \rightarrow A$
Photodesorption	$A_{\text{ice}} + \text{photon} \rightarrow A$
Cosmic-ray desorption	$\text{CR} + \text{dust} \rightarrow A_{\text{ice}} \rightarrow A$

**Figure 1.11:** Gas-grain environment and cosmic-ray induced photons.

1. Introduction

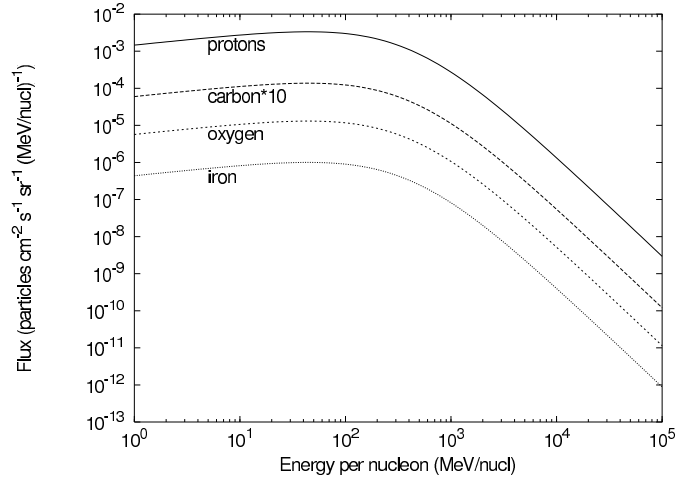


Figure 1.12: Cosmic ray energy spectra for different nucleons. Figure taken from Shen et al. (2004).

density conditions are such that the timescale for reaching a solution can be longer than the lifetime of the disk. This is particularly important for the formation of ices, which have very long ad/desorption timescales.

Given that stellar ionizing radiation cannot penetrate these regions, cosmic rays are the main mechanism by which the disk midplane is ionized. Studying how cosmic rays affect the chemical evolution in the midplane (Figure 1.11) by solving the chemical rate equations in a time-dependent way can give us a better insight on how ices, and in particular simple organic species are formed in protoplanetary disks.

1.5 Cosmic rays

Cosmic rays are highly energetic particles which are isotropically generated in supernovae shock events throughout the galaxy. They were first detected at the beginning of the 20th century in experiments with radioactive elements, when ionization events occurred while no radioactive sample was in the experimental chamber (Wulf 1909). For the most part they are protons and atomic nuclei, and their average kinetic energy is of the order of 1 GeV per nucleon, although their energy spectrum is very broad (Fig. 1.12).

Elsewhere in our galaxy, their activity can be observed by looking at H_3^+ in the

line of sight of molecular clouds, which is a tracer of ionization of molecular hydrogen (Indriolo et al. 2007). In protoplanetary disk environments, they are expected to play a significant role in ionizing the disk material and in heating the gas (Glassgold et al. 2007). The vertical column density of a typical T Tauri disk at 1 AU is close to the estimated attenuation limit of cosmic ray ionization, which is about 150 g cm^{-2} (Umebayashi & Nakano 1981). Therefore we estimate that the correction factor for the cosmic ray ionization rate ζ_{H_2} would be approximately $1/e$ (Semenov et al. 2010). However, this is covered by the uncertainty in the cosmic ray-ionization rate itself, for which there is no consensus (Indriolo et al. 2007). According to Padovani & Galli (2011), magnetic mirroring in molecular cloud cores significantly hampers the penetration of cosmic rays, which could mean that magnetic fields in protoplanetary disks may further attenuate ζ_{H_2} . However, it is not yet clear whether this effect is relevant to the particular geometry of the magnetic fields in protoplanetary disks, which remains largely unknown.

1.5.1 Cosmic ray-induced UV photons

Besides direct ionization of gas phase species, cosmic rays can ionize the medium in a less direct way: by inducing a UV field that comes from secondary ionization of molecular hydrogen. This process, known as the Prasad-Tarafdar mechanism (Prasad & Tarafdar 1983), starts when an electron, with a typical energy of 30 eV, is released after the cosmic ray ionization of an H_2 molecule. This electron then hits another (neutral) H_2 molecule, which leaves it in an excited electronic state (Sternberg et al. 1987; Riahi et al. 2006). After this, H_2 spontaneously decays to the excited vibrational states of the $B \ ^1\Sigma_u^+$ and the $C \ ^1\Sigma_u$ levels. In the subsequent decay to excited vibrational states of the ground electronic level $X \ ^1\Sigma_g^+$ of H_2 , Lyman and Werner photons are emitted in the 1.76 – 3.28 PHz frequency range (90-170 nm). The corresponding emission probability profile is shown in Fig. 1.13. Vibrationally excited H_2 can also be dissociated in subsequent encounters with other chemical species, because the activation barrier can be lowered by the availability of the internal energy of the H_2 molecule (see Agúndez et al. 2010).

This field is generated locally wherever cosmic rays penetrate. Because of this, it is locally extinguished by the gas and dust. This is evident when we consider the mean free path length of a UV photon in this region. Assuming a dust UV extinction cross section of the order of $10^{-22} \text{ cm}^2/\text{H-atom}$ (Gredel et al. 1989) and a typical 1 AU density of 10^{14} cm^{-3} , the mean free path would be of the order of 1000 km, which means that these photons are absorbed locally. The total gas and dust UV extinction

1. Introduction

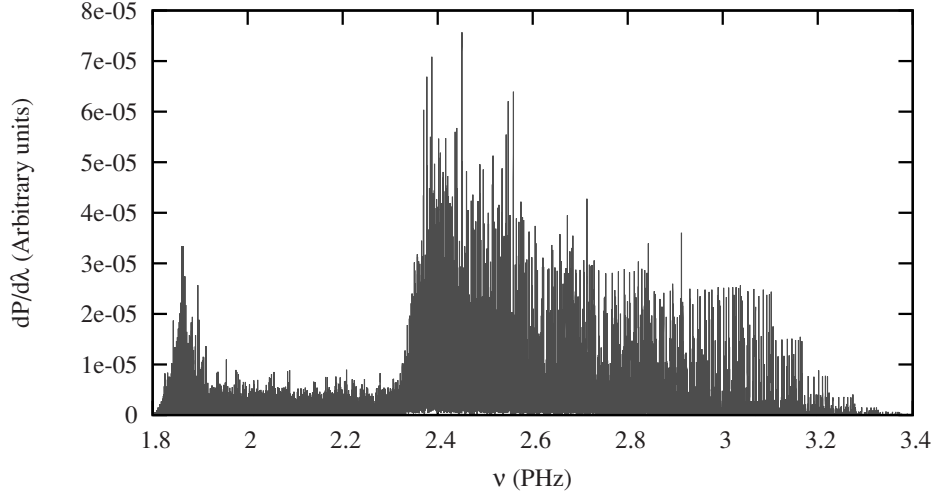


Figure 1.13: Emission probability profile for Cosmic Ray-Induced UV (CRUV) photons. This emission profile comes from the de-excitation of an H_2 molecule that has been excited by electrons produced in cosmic ray ionization of another H_2 molecule (Abgrall et al. 2000).

cross-section is calculated according to the following formula:

$$\sigma_{\text{tot}}(\nu) = (1 - \omega)\sigma_{\text{dust}}(\nu) + \sum_j \left(\frac{n_j}{n_{\langle\text{H}\rangle}} \right) \sigma_j(\nu). \quad (1.43)$$

The first term on the right hand side corresponds to the extinction by dust, where ω is the dust grain UV albedo and $\sigma_{\text{dust}}(\nu)$ is the dust extinction cross-section. The second term is the total gas extinction, adding the partial extinctions of gas-phase species. Each species contributes a fraction of the gas extinction depending on their abundance $n_i/n_{\langle\text{H}\rangle}$ and the photoprocess cross-section $\sigma_j(\nu)$ (van Dishoeck et al. 2006). Note that only species that are susceptible to photodissociation/ionization in the wavelength relevant for absorption of *Cosmic Ray-Induced UV (CRUV)* photons in the 90-170 nm range, contribute to the gas extinction⁴.

Rate constants for CRUV photoprocess in the interstellar medium are listed in the UMIST database (Woodall et al. 2007), where they use data from Sternberg et al.

⁴To be completely accurate, we would have to consider the full gas extinction cross section, which would not only contain photodissociation/ionization, but also excitation. Excitation of a chemical species leads to de-excitation, in which a UV photon can be re-emitted, but it could also de-excite in a ladder of transitions occurring mostly in the IR (e.g. CO). We are aware that this is a limitation of this approach.

(1987) and Gredel et al. (1989). However, they assume that the gas extinction is negligible, and only consider extinction of this field by dust grains to be relevant, i.e. $\sigma_{\text{tot}} \approx (1 - \omega)\sigma_{\text{dust}}$. Gredel et al. (1989) ignored the contribution of the gas opacity, assuming that high gas abundances (other than CO) would never appear under interstellar medium conditions. This assumption does not hold for protoplanetary disks, as many species that cause CRUV extinction (for example CH₄, CO₂, O₂) have high gas-phase abundances in the inner midplane, inside the snow line, whereas in the interstellar medium they are almost non-existent in the gas phase. As mentioned above in Sections 1.1.1 and 1.1.2, dust grains in protoplanetary disks are processed further than in molecular clouds, which leads to grain growth. This causes the dust UV extinction cross-section to be larger in protoplanetary disks, which can lead to an enhancement in the CRUV flux in gas-poor regions of the disk midplane. In its full form, the rate constant for CRUV photodissociation/ionization processes in protoplanetary disks should be calculated as:

$$k_i = \zeta_{\text{H}_2} \int_{1.76 \text{ PHz}}^{3.28 \text{ PHz}} \frac{P(\nu)\sigma_i(\nu)}{(1 - \omega)\sigma_{\text{dust}}(\nu) + \sum_j \left(\frac{n_j}{n_{\text{H}}}\right)\sigma_j(\nu)} d\nu. \quad (1.44)$$

Some of the species that contribute to the gas extinction of CRUV photons are themselves generated via chemical pathways that include CRUV photoprocessing of other species. This poses a computational challenge for finding a solution to the chemical rate equation.

1.6 This thesis

In this thesis we set out to constrain the chemical conditions in the early Solar System by analyzing chemical evolution models of protoplanetary disks and comparing them to our current knowledge of the chemical composition of Solar System bodies, such as comets. To achieve this, we require consistent radiative and hydrostatic disk models to set the local temperature, density and radiation field in which the gas/grain chemistry evolves. Given that the planet (and comet) forming region of disks largely coincides with the cosmic-ray dominated midplane of disks, we also focus in understanding the role of cosmic ray-induced processes in the chemical evolution.

In Chapter 2 (Chaparro Molano & Kamp 2012b), I present a time dependent analysis of the gas/grain chemistry in cold, gas-poor regions of protoplanetary disks. I focus on the role of OH on the gas-phase formation pathways for ices, and how OH is generated in cosmic ray-induced UV photoprocessing of other species. In addition, I present a method for calculating CRUV photoprocess rates in a way that is consistent

1. Introduction

with protoplanetary disk dust extinction. I find that the density and temperature conditions in the region of the disk midplane at radial distances larger than 10 AU in our model are ideal for the formation of ices that match observed cometary abundances.

I explore the chemical evolution of gas-rich regions of protoplanetary disks in Chapter 3 (Chaparro Molano & Kamp 2012b). In order to assess the role of CRUV photoprocesses, the effects of local gas extinction need to be taken into account. I improve on the CRUV photorate calculation from Chapter 2 by performing a frequency-dependent integration of the emission probability profile (Fig. 1.13) over both the local gas and dust extinction cross sections (see Eq. 1.44). I find that gas opacity in gas-rich regions of the disk midplane ($r < 10$ AU) is almost 30% of the total opacity. CO, CO₂, SiO and OH are found to be the main contributors to CRUV extinction, besides dust grains. I propose that gas-phase species created in the midplane may drift vertically to optically thin zones. In the case of SiO, its photodissociation timescale is long enough that it guarantees its survival in such regions. Thus, SiO and species that behave similarly can be used to probe the midplane chemical activity in future high angular resolution observations of disks.

In Chapter 4 I extend the method for self-consistently calculating CRUV rates developed in the previous two chapters to a fully converged 2D disk model in vertical hydrostatic equilibrium. I study the effects of CRUV in the chemical evolution of the gas and ice species, and I find that the ice species found in cometary bodies are formed in timescales shorter than the lifetime of the disk, thus showing that steady-state models of the chemistry underpredict the abundances of such species. I also discuss the possibility of trapping ice species formed in early stages of the disk evolution in the layers closest to the dust grain surface, thus forming a stratified ice mantle.

In Chapter 5 I focus on the layered formation of ices on the surface of spherical dust grains. I find that in most regions of the disk midplane, there is a primary mantle of ices that is ~ 300 monolayers thick. At 30 AU, a secondary ice mantle forms that makes the primary ice mantle double in size. The chemical composition of each mantle is set by the local thermal conditions in which they are formed. I obtain an ice-to-dust mass ratio in these cometary precursors that agrees within an order of magnitude with the assumed cometary ratio. I find that ice mantle growth contributes to increase the size of dust grains: the radius of a typical dust grain of size $0.2 \mu\text{m}$ will increase to $0.4 \mu\text{m}$. Such a modification in the dust size distribution will impact the dust opacities (which set the midplane thermal profile) and the sticking efficiency (which enhances the process of dust coagulation).

2 The role of OH in the chemical evolution of protoplanetary disks

I. The comet-forming region

—G. Chaparro Molano & I. Kamp—

Astronomy & Astrophysics 537, A138 (2012)

*In the depth of winter, I finally learned that
within me there lay an invincible summer.*
— Albert Camus, *Retour à Tipasa* —

2. Chemistry in the comet-forming region

Abstract

Context. Time-dependent gas-grain chemistry can help us understand the layered structure of species deposited onto the surface of grains during the lifetime of a protoplanetary disk. The history of trapping large quantities of carbon- and oxygen-bearing molecules onto the grains is especially significant for the formation of more complex (organic) molecules on the surface of grains.

Aims. Among other processes, cosmic ray-induced UV photoprocesses can lead to the efficient formation of OH. Using a more accurate treatment of cosmic ray-gas interactions for disks, we obtain an increased cosmic ray-induced UV photon flux of 3.8×10^5 photons $\text{cm}^{-2}\text{s}^{-1}$ for a cosmic-ray ionization rate of H_2 value of $5 \times 10^{-17} \text{ s}^{-1}$ (compared to previous estimates of 10^4 photons $\text{cm}^{-2}\text{s}^{-1}$ based on ISM dust properties). We explore the role of the enhanced OH abundance on the gas-grain chemistry in the midplane of the disk at 10 AU, which is a plausible location of comet formation. We focus on studying the formation/destruction pathways and timescales of the dominant chemical species.

Methods. We solved the chemical rate equations based on a gas-grain chemical network and correcting for the enhanced cosmic ray-induced UV field. This field was estimated from an appropriate treatment of dust properties in a protoplanetary disk, as opposed to previous estimates that assume an ISM-like grain size distribution. We also explored the chemical effects of photodesorption of water ice into OH+H.

Results. Near the end of the disk's lifetime our chemical model yields H_2O , CO, CO_2 and CH_4 ice abundances at 10 AU (consistent with a midplane density of 10^{10} cm^{-3} and a temperature of 20 K) that are compatible with measurements of the chemical composition of cometary bodies for a [C/O] ratio of 0.16. This comparison puts constraints on the physical conditions in which comets were formed.

2.1 Introduction

Understanding the evolution of gas-grain chemistry and the role of the dust size distribution in protoplanetary disks is paramount to understanding their history. This history is imprinted in the remnants of the formation of the disks, namely asteroids and cometary bodies in our solar system. However, in-depth theoretical and laboratory studies of gas-grain chemical networks have only been researched in recent times (Aikawa et al. 1997a; Willacy et al. 1998; Roberts et al. 2007; Öberg et al. 2009; Visser et al. 2009; Woitke et al. 2009). Chemical networks in protoplanetary disk-like conditions have not been as thoroughly studied as in molecular cloud-like conditions (Hasegawa & Herbst 1993; Bates 1986; Woodall et al. 2007). For these reasons, we are interested in exploring chemical pathways in different regions of the disk, focusing on the role of OH, a highly reactive radical that can change the molecular composition of the gas when efficiently formed. To accomplish that, we study the chemical evolution and the chemical network in two regions of the disk midplane, including enhanced OH formation from cosmic rays and photodesorption of water ice.

Our goal is to study the time-dependent chemistry in the cold comet-formation zone, which in a T Tauri-type protoplanetary disk can be located at 10 AU (Kelley & Wooden 2009). We include in our chemical network the most important adsorption-desorption processes for H₂O, CO, CO₂ and CH₄ (Hasegawa & Herbst 1993; Collings et al. 2004; Öberg et al. 2009), which link the gas species to the icy surface of grains. We also use a refined approach to calculating the effect of cosmic rays on both gas and grains (Leger et al. 1985; Cecchi-Pestellini & Aiello 1992; Shen et al. 2004). Cosmic rays are important because they drive the chemistry in some regions of the disk via the ultraviolet (UV) field produced by their ionization of H₂ (Prasad & Tarafdar 1983; Sternberg et al. 1987; Gredel et al. 1989). This secondary UV field can photodissociate many chemical species and change the chemical balance, especially in regions of the disk that are opaque to stellar and interstellar radiation: the highly energetic cosmic rays can reach deep into the midplane of the disk. For this reason, the midplane of the disk can be considered as a cosmic-ray dominated region.

To analyze the chemical evolution, the local environment of the chemical system should resemble the conditions in a protoplanetary disk as much as possible. One of the main tools for building chemical networks in astronomy, the UMIST database for astrochemistry (Woodall et al. 2007), lists some important chemical processes that have been calculated for molecular cloud-like conditions. The rates for some of these

2. Chemistry in the comet-forming region

processes need to be recalculated for use in protoplanetary disk chemical networks, using the appropriate values for density, temperature, dust parameters, and radiation field. Cosmic ray-induced UV photo-dissociation is one example of the type of processes for which rates are calculated in the UMIST literature using molecular cloud-like grain parameters and H₂ abundances (Sternberg et al. 1987; Gredel et al. 1989). In protoplanetary disks, dust grains are larger than in molecular clouds due to aggregation and coagulation processes (D’Alessio et al. 2001; Natta et al. 2007; Dominik et al. 2007). Therefore, the overall grain surface and the local UV dust extinction will be smaller under protoplanetary disk conditions than under molecular cloud conditions. Here, we calculate the cosmic ray-induced UV (CRUV) photoprocess rates using the appropriate dust grain parameters.

In the work by Dalgarno et al. (see Sternberg et al. 1987; Gredel et al. 1987, 1989) on the interstellar medium and molecular clouds (on which the UMIST06 (Woodall et al. 2007) CRUV rates are based), the local extinction of cosmic ray-induced UV photons is dominated by dust grains; the gas contribution to the extinction is not considered to be important. However, in protoplanetary disks the gas composition can be very different from that of the interstellar medium or molecular clouds (e.g. high abundances of CH₄) which can significantly increase the gas opacity. It is then possible that in some regions of the disk CRUV photons can be absorbed much more efficiently by the gas than by the dust.

The general understanding of photodesorption is getting more detailed nowadays (Andersson & van Dishoeck 2008; Arasa et al. 2010). When a photon hits an adsorbed molecule it can photodissociate it, instead of directly desorbing the ice species into the gas phase. The products of this dissociation can either recombine on the surface or desorb individually. In the case of water, molecular dynamics studies of a pure water ice layer that is hit by a UV photon show that a water molecule is often desorbed as OH+H instead of desorbing intact (Andersson & van Dishoeck 2008; Arasa et al. 2010). The effect of this constant OH formation channel through grains may drastically alter the gas-phase chemical evolution.

We can safely neglect the gas opacity at distances of approximately 10 AU in our model, because most of the material is frozen on the dust grain surface, thereby suppressing the gas phase abundances of many molecules. However, as we get closer to the star, the temperature is high enough to keep molecules in the gas phase. At 1 AU the gas opacity is therefore important for the chemical evolution. Another factor to consider is that gas-phase processes involving line absorption will be affected by the local temperature conditions. This implies that CRUV photodissociation cross

sections will have to be recalculated and integrated properly into the rate equations. This is the subject of Chapter 3 (Chaparro Molano & Kamp 2012b).

The structure of this Chapter is the following. In Section 2.2 we explain how we use the results of the disk modeling code `ProDiMo` (Woitke et al. 2009) as input for our model. Next we explain the role of cosmic rays (Section 2.3), including an appropriate calculation (i.e. following protoplanetary disk grain parameters) of cosmic ray-induced UV photoprocesses in a low-gas environment. Section 2.4 consists of a comprehensive account of the gas-grain chemical model including adsorption-desorption mechanisms. Section 2.5 deals with the setup for the chemical evolution model, including an estimate of the initial set of chemical abundances that apply for a protoplanetary disk. In Section 2.6 we explore the full chemical networks at the comet formation zone, comparing the chemical abundances with those measured in cometary bodies. In Section 2.7 we discuss the chemical effects of H₂O ice photodesorbing into OH+H instead of desorbing intact. A discussion of our results in Section 2.8 is followed by our conclusions (Section 2.9), in which we summarize the main results of this Chapter.

2.2 Disk Model

For the sake of consistency, the disk structure used here is taken from the model of a passive disk around a T Tauri star obtained with the steady-state disk modeling code `ProDiMo` (Woitke et al. 2009). This approach is valid because the accretion rate is negligible and transport processes occur on longer timescales than the ones modeled in this paper. The position of the region under study within the disk structure (from the simulation) is illustrated in Fig. 2.1. The location at 10 AU from the star corresponds to a likely location for comet formation, in which the density remains fairly high ($n_{\text{H}}=10^{10} \text{ cm}^{-3}$) if compared to molecular cloud conditions and the temperature is quite low ($T=20 \text{ K}$). The CO and H₂O adsorption-desorption processes are most significant at such low temperatures¹. Studying the change in chemical composition as a function of density while keeping a constant temperature is equivalent to moving in a direction perpendicular to the plane of the disk: disk models are vertically isothermal at high optical depth. Table 2.1 summarizes all relevant input parameters.

The grain size distribution in a quiescent protoplanetary disk is assumed to follow a power-law distribution $f(a)\sim a^{-p}$ with $p=3.5$ and a in the range 0.1-10 μm (Woitke

¹In those regions, the gas and grain temperatures are coupled, i.e. $T_{\text{gas}} = T_{\text{dust}}$ (Woitke et al. 2009).

2. Chemistry in the comet-forming region

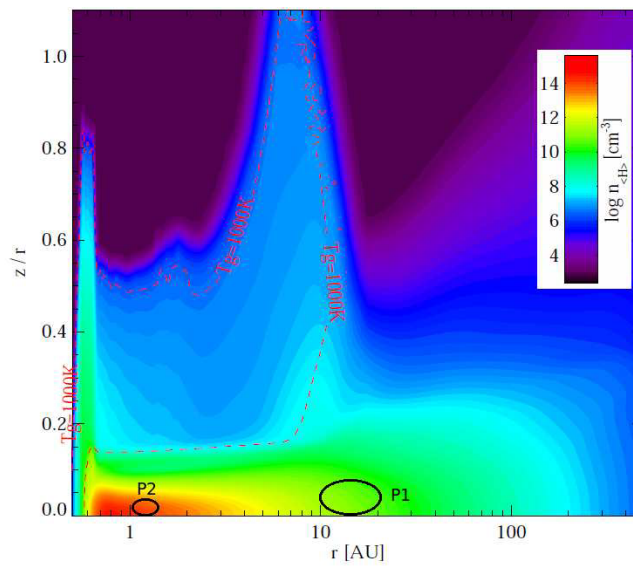


Figure 2.1: Density structure (total hydrogen nuclei number density $n_{(\text{H})}$) of a T Tauri disk model as function of radial distance from the star r and the relative height z/r . Gas in thermal balance. The red dashed line shows the temperature boundary where $T_g = 1000$ K. The regions under consideration for this Chapter are shown as black ovals (P1, and P2 for benchmarking). This figure is taken from the ProDiMo simulation (Woitke et al. 2009).

et al. 2009). This value of p is also used for grains in molecular clouds (Weingartner & Draine 2001), but a_{\min} and a_{\max} are different, reflecting the overall smaller grain sizes in the interstellar medium (ISM): in the much denser protoplanetary disk environment aggregation processes and dust settling to the midplane produce larger sized grains on average. For example, D’Alessio et al. (2001) show the median Taurus SED and models it with an ISM grain size distribution and also with a distribution with larger grains on average. The latter is shown to fit much better. This grain growth causes a reduction of the average surface area of the grains, which limits their ability to absorb UV photons.

Dust settling in the midplane could lead to a lower gas-to-dust ratio than the typical value used here (Woitke et al. 2009). This decreases dust extinction in the top layers in the disk (i.e. these layers become almost transparent), which allows the UV radiation to penetrate deeper towards the midplane. This means that the $A_V=1$ line is shifted to a lower height above the midplane. However, this effect can be compensated by the increased dust UV extinction in the midplane due to the enhanced dust-to-mass ratio. To isolate the effect of larger dust grains on the CR-induced UV field, here we stick to the grain parameters used in previous ProDiMo papers and keep the value 100 for the gas-to-dust mass ratio.

The local UV flux (in $\text{erg}\cdot\text{cm}^{-3}$) of the star and the ISM is frequently given in units of a Draine field (Weingartner & Draine 2001; Lee 1984). The strength of the UV field is then provided via the dimensionless quantity χ (which is 1 for the ISM),

$$\chi = \int_{91.2\text{ nm}}^{205\text{ nm}} \lambda u_\lambda d\lambda \left/ \int_{91.2\text{ nm}}^{205\text{ nm}} \lambda u_\lambda^{\text{Draine}} d\lambda \right. . \quad (2.1)$$

The full 2D radiative transfer treatment in ProDiMo (which uses the same grain parameters, as stated in Table 2.1) yields that for regions close to the midplane of the disk ($z/r < 0.05$ and $0.7 < r < 10$ AU the disk is opaque to the stellar and interstellar UV photons and thus the local UV field strength is very low, $\chi \simeq 0.001$ (Woitke et al. 2009). Hence, UV photoreactions will only play a minor role here when compared to the effects of cosmic rays.

A cosmic ray-induced UV (CRUV) field is present in most regions of the disk (Prasad & Tarafdar 1983; Cecchi-Pestellini & Aiello 1992). This field can cause photodissociation reactions to take place at regions with high optical depth in the disk. However, CRUV photons are created locally and are assumed to be absorbed by the surrounding material (i.e. gas and dust grains) that is locally present. This means that the most appropriate treatment of CRUV photoreactions requires calculating the

2. Chemistry in the comet-forming region

UV field created by cosmic-ray ionization of molecular hydrogen, accounting for dust grain surfaces as a possible sink for these UV photons by using the appropriate (local) grain properties, and also for the effects of gas opacity when the local conditions require. This will be discussed further in the following section.

2.3 Cosmic rays

Cosmic rays play a very important role in the chemistry because they can pervade most regions of a protoplanetary disk. Shen et al. (2004) have calculated that a cosmic-ray iron nucleus with an energy ranging from 20-1000 MeV will lose less than 1% of its energy when passing through a dense molecular cloud. Their influence can be intense in highly obscured regions ($A_V \geq 5$) where most stellar or interstellar UV radiation cannot penetrate (Roberts et al. 2007). Umebayashi & Nakano (1981) found that cosmic rays get effectively attenuated at a column density above $\Sigma \sim 150 \text{ g cm}^{-2}$. In the particular disk model used here, the column density at 1 AU is not high enough to provide a significant extinction of cosmic rays. Choosing a steeper surface density distribution or a smaller outer radius could make the midplane opaque to cosmic rays at greater distances from the star. In Leger et al. (1985) the total flux for cosmic-ray particles with energies higher than 0.02 GeV/nucleon in the ISM is calculated to be

$$\Phi_{\text{CR}}^{\text{H}} = \int_{0.02}^{\infty} \phi_{\text{H}}(\epsilon) d\epsilon = 1.0 \text{ CR cm}^{-2} \text{ster}^{-1} \text{s}^{-1} . \quad (2.2)$$

The amount of cosmic rays that are present can also be measured from the CR ionization rate of H_2 , ζ_{H_2} . A recent work by Indriolo et al. (2007) shows that column densities of H_3^+ (a tracer of H_2 ionization) vary in different molecular clouds. From their work, we pick a conservative value for ζ_{H_2} , which agrees with previous calculations obtained from measured cosmic ray spectra (Cecchi-Pestellini & Aiello 1992)

$$\zeta_{\text{H}_2} = 5 \times 10^{-17} \text{ s}^{-1} . \quad (2.3)$$

2.3.1 Impact on chemistry

Cosmic rays play an important role in molecular cloud chemistry (Herbst & Klemperer 1973; Shen et al. 2004): reactions with the CR-generated H_3^+ and He^+ are of special significance for CO/ H_2O gas formation and destruction in the gas phase. Both H_3^+ and He^+ can dissociate CO and also SiO, which is an important player in H_2O formation. He^+ is created from He+CR reactions, which happen at the same rate as H_2 ionization (see Eq. (2.3)) because they have approximately the same stopping power

Table 2.1: Table of modeling parameters, following Woitke et al. (2009). The symbol # identifies an ice-phase species.

Parameter	Symbol	Value
Disk mass	M_D	$0.01 M_\odot$
Dust-to-gas mass ratio	ρ_d/ρ_g	0.01
Minimum dust grain size	a_{\min}	$0.1 \mu\text{m}$
Maximum dust grain size	a_{\max}	$10 \mu\text{m}$
Grain size power-law index	p	3.5
Grain material mass density	ρ_{gmd}	$2.5 \text{ g}\cdot\text{cm}^{-3}$
Grain mass density	ρ_d	$2.16 \times 10^{-26} \cdot n_{\langle\text{H}\rangle} \text{ g}$
Grain number density	n_{dust}	$4.6 \times 10^{-14} \cdot n_{\langle\text{H}\rangle}$
Local UV field strength	χ	10^{-3}
Dust opacity (UV, 100 nm)	κ_{UV}	$6.8 \times 10^3 \text{ cm}^2 \cdot \text{g}^{-1}$
Cosmic ray ionization rate (H_2)	ζ_{H_2}	$5 \times 10^{-17} \text{ s}^{-1}$
Adsorption site area	A_{site}	$6.67 \times 10^{-16} \text{ cm}^2$
Number of active layers	N_{Lay}	2
Grain CR “duty-cycle”	$f(70 \text{ K})$	3.16×10^{-19}
Grain albedo at 150 nm	ω	0.57
CO Photodesorption yield	$Y_i (\text{CO}\#)$	2.7×10^{-3}
H_2O Photodesorption yield	$Y_i (\text{H}_2\text{O}\#)$	1.3×10^{-3}
CH_4 Photodesorption yield	$Y_i (\text{CH}_4\#)$	10^{-3}
CO_2 Photodesorption yield	$Y_i (\text{CO}_2\#)$	10^{-3}
CO Adsorption energy	$E_i^b (\text{CO}\#)$	960 K
H_2O Adsorption energy	$E_i^b (\text{H}_2\text{O}\#)$	4800 K
CH_4 Adsorption energy	$E_i^b (\text{CH}_4\#)$	1100 K
CO_2 Adsorption energy	$E_i^b (\text{CO}_2\#)$	2000 K

2. Chemistry in the comet-forming region

(Herbst & Klemperer 1973). H_3^+ is created after $\text{H}_2 + \text{CR}$ collisions occur, which enable ionized molecular hydrogen to rapidly react with H_2

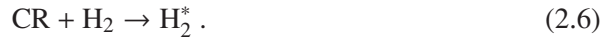
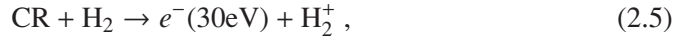


As an important side effect, excited H_2^+ will also emit Werner and Lyman UV photons that can photodissociate otherwise stable species such as CH_4 (Prasad & Tarafdar 1983). The presence of CR-induced UV photons can change the overall chemical balance through efficient ion-molecule chemical pathways.

For processes such as photodesorption, we need to calculate the local CRUV flux, N_{CU} , while for CRUV photoprocesses we need to recalculate the efficiencies given the revised dust properties. The effects of gas opacity can be neglected at 10 AU, as most of the material is frozen on the grain surface, and gas abundances are low. The next two sections discuss this in more detail.

2.3.2 Cosmic ray-induced UV photon flux

The effect of cosmic rays on molecular hydrogen is twofold: ionization and direct excitation (Cecchi-Pestellini & Aiello 1992)



Fifty-five percent of all electrons produced in reaction (2.5) will excite molecular hydrogen to excited electronic states (Sternberg et al. 1987):



Excited electronic states of H_2 via (2.6) and (2.7) spontaneously decay to the $B^1\Sigma_u^+$ and the $C^1\Sigma_u$ states, which then decay to the ground electronic state $X^1\Sigma_g^+$ and emit Lyman and Werner UV photons in the wavelength range 90 – 170 nm:



This is called the Prasad-Tarafdar mechanism (Prasad & Tarafdar 1983).

We calculate the flux of locally generated cosmic ray-induced UV photons (in $\text{cm}^{-2}\text{s}^{-1}$) based on the work of Cecchi-Pestellini & Aiello (1992):

$$N_{\text{CU}} \simeq 12\,500 \frac{1}{1 - \omega} \left(\frac{\zeta_{\text{H}_2}}{5 \times 10^{-17} \text{ s}^{-1}} \right) \left(\frac{2 \times 10^{-21} \text{ cm}^2}{\sigma_{\langle \text{H} \rangle}^{\text{UV}}} \right) \left(\frac{n_{\text{H}_2}/n_{\langle \text{H} \rangle}}{0.5} \right) . \quad (2.9)$$

2.3 Cosmic rays

Here $\omega = Q_{\text{sca}}/(Q_{\text{sca}} + Q_{\text{abs}})$ is the grain albedo at 90 – 170 nm, and $\sigma_{\langle\text{H}\rangle}^{\text{UV}}$ is the grain UV extinction cross section per hydrogen nucleus. The factor $n_{\text{H}_2}/n_{\langle\text{H}\rangle}$ is included because CRUV photons are generated by H₂ molecules, so their number should depend on the local H₂ abundance.

We calculate ω and $\sigma_{\langle\text{H}\rangle}^{\text{UV}}$ for the protoplanetary disk grain size distribution discussed in Section 2.2 using the appropriate dust opacity κ_{UV} (see Table 2.1):

$$\sigma_{\langle\text{H}\rangle}^{\text{UV}} = \kappa_{\text{UV}} \frac{\rho d}{n_{\langle\text{H}\rangle}} = 1.47 \times 10^{-22} \text{ cm}^2. \quad (2.10)$$

The UMIST database uses a standard molecular cloud value for the UV extinction cross section (Sternberg et al. 1987)

$$\sigma_{\langle\text{H}\rangle}^{\text{UV}} = 2 \times 10^{-21} \text{ cm}^2. \quad (2.11)$$

Such a divergence in $\sigma_{\langle\text{H}\rangle}^{\text{UV}}$ can be expected for a protoplanetary disk-like grain size distribution, since it favors large grains that do not provide significant extinction at short wavelengths when compared to a molecular cloud-like grain size distribution (Weingartner & Draine 2001). With this, it is possible to estimate a value for the CRUV photon flux under protoplanetary disk conditions, assuming that most of the H in the gas is stored in molecular hydrogen²:

$$N_{\text{CU}} \simeq 386\,000 \text{ photons cm}^{-2}\text{s}^{-1}. \quad (2.12)$$

Here N_{CU} is 13.6 times more than the value implicitly used in Sternberg et al. (1987) (i.e. in the UMIST database) and approximately 40 times higher than previous estimates for CRUV fields in molecular clouds (Shen et al. 2004):

$$N_{\text{CU}} \simeq 10\,000 \text{ photons cm}^{-2}\text{s}^{-1}. \quad (2.13)$$

Comparing our value for N_{CU} with the stellar and interstellar UV field in the midplane (which is approximately 190 000 photons cm⁻²s⁻¹) and considering direct cosmic-ray ionization processes, it follows that cosmic-rays can be a major driver of the chemistry in the midplane of the disk. Aikawa et al. (1999) reached a similar conclusion based on the estimate of cosmic-ray extinction by Umebayashi & Nakano (1981).

²This remains valid as long as molecular cloud-like abundances are used as initial conditions of the protoplanetary disk model.

2. Chemistry in the comet-forming region

2.3.3 Cosmic ray-induced UV photodissociation

The secondary field of cosmic ray-induced UV photons discussed in Section 2.3.2 has the same effect on the overall chemistry as stellar or interstellar UV radiation, via photodissociation/ionization of gas species and photodesorption of ice species. CR-induced photoprocesses are listed in the UMIST database (Woodall et al. 2007) using data from Sternberg et al. (1987) and Gredel et al. (1989). The cosmic-ray-induced photodissociation efficiency describes the competition for the locally generated UV photons between a species i and the rest of the gas and dust grains:

$$\tilde{\gamma}_i = \int \frac{P(\nu)\sigma_i(\nu)}{\sigma_{\text{tot}}(\nu)} d\nu. \quad (2.14)$$

Here $\sigma_i(\nu)$ is the photoprocess cross section (Lee 1984), $P(\nu)$ the H_2 line emission probability (Lyman and Werner lines in a de-excitation transition of H_2 from a CR-induced 30 eV electron excitation), and $\sigma_{\text{tot}}(\nu)$ is the total extinction (of both gas and grain) cross section:

$$\sigma_{\text{tot}}(\nu) = \sigma_{\langle\text{H}\rangle}^{\text{UV}}(1 - \omega) + \sum_j \frac{n_j}{n_{\langle\text{H}\rangle}} \sigma_j(\nu). \quad (2.15)$$

Dust UV extinction is assumed to be larger than gas UV extinction in molecular cloud-like conditions (Sternberg et al. 1987; Cecchi-Pestellini & Aiello 1992). However, for protoplanetary disk-type chemical abundances this only applies if the local gas-phase abundances are low, as is the case at 10 AU. Ignoring the contribution of the gas opacity, the efficiency is then written as

$$\tilde{\gamma}_i = \int \frac{\sigma_i(\nu)P_i(\nu)}{\sigma_{\langle\text{H}\rangle}^{\text{UV}}(1 - \omega)} d\nu = \frac{1}{1 - \omega} \gamma_i. \quad (2.16)$$

The reaction rate coefficient is usually calculated by considering that CRUV photons are generated in a proportional amount to the CR ionization rate of H_2 ,

$$k_{\text{CU},i} = \zeta_{\text{H}_2} \frac{1}{1 - \omega} \gamma_i. \quad (2.17)$$

The previous expression ignores that CRUV photons are created from *single* H_2 molecules, as opposed to hydrogen nuclei. For this reason the UMIST06 database corrects the photodissociation efficiencies from Gredel et al. (1989) by a factor 2, which is assumed to be the value for $n_{\langle\text{H}\rangle}/n_{\text{H}_2}$ in molecular clouds. For this reason we include the factor $n_{\text{H}_2}/n_{\langle\text{H}\rangle}$ explicitly in the CRUV photo-dissociation rate:

$$k_{\text{CU},i} = 2 \frac{\zeta_{\text{H}_2}}{1 - \omega} \left(\frac{T_g}{300 \text{ K}} \right)^\beta \frac{n_{\text{H}_2}}{n_{\langle\text{H}\rangle}} \gamma. \quad (2.18)$$

Table 2.2: Table of chemical species in the chemical networks.

Type	Symbol
Atoms	H, He, C, O, S, Si, Mg, Fe
Ions	He ⁺ , Si ⁺ , Fe ⁺ , H ⁻ , H ⁺ , C ⁺ , O ⁺ , S ⁺ , Mg ⁺
Molecules	H ₂ , H ₂ O, CH ₂ , HCO, SiO, CO ₂ , SiH, CH ₃ , CH ₄ , OH, O ₂ , CO, CH
Molecular Ions	HCO ⁺ , CH ₂ ⁺ , H ₃ ⁺ , SiH ⁺ , SiO ⁺ , CH ₄ ⁺ , H ₃ O ⁺ , H ₃ O ⁺ , SiH ₂ ⁺ , CH ₅ ⁺ , CH ₃ ⁺ , H ₂ O ⁺ , SiOH ⁺ , CH ⁺ , H ₂ ⁺ , O ₂ ⁺ , CO ⁺ , OH ⁺ , CO ₂ ⁺
Ice species ^a	H ₂ O#, CO#, CH ₄ #, CO ₂ #

a: # stands for an ice-phase species.

The exponent $\beta=1.17$ accounts for the fact that some species are photo-issociated by discrete line absorption (Woodall et al. 2007; Gredel et al. 1987). For all other species other than CO, this parameter is zero. Using our new value for $\sigma_{(H)}^{UV}$ in Eq. (2.10), CRUV photodissociation processes will be up to 13.5 times more efficient due to the reduced grain extinction³.

2.4 Chemical model

The rate equations that describe the time-dependent chemistry (and chemical channels) of a gas-grain system comprise chemical reactions of the following types:

- gas-phase reactions: reactions between species that are present in the gas phase such as ion-molecule, recombination, charge transfer, neutral-neutral reactions, photo-dissociation and cosmic ray-induced processes.
- adsorption-desorption processes: reactions that take species from the gas phase into the solid phase (on the surface of the grain) or vice versa, usually driven by the local temperature, cosmic rays, and the local UV radiation field (stellar, interstellar and cosmic ray-induced).

³This factor is 13.5 when compared to the UMIST rates, which are based on a standard molecular cloud-like dust UV extinction cross section. The factor 40 comes from the comparison to conservative estimates of the CRUV photon flux in molecular clouds, as in the previous section.

2. Chemistry in the comet-forming region

- surface-surface reactions: reactions that occur on the surface of the grain, between species that are present in the solid phase.

Surface-surface reactions are beyond the current scope of this Chapter, so only the first two are considered here. The 53 chemical species used here are listed in Table 2.2.

The rate equation for the chemical network under study is a system of kinetically coupled differential equations. For a gas-phase species i , it is written as

$$\frac{dn_i}{dt} = R_i^+ - R_i^- . \quad (2.19)$$

Here R_i^+ is the rate that characterizes all processes that have the species i as a product, and R_i^- is the rate that describes all processes that decrease the abundance of the species i . For an ice species⁴ $i\#$, the rate equation accounts for adsorption-desorption processes:

$$\frac{dn_{i\#}}{dt} = k_i^a n_i - k_i^d n_{i\#} . \quad (2.20)$$

The four most important desorption processes considered here are thermal, photo-, cosmic ray-induced photo-, and direct cosmic-ray desorption:

$$k_i^d = k_i^{d,th} + k_i^{d,ph} + k_i^{d,cr} + k_i^{d,cu} . \quad (2.21)$$

It should be noted that we did not include X-ray desorption processes, which are very important near the inner rim, because the rates for these processes have not been determined beyond order-of-magnitude estimations (Walsh et al. 2010).

2.4.1 Adsorption

Adsorption is the process that allows a species in the gas phase to adhere to the surface of a grain upon collision. Since the grain is assumed to be immersed in a well-stirred gas at a temperature T_g , a constant flux of gaseous molecules (each with mass m_i) is hitting the surface of the grain with an average thermal velocity of

$$v_i^{th} = \sqrt{\frac{kT_g}{2\pi m_i}} . \quad (2.22)$$

For a number density of dust grains n_{dust} , a sticking probability $S = 1$, and an average grain surface area of $4\pi\langle a^2 \rangle$ the rate is

$$k_i^a = 4\pi\langle a^2 \rangle S v_i^{th} n_{dust} . \quad (2.23)$$

⁴The # symbol identifies an ice-phase (frozen on a grain surface) species i .

Adsorption becomes more efficient (i.e. acts on shorter timescales) as the gas density increases, given that more particles per volume are impinging on grains. The largest variation in the sticking parameter S comes from the temperature-to-adsorption-energy ratio (see Fegley 2000). In Burke & Hollenbach (1983) a complete parameter-space exploration of the sticking probability yields that under protoplanetary disk-like conditions the chemical balance does not change significantly, which seem to be confirmed by experimental results in Öberg et al. (2009). Parameters for adsorption are given in Table 2.1.

2.4.2 Desorption

Desorption processes counterbalance the complete depletion of species due to freeze-out. It should be noted that the details of the various desorption processes are not very well understood, are based on very few laboratory experiments, and use extreme simplifications (Roberts et al. 2007).

Thermal desorption

Thermal desorption is a process in which the temperature of the dust grain can cause some of the ice-phase species bound to its surface to evaporate. The rate at which this happens depends on a characteristic binding energy E_i^b :

$$k_i^{\text{d,th}} = \nu_i \exp\left(-\frac{E_i^b}{kT_d}\right). \quad (2.24)$$

This Arrhenius-type expression for the thermal desorption rate is theoretical in nature, and the constant ν_i can be estimated from the vibrational frequency associated to the bond that holds the ice-phase species on the surface of the grain. This is based on the Polanyi-Wigner equation for a single desorption process, ignoring rotational degrees of freedom (Holloway & Beeby 1975; Galwey & Brown 1999):

$$\nu_i = \sqrt{\frac{2n_{\text{surf}}kE_i^b}{\pi^2 m_i}}. \quad (2.25)$$

Here $n_{\text{surf}} = 1/A_{\text{site}} = 1.5 \times 10^{15} \text{ cm}^{-2}$ is the number density of available adsorption sites per unit grain area (Herbst 1993). Parameters for thermal desorption are given in Table 2.1.

2. Chemistry in the comet-forming region

Photodesorption

Photodesorption occurs when a UV photon hits a specific adsorption site on the surface of the grain. The rate of this process can be written as

$$k_i^{\text{d,ph}} = \pi \langle a^2 \rangle \frac{n_{\text{dust}}}{n_{\text{act}}} Y_i \chi F_{\text{Draine}} . \quad (2.26)$$

This rate describes a Draine UV field⁵ impinging on the grain surface, and desorbing a species i . The photodesorption yield Y_i is measured in the laboratory using a UV field comparable in strength to the Draine field (see Öberg et al. 2009). Given that the ice mantle on the grain surface is composed of many layers, the rate has to account for an incoming photon only being able to process a fraction of the icy molecules that are adsorbed onto the grain surface. This number of active sites on the grain surface is

$$n_{\text{act}} = 4\pi \langle a^2 \rangle n_{\text{dust}} n_{\text{surf}} N_{\text{Lay}} . \quad (2.27)$$

Here $N_{\text{Lay}} = 2$ is the number of layers of ice that can be affected by an incoming UV photon. The expression for the photodesorption rate in Eqn. (2.26) can then be rewritten as

$$k_i^{\text{d,ph}} = \frac{\chi F_{\text{Draine}}}{4 n_{\text{surf}} N_{\text{Lay}}} Y_i . \quad (2.28)$$

Consequently, the rate for this process depends only on the amount of surface adsorption sites, the photodesorption yield, and the local flux of UV photons. This process can become important when the timescale for thermal desorption is large, such as for H₂O at temperatures below 120 K. Parameters for photodesorption are given in Table 2.1.

Most species are assumed to photodesorb intact. However, this is not always the case for water, as reported in molecular dynamics studies by Andersson & van Dishoeck (2008) and Arasa et al. (2010). Most of the time (70%) a water ice molecule that is hit by a UV photon will dissociate and subsequently desorb into an OH molecule and an H atom. This means that there is only a 30% chance that the water molecule will desorb intact. It should be noted that this special case of water ice desorption does not change the photodesorption yield value. Here it is assumed that desorption occurs only for the first two layers of frozen material on the grain surface. When considering deeper layers, less than half of the water ice molecules desorb as water vapor. The effect on the overall chemical evolution of this special desorption case for water will be explored in Section 2.7.

⁵A value for the flux produced by this field $F_{\text{Draine}} \approx 2 \times 10^8 \text{ cm}^{-2} \text{ s}^{-1}$ is given in Woitke et al. (2009). The wavelength range for this field is given in Section 2.2 above.

Table 2.3: List of the most significant initial abundances of species used in the chemical networks.

Pre-molecular cloud (Atomic)		Molecular cloud (Post-modeling)	
Symbol	$\log(n_X/n_{\text{H}})$	Symbol	$\log(n_X/n_{\text{H}})$
H	0	H ₂	-0.301
He	-1.125	He	-1.125
O	-3.538	CO	-3.939
C	-3.886	H ₂ O#	-4.129
Si	-5.1	O	-4.56
Fe	-5.367	CO ₂ #	-4.575
Mg	-5.377	O ₂	-4.977
S	-5.721	SiO	-5.1
		Fe	-5.367
		Mg	-5.377
		H	-5.57
		H ₂ O	-5.798
		S	-5.721

2. Chemistry in the comet-forming region

Cosmic ray-induced UV photodesorption

This photodesorption process is identical to regular photodesorption, except for the source of UV photons. Therefore, by replacing the stellar and interstellar UV energy density χF_{Draine} in Eq. (2.28) by the appropriate CRUV photon flux for a proto-planetary disk N_{CU} in Eq. (2.12), the cosmic ray-induced UV photodesorption rate becomes

$$k_i^{\text{d,cu}} = \frac{N_{\text{CU}}}{4n_{\text{surf}}N_{\text{Lay}}} Y_i . \quad (2.29)$$

Direct cosmic ray desorption

Grain heating by cosmic rays as described by Hasegawa & Herbst (1993) happens when a cosmic ray passes through a disk and hits a dust grain, heating it up to an estimated temperature of 70 K. This causes species to thermally desorb from the grain as they would from thermal desorption at 70 K. Iron nuclei have been found to be the most important contributors to grain heating (Leger et al. 1985). For an iron-to-hydrogen ratio of approximately $[\text{Fe}/\text{H}] \approx 1.6 \times 10^{-4}$, it is possible to estimate the rate at which cosmic rays hit an $a \approx 0.1 \mu\text{m}$ grain:

$$R_{\text{CR}} = \Phi_{\text{CR}}^{\text{Fe}} \pi \langle a^2 \rangle = 3.16 \times 10^{-14} \text{ s}^{-1} . \quad (2.30)$$

The timescale for successive CR-grain hits is then $\tau_{\text{CR}} \approx 10^6$ yr. Given that the estimated cooling time for a silicate grain that goes from $T=70$ K to $T=20$ K is on the order of 10^{-5} s, we can find the ratio between the cooling and heating timescales⁶ with

$$f(70 \text{ K}) = \frac{\tau_{\text{cool}}}{\tau_{\text{CR}}} = 3.16 \times 10^{-19} . \quad (2.31)$$

This is called the ‘‘duty-cycle’’ of the grain heating by cosmic rays (Hasegawa & Herbst 1993). The ‘‘duty-cycle’’ modulates the thermal desorption at $T=70$ K, scaled to the CR ionization rate of H_2

$$k_i^{\text{d,cr}} = f(70 \text{ K}) R_i^{\text{d,th}}(70 \text{ K}) \zeta_{\text{H}_2} . \quad (2.32)$$

2.5 Gas-grain chemistry model

The time-dependent chemical network used for this model is `chem_compact`, which is based on Milica Milosavljevic & Inga Kamp’s `chemistry` code (Milosavljević

⁶Calculation of this value requires knowledge of the specific heat obtained from indirect measurements, which means that it is highly dependent on T and thus may not be valid for high (> 150 K) dust temperatures.

2008). This code is a time-dependent solver of the gas-phase chemical rate equation and has been originally used to explore the role of shocks in protoplanetary disks. It uses the UMIST database for astrochemistry (Woodall et al. 2007), which identifies all relevant chemical reactions for a set of chosen species. We use the ordinary differential equation (ODE) solver `vode`, which is specifically designed to solve stiff ODEs with strong and sudden time variations, such as the rate equation for a chemical network of any size (Brown et al. 1989). This code has previously been benchmarked against steady state abundances, and in addition we make our own benchmark against ProDiMo (Woitke et al. 2009) steady state abundances in Section 2.5.2.

Additionally, we include adsorption-desorption reactions for CO, CO₂, CH₄, and H₂O, and a new calculation of grain parameters for an appropriate treatment of CRUV photoprocesses for protoplanetary disk-like grain parameters (see Section 2.3). We checked for the effects of incorporating other significant ice species such as O₂ and SiO ice to our network, and found no significant differences from our results. At 10 AU, O₂ and SiO ice are formed, but because adsorption is very efficient, it is necessary for them to be formed in the gas phase first. In future Chapters, when we also consider surface reactions, we will incorporate adsorption for all gas-phase species.

2.5.1 Initial conditions

Assuming that the material has been processed before the formation of the disk, the initial abundances for the protoplanetary disk model were computed from molecular cloud-like conditions⁷. The chemical model was evolved from atomic conditions (see Table 2.3, left column) in a gas of density $n_{\text{(H)}} = 10^6 \text{ cm}^{-3}$, temperature $T = 20 \text{ K}$ and $\chi = 0.01$ for 10^7 years. The final chemical abundances for this run (see Table 2.3, right column) were used as input for the initial chemical abundances⁸ in the different protoplanetary disk models studied here. A similar approach has been used by Thi et al. (2011).

We studied the chemical evolution under two different conditions for each point of interest: using a low (molecular cloud-like) and high (protoplanetary disk-like) value for the CRUV field. Thus we can see how the chemical abundances and pathways change as the protoplanetary disk-sized grains absorb less CRUV photons.

⁷This means that the molecular cloud values for the UV grain extinction cross section (Eq. 2.11) were used in the CRUV photo-rates (Eqns. 2.18 and 2.29).

⁸The O₂ and H₂O abundances under molecular cloud-like conditions are inconsistent with current observations of the ISM (Hollenbach et al. 2009). However, we found that formation of O₂ and H₂O in our protoplanetary disk model does not depend on their initial abundance.

2. Chemistry in the comet-forming region

2.5.2 Chemistry benchmarking at 1 AU

For the sake of consistency, we tested the solver against the steady-state chemistry in `ProDiMo` (Woitke et al. 2009), by comparing the results at a distance of 1 AU from the star, near the midplane of the disk (P2 in Fig. 2.1): $T = 80$ K, $n_{\langle H \rangle} = 10^{14}$ cm $^{-3}$ and $\chi = 0.001$. For the purpose of matching the results of both models, we used a low (molecular cloud-like) value for the $\sigma_{\langle H \rangle}^{\text{UV}}$ and ignore the effects of CRUV desorption.

In the `ProDiMo`-simulated chemistry at 1 AU all the oxygen is trapped in H₂O ice ($n_{\text{H}_2\text{O}\#}/n_{\langle H \rangle} \simeq 10^{-4}$), and all the carbon in methane gas ($n_{\text{CH}_4}/n_{\langle H \rangle} \simeq 10^{-4}$), which implies a low abundance of gas-phase CO ($n_{\text{CO}}/n_{\langle H \rangle} \simeq 10^{-6}$) and consequently a very low atomic oxygen abundance ($n_{\text{O}}/n_{\langle H \rangle} \simeq 10^{-12}$). `chem_compact` yields very similar results, although on a much larger timescale than the lifetime of the disk ($\tau \sim 10^8$ yr). Therefore in this case, steady state abundances in the midplane have to be treated with caution. This has been pointed out by Woitke et al. (2009)- see their Fig. 13.

2.6 Chemistry in the comet-formation zone

In the midplane of the disk at a distance of 10 AU from the central star, the density of our model is $n_{\langle H \rangle} = 10^{10}$ cm $^{-3}$ and the temperature is $T = 20$ K, corresponding to the region P1 in Fig. 2.1. Even though photo-desorption here is more efficient than thermal desorption, it acts at a timescale much longer than the disk's lifetime. These conditions are ideal for ice formation on grains, which means that carbon and oxygen will be trapped on the surface of grains and will not efficiently form gas-phase molecules. The chemical evolution in this region of the disk is plotted in Figs. 2.2 and 2.3, corresponding to a low and a high CRUV flux, respectively.

From these figures it follows that while the local CRUV field does not radically change the chemical balance, it does have an effect. This will be discussed in Section 2.6.2. It should also be noted that cosmic-ray ionization of H₂ and He has a very big impact on the chemistry, even though those rates are not affected by the dust grain parameters. The formation pathways that we describe in the following section apply to both low and high CRUV flux conditions.

2.6.1 Chemical pathways

The final abundances and time evolution of CO shows that it suffers depletion on a typical timescale of 10^6 yr. This suggests that H₂O is more efficiently formed than CO on long timescales, removing oxygen from the gas phase and trapping it into

2.6 Chemistry in the comet-formation zone

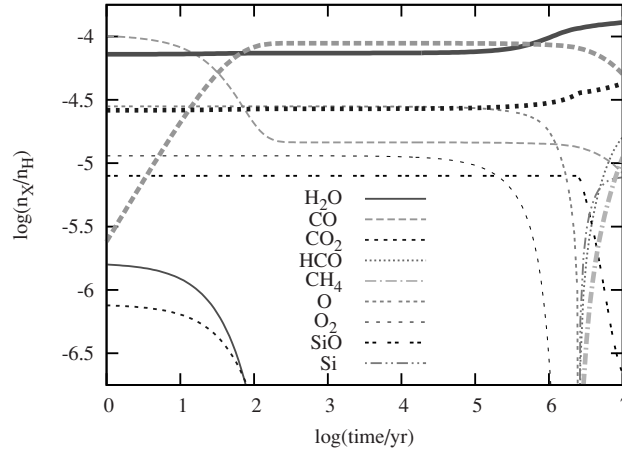
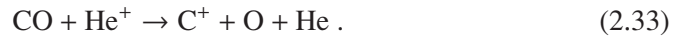


Figure 2.2: Example of the time evolution of gas/ice abundances (thin/thick lines) using the standard ISM value for $\sigma_{\langle H \rangle}^{\text{UV}} = 2 \times 10^{-21} \text{ cm}^2$. The disk parameters correspond to point P1 in Fig. 2.1 ($n_{\langle H \rangle} = 10^{10} \text{ cm}^{-3}$ and $T = 20 \text{ K}$).

water ice. The main processes that create CO, H₂O and other related species are illustrated in Figs. 2.4 and 2.5, where the gray pathways indicate CRUV photodissociation.

Figure 2.3 shows that after 100 yr, CO ice is the main carbon carrier. Excluding adsorption, the main reaction destroying gas-phase CO is



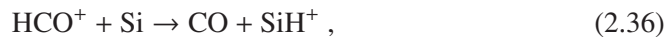
It should be remembered that He⁺ is created by cosmic-ray ionization of He. C⁺ created in this reaction will undergo charge exchange with other atoms (Si, Mg, Fe) to form atomic carbon, which then reacts very efficiently via radiative association with H₂ to form CH₂:



In turn, CH₂ reacts with atomic oxygen to again form CO:



This reaction is very fast because atomic oxygen is steadily produced by He⁺ dissociation of CO in reaction (2.33). CO is also formed from HCO⁺, either in the Si-reaction,



2. Chemistry in the comet-forming region

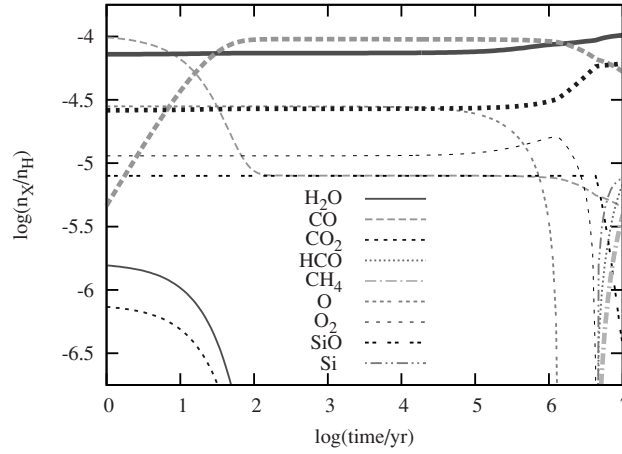
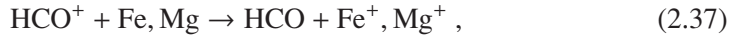
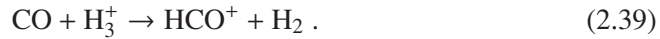


Figure 2.3: Example of the time evolution of gas/ice abundances (thin/thick lines) using an appropriate $\sigma_{\langle H \rangle}^{UV} = 1.5 \times 10^{-22} \text{ cm}^2$ for a protoplanetary disk. See text in Section 2.6.2 for a discussion of these results. The disk parameters correspond to point P1 in Fig. 2.1 ($n_{\langle H \rangle} = 10^{10} \text{ cm}^{-3}$ and $T = 20 \text{ K}$).

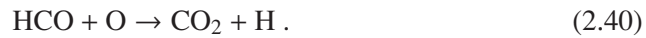
or via HCO



an HCO^+ can itself be formed from CO via H_3^+

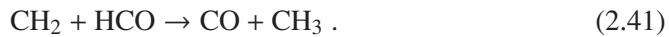


However, this HCO^+ -CO feedback cycle is not closed because CO_2 can also be formed from HCO:



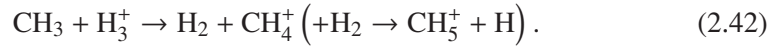
After formation, CO_2 is rapidly frozen, at the expense of a significant fraction of CO. This reduces the carbon available for CO ice formation.

CO_2 ice is more abundant in Fig. 2.3 than in Fig. 2.2 at the expense of water, HCO and CH_4 . The long timescale for CH_4 ice formation is due to the chemical pathways that create CH_4 from CO. They are activated via CR-induced dissociation of CH_3 , which acts on a timescale of approximately $8 \times 10^6 \text{ yr}$. CH_3 is created from HCO and CH_2

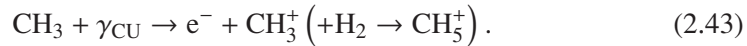


2.6 Chemistry in the comet-formation zone

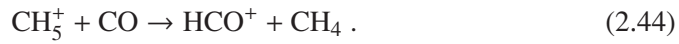
The first and most important pathway starts from H_3^+ -dissociation of CH_3 . It should be noted that H_3^+ is created after cosmic-ray ionization of H_2 :



The second pathway is started by CRUV photo-ionization of CH_3 (which is half as efficient as He^+ dissociation):



Thus, if CH_3 is efficiently dissociated, CH_5^+ will be efficiently formed. CH_5^+ is only one step away from forming CH_4 :



This reaction is more efficient at forming HCO^+ than reaction (2.39). After CH_4 is formed, it is rapidly adsorbed onto the grain surface.

SiO forms H_3O^+ in reactions with He^+ , which can form SiO again via OH . This feedback cycle is broken on the same timescale as the freeze-out of water, which causes the SiO abundance to decrease on long timescales (see Figs. 2.2 and 2.3). The $\text{SiO}/\text{H}_2\text{O}$ feedback cycle goes as follows:



Then, H_3O^+ efficiently forms H_2O via dissociative recombinations (Bates 1986; Sternberg et al. 1987):



This reaction creates water vapor fairly efficiently on a timescale of 0.06 yr. However, there is another dissociative recombination reaction with Si , driven by the high abundance of atomic silicon formed in reaction (2.45):



The previous cycle continuously generates water vapor that can rapidly be adsorbed onto the grain surface. This chain of reactions is very efficient because no other processes are creating O^+ , OH^+ or H_2O^+ .

2. Chemistry in the comet-forming region

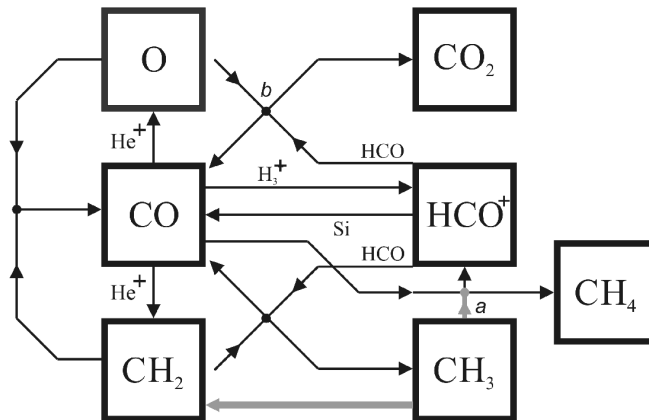


Figure 2.4: Final (10^7 yr) chemical network for CO and CH₄ at P1 in Fig. 2.1 ($n_{\text{H}} = 10^{10} \text{ cm}^{-3}$ and $T = 20 \text{ K}$), where the low temperature freezes CH₄ after its gas-phase formation at 10^6 yr, as seen in Fig. 2.3. The lines represent reactions between species on the diagram, with arrows pointing at the product(s) of each reaction. Gray lines: Cosmic ray-induced photodissociation reactions. (Notes: *a*. Via $\gamma_{\text{CRUV}}/\text{H}_3^+ \rightarrow \text{CH}_3^+/\text{CH}_4^+ \rightarrow \text{CH}_5^+$. *b*. $\text{HCO}^+ + \text{O} \rightarrow \text{CO}_2 + \text{H}$ or $\text{HCO}^+ + \text{O} \rightarrow \text{CO} + \text{OH}$.)

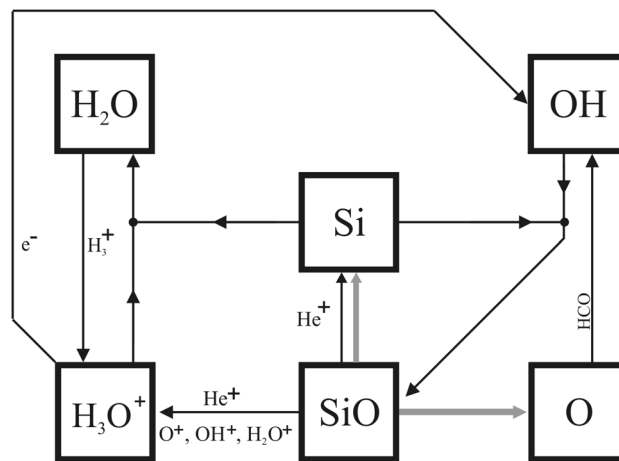


Figure 2.5: Final (10^7 yr) chemical network for H_2O at P1 in Fig. 2.1 ($n_{(\text{H})} = 10^{10} \text{ cm}^{-3}$ and $T = 20 \text{ K}$). The lines represent reactions between species on the diagram, with arrows pointing at the product(s) of each reaction. Gray lines: Cosmic ray-induced photo-dissociation reactions.

2. Chemistry in the comet-forming region

On the other hand, water (in the gas phase) can go back to H_3O^+ via H_3^+



The dissociative recombination of H_3O^+ and an electron can also create OH



OH is a low-abundance but rapid catalyst for SiO formation



However, since OH forms SiO about ten times faster than SiO forms H_3O^+ , SiO will be steadily formed within 10^6 yr, despite constant dissociation by CRUV photons. When we freeze all the water formed in reaction (2.50), then the reaction (2.51) will be interrupted, and the OH-fueled SiO formation cycle is broken. Thus, even though CRUV photodissociation of water vapor into OH and H can favor SiO formation over water on long timescales, in neither case (low or high CRUV field) can we produce enough OH to keep high abundances of SiO in the gas phase after a few Myr, as seen in Figs. 2.2 and 2.3. SiO is depleted after a few Myr because its formation pathway, reactions (2.45) to (2.50), is disrupted by freeze-out of water.

2.6.2 The effect of CRUV enhancement

Besides being important drivers for the later evolution of the chemistry, as seen in the previous section, CRUV photons affect different species in different ways. This is evident when comparing the chemistry that arises in the low and high CRUV flux environments, as seen in Figs. 2.2 and 2.3. For instance, since CH_3 has an estimated higher cross section than CO and CH_4 , it is more susceptible to CRUV photodissociation. Thus, when the CRUV flux is enhanced, the CH_4 formation pathways will be slowed down and its abundance will decrease. Also, even though there will more carbon available for CO formation, gas-phase CO will be more efficiently dissociated than CO_2 . This shows in Fig. 2.3, where we see the (final) CO_2 ice abundance increasing more (27%) than the gas-phase CO (7%) in the low CRUV flux case, in Fig. 2.2.

This CO_2 ice enhancement comes at the expense of water, which decreases about 20% in abundance because of CRUV photodissociation. This process enhances the OH abundance, and this shows how SiO can survive for a few more million years (as noted in the previous section). This shift in abundances is further proven by the long-term availability of atomic oxygen (formed in the photodissociation of CO and SiO), which in the high CRUV flux case is depleted a few hundred thousand years later than in the low CRUV flux case.

2.6 Chemistry in the comet-formation zone

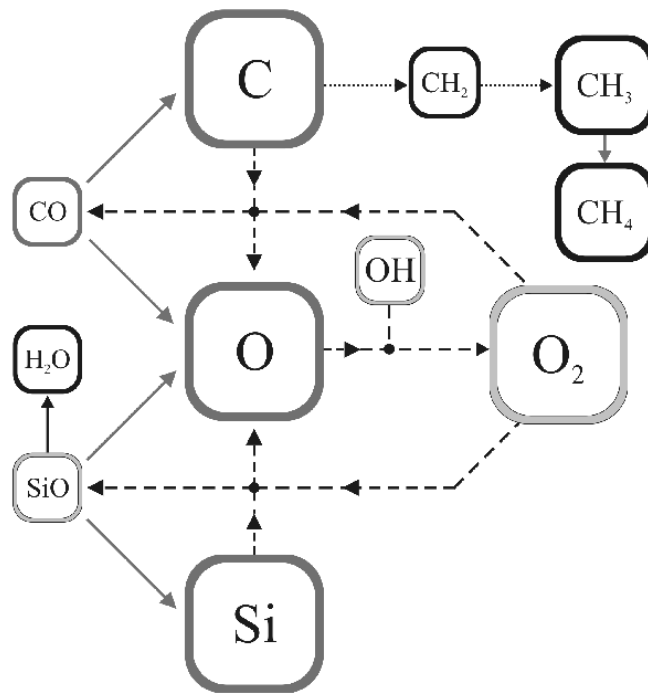


Figure 2.6: Schematic chemical network for a protoplanetary disk, showing the competition of some chemical species (H_2O , CO , $\text{CH}_{3,4}$, SiO , O_2) for the carbon, silicon, and oxygen, depending on whether there is high OH formation or not. The lines represent reactions between species on the diagram, with arrows pointing at the product(s) of each reaction. The dotted branches correspond to a chemical network where OH is not being efficiently formed. The dashed branches replace the dotted pathways when OH is being efficiently created, thus taking away oxygen from H_2O to form CO , SiO , O_2 , and atomic oxygen. The gray arrows represent CRUV photodissociation processes.

2.7 Alternative H₂O photodesorption mechanism

Molecular dynamics simulations by Andersson & van Dishoeck (2008) and Arasa et al. (2010) show that the effect of UV photons impinging on water ice molecules is more destructive than previously thought. Before these studies, water molecules were believed to desorb intact into the gas phase after being expelled from the grain surface by a UV photon. However, water molecules are not desorbed instantaneously after the UV photon hits them: almost every single photon-water molecule interaction will result in photodissociation of the water molecule into OH and H. Most of the time (70%), these byproducts will leave the surface in the gas phase. However, it is also possible (30%) that the OH and H recombine on the surface, and the energy left over from this reaction will cause the newly formed water ice molecule to desorb into the gas phase.

The main processes that create CO, H₂O, and other related species are summarized in Fig. 2.6 schematically showing the chemical network depicted in Figs. 2.4 (for CO, CO₂, and CH₄) and 2.5 (for H₂O and SiO). They also show CRUV photodissociation processes and the new pathways arising from having an efficient OH formation mechanism.

When water ice photodesorbs intact at P1 (Fig. 2.7, corresponding to the final abundances in Fig. 2.3) most of the oxygen is in H₂O, CO, and CO₂ ice, and a fraction of carbon is in CH₄ ice (see 2.6). When water ice partially desorbs into OH and H (Fig. 2.7) the efficient OH formation enables the oxygen in water to be stored elsewhere, such as in atomic oxygen and SiO. Now all the carbon is trapped in CO and CO₂ thanks to OH-driven CO formation (see Fig. 2.6).

The main chemical products of a high CRUV field present are atomic oxygen and, to a lesser degree, OH. Atomic oxygen, which is now very abundant will react very efficiently with desorbed OH to form O₂



This means that carbon and silicon photodissociated from CO and SiO will react with O₂ to form CO and SiO at approximately the same rate (while other carbon carriers like CH₄ are rapidly photo-dissociated):



This feedback pathway arising from a highly efficient OH-forming mechanism enables the long-term gas-phase formation of O₂ and SiO that can later freeze on the

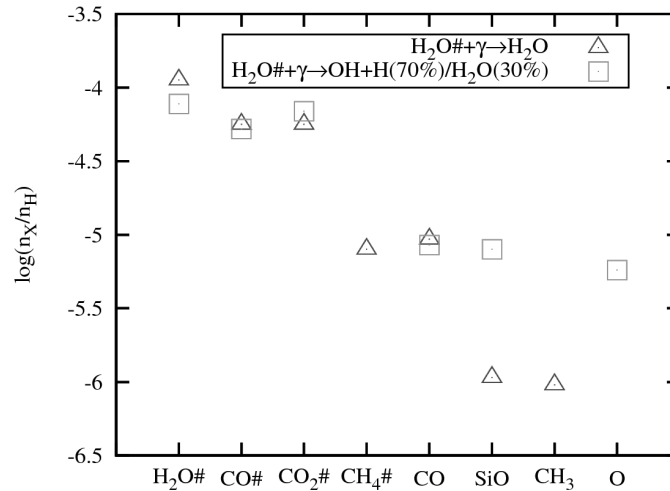


Figure 2.7: Final (10^7 yr) abundances of significant species at the comet-forming region (P1 in Fig. 2.1). Triangles: Water ice photodesorbs intact (Fig. 2.3). Squares: Water vapor is partially photodissociated into OH + H. Plot obtained using an appropriate $\sigma_{(H)}^{UV}$ for a protoplanetary disk and for a [C/O] ratio of 0.46.

dust grain surface. Now that carbon forms CO via O_2 and not via CH_2 as in reaction (2.35), the byproducts CH_3 and CH_4 are not being efficiently formed, and CO becomes the main carbon carrier. The final chemical abundances resulting from having this special case of water desorption in P1 (see Fig. 2.1) is depicted in Fig. 2.7.

2.8 Discussion

In this Chapter we focus on the timescales in which gas-grain chemical processes can take place in passive, nonaccreting disks. We thus assume that the density and temperature of the midplane will stay approximately constant during our simulation. We discuss the main results drawn from our study of the gas-grain chemical timescales in relation to observables such as the composition of cometary ices.

2.8.1 Implications for comet formation

Ice formation for different molecules takes place at different times because desorption processes act different timescales. This is evident in Fig. 2.3, where CO ice is more abundant than water ice between 10^2 and 10^6 yrs. After this the ice content resembles

2. Chemistry in the comet-forming region

what is observed in cometary ices⁹ (Bockelée-Morvan et al. 2004; Bockelée-Morvan 2010), where the predominant form of ice is H₂O, followed by CO and CO₂ ice and, to a lesser degree, CH₄ ices. CH₄ ice is formed after a few million years, and only after water ice formation has become so efficient that it takes away most of the oxygen from CO and leaves the carbon free to form other molecules. This suggests that the CH₄ ice found in comets was formed very late in the disk evolution.

A comparison between measured cometary ice abundances and our resulting ice abundances is presented in Table 2.4. Our resulting $n_{\text{CO}\#}/n_{\text{CO}_2\#}$ and $n_{\text{CH}_4\#}/n_{\text{H}_2\text{O}\#}$ ratios are very close to the cometary values, which means that the relative abundances of ice species are predicted by our model to some extent. Furthermore, when we attempted to increase T (i.e. moving radially toward the star) or reduce $n_{\langle\text{H}\rangle}$ (i.e. moving vertically away from the midplane) in order to decrease the adsorption rates, we ended up with a very different $n_{\text{CO}\#}/n_{\text{CO}_2\#}$ ratio, due to the high volatility of CO compared to CO₂. This means that the conditions at P1 are optimal for formation of comet-like ice abundances.

This conclusion is unique to the density-temperature combination rather than to the exact location in the midplane of the disk. If the temperature changes by 10 K, different ice abundances will vary in a nonuniform way due to the different binding energies of the chemical species; for example, at 10 K CH₄ ice is about 100 times less abundant because it cannot be formed efficiently. At 30 K thermal desorption of CO is so efficient that most of it stays in the gas phase. Also, if the density changes, the gas chemistry that drives the formation of ices via adsorption changes, so the particular ice structure will also change. At a density of 10^{11} cm^{-3} , CO adsorption is so efficient that the gas-phase CH₄ formation processes are not efficient, and again lead to a CH₄ ice abundance that is 100 times less than in the 10 AU case. At a density of 10^9 cm^{-3} , CO₂ ice becomes twice as abundant as CO ice. Thus, a difference of an order of magnitude in density or 10 K in temperature will drastically change the ice composition.

The reason for the discrepancy between the measurements of Bockelée-Morvan (2010) and our results stems from the fact that the carbon-to-oxygen ratio is much lower in observed cometary ices (~ 0.16) than in our model (~ 0.45). The reason behind this could be that some carbon is bound in dust that we consider here to be in the gas phase. In other words, as the sum of the carbon in the ices and in the gas phase is the total amount of carbon considered in our model, a fraction may be stored

⁹Even though ice ratios can vary among individual comets (see Bockelée-Morvan et al. 2004), the general composition $n_{\text{H}_2\text{O}\#} > n_{\text{CO}\#} > n_{\text{CO}_2\#} > n_{\text{CH}_4\#}$ is fairly consistent.

Table 2.4: Ice ratios in comets compared to our results at two different epochs.

Ratio	Cometary measurements ^a	c_c ^b : [C/O]=0.45		c_c ^c : [C/O]=0.16
		10 ⁶ yr	10 ⁷ yr	10 ⁷ yr
$n_{\text{CO}_2\#}/n_{\text{CO}\#}$	<0.6	0.65	1	0.43
$n_{\text{CO}\#}/n_{\text{H}_2\text{O}\#}$	<0.2	0.6	0.45	0.14
$n_{\text{CO}_2\#}/n_{\text{H}_2\text{O}\#}$	0.02-0.12	0.39	0.6	0.06
$n_{\text{CH}_4\#}/n_{\text{H}_2\text{O}\#}$	0.003-0.015	0.001	0.06	<0.001

a: Abundances compiled from cometary measurements in Bockelée-Morvan et al. (2004); Bockelée-Morvan (2010). *b*: Ratios from our chem_compact (c_c) model using a [C/O] ratio of 0.45 (see Fig. 2.3). *c*: Ratios from our chem_compact model using a (cometary) [C/O] ratio of 0.16.

in refractory grain cores. Because of this we changed the [C/O] ratio in our model to the cometary value, which yielded the results in the right column of Table 2.4. These results fit the cometary $n_{\text{CO}\#}/n_{\text{H}_2\text{O}\#}$ and $n_{\text{CO}_2\#}/n_{\text{H}_2\text{O}\#}$ ratios more closely.

2.9 Conclusions

Our time-dependent chemical network is compiled from the UMIST database for astrochemistry (Woodall et al. 2007), adsorption-desorption processes for H₂O, CO, CO₂, and CH₄ (Woitke et al. 2009), and an appropriate treatment of CRUV photoprocesses (Cecchi-Pestellini & Aiello 1992) for protoplanetary disks.

In the midplane of a protoplanetary disks, the steady formation of H₂O and CO and their relation to secondary oxygen and carbon carriers, such as CO₂, CH₃, CH₄ and SiO in the gas phase, are caused by recombination of ionized species. The presence of ionized material comes from an internal UV field, which in the dark, cold midplane reaches the floor level caused by cosmic ray interactions with the gas. Thus CRUV photons become the main driver of the chemistry. Locally generated UV photons can either photodissociate a molecule in the gas phase or impinge on the surface of a dust grain and photodesorb a frozen molecule.

By calculating grain parameters (such as the UV albedo and extinction cross section) for the grain size distribution appropriate for a protoplanetary disk, we find a CRUV photon flux of 380 000 photon cm⁻²s⁻¹, which is 40 times larger than conser-

2. Chemistry in the comet-forming region

vative estimates for molecular clouds (Prasad & Tarafdar 1983; Cecchi-Pestellini & Aiello 1992; Shen et al. 2004; Roberts et al. 2007). Also, CRUV photodissociation processes can be up to 13.5 times more efficient in the midplane of a protoplanetary disk than in a similar molecular cloud-like environment. This can be curbed by the effects of gas opacity in warmer regions of the disk (closer to the star than 10 AU), which will be the subject of our next Chapter.

Cosmic ray-induced UV photons are responsible for the destruction of CH_3 (which favors CO formation) and formation of CH_4 . Since CH_4 and CO_2 are more sensitive to CRUV photodissociation than CO, CO will mostly compete with H_2O as the most abundant oxygen-bearing species for the region of the disk that we probed here ($r \sim 10$ AU). Carbon and oxygen are efficiently trapped in ices in the midplane of the disk because the desorption timescales are longer than the lifetime of the disk.

The chemical abundances and their evolution change drastically whenever there is a mechanism that efficiently forms OH. A high formation rate of OH implies that O_2 , SiO, and atomic oxygen will be efficiently formed, often at the expense of part of the oxygen in H_2O . Also, all the carbon will tend to be stored in CO instead of CH_4 .

At 10 AU the only way to enhance OH formation is by photodesorbing water into OH+H. Even an enhanced CRUV field does not have any effect on OH formation because adsorption of gas molecules as soon as they are formed is very efficient at 20 K. When OH is not formed via photo-processing of water ice, we obtain ice-on-grain abundances and ratios that are comparable to those measured in comets (Bockelée-Morvan et al. 2004; Bockelée-Morvan 2010). One important instance is the formation of CH_4 ice, for which we obtained a timescale of a few Myr. This timescale is limited by (cosmic-ray generated) He^+ dissociation of CH_3 .

The sensitivity of these ice ratios to temperature and density provide strong evidence that cometary ices must have formed under conditions similar to the ones used here, and most likely at late evolutionary stages (after a few Myr). This also means that the measured ice composition of comets precludes their formation in an OH-rich environment.

Acknowledgments We would like to thank W.-F. Thi and P. Woitke for many helpful discussions on the effects of grain growth and on the physics behind CRUV processes, and M. Milosavljevic for providing us with the basis for the current `chem_compact` code. Finally, we thank the anonymous referee and the A&A Editor Malcolm Walmsley for helping us clarify important aspects of this Chapter.

3 The role of OH in the chemical evolution of protoplanetary disks

II. Gas-rich environments

—G. Chaparro Molano & I. Kamp—

Astronomy & Astrophysics 547, A7 (2012)

*Every life is inexplicable, I kept telling myself.
No matter how many facts are told,
no matter how many details are given,
the essential thing resists telling.
— Paul Auster, The New York Trilogy —*

3. Chemistry in gas-rich environments

Abstract

Context. We present a method for including gas extinction of cosmic-ray-generated UV photons in chemical models of the midplane of protoplanetary disks, focusing on its implications on ice formation and chemical evolution.

Aims. Our goal is to improve on chemical models by treating cosmic rays, the main source of ionization in the midplane of the disk, in a way that is consistent with current knowledge of the gas and grain environment present in those regions. We trace the effects of cosmic rays by identifying the main chemical reaction channels and also the main contributors to the gas opacity to cosmic-ray-induced UV photons. This information is crucial in implementing gas opacities for cosmic-ray-induced reactions in full 2D protoplanetary disk models.

Methods. We considered time-dependent chemical models within the range 1-10 AU in the midplane of a T Tauri disk. The extinction of cosmic-ray-induced UV photons by gaseous species was included in the calculation of photorates at each timestep. We integrated the ionization and dissociation cross sections of all atoms/molecules over the cosmic-ray-induced UV emission spectrum of H₂. By analyzing the relative contribution of each gas phase species over time, we were able to identify the main contributors to the gas opacity in the midplane of protoplanetary disks.

Results. At 1 AU the gas opacity contributes up to 28.2% of the total opacity, including the dust contribution. At 3-5 AU the gas contribution is 14.5% of the total opacity, and at 7-8 AU it reaches a value of 12.2%. As expected, at 10-15 AU freeze-out of species causes the gas contribution to the total opacity to be very low (6%). The main contributors to the gas opacity are CO, CO₂, S, SiO, and O₂. OH also contributes to the gas opacity, but only at 10-15 AU.

3.1 Introduction

The midplane of protoplanetary disks has been considered a dead zone, because the lack of a source of ionization prevents the development of magneto-rotational instabilities, which are thought to drive the accretion process. The midplane of a disk corresponding to a Class II source around a T Tauri star is opaque to stellar and interstellar UV (van Zadelhoff et al. 2001; Woitke et al. 2009) and X-ray (Glassgold et al. 2007; Aresu et al. 2011) photons, which corresponds to a region located at $z/r < 0.05$ and $1 < r < 10$ AU. However, most regions of the midplane are far from being dead zones because of cosmic rays, which directly ionize the gas and heat the dust grains. An important consequence of the interaction of cosmic rays and H_2 molecules is the emission of a locally generated UV field that can ionize/dissociate species. More specifically, regions that have a value for A_V of a few are dominated by cosmic-ray processing, since they can penetrate column densities of $\Sigma \sim 150 \text{ g cm}^{-2}$ (Umebayashi & Nakano 1981).

Hence, the midplane of the disk between 1 and 10 AU can be viewed as a cosmic-ray dominated region, where cosmic rays are the main source of ionization and therefore the main driver of the chemical evolution. Steady-state chemical models applied to these regions cannot fully describe the chemical evolution of the midplane, as the chemical relaxation timescale can be as long as 10^8 yr (Woitke et al. 2009), which is longer than the lifetime of the disk (Fedele et al. 2010; Haisch et al. 2010; Semenov & Wiebe 2011). For this reason it is necessary to approach the study of the chemical evolution of the disk from a time-dependent model. One of the main catalysts of the cosmic-ray driven chemistry in these regions is OH (Chaparro Molano & Kamp 2012a, Chapter 2), especially for the formation of CO and H_2O .

Current chemical models of protoplanetary disks include to a large extent the effects of cosmic rays, whether they model the chemistry using steady-state (Woitke et al. 2009; Willacy & Woods 2009; Gorti et al. 2011; Thi et al. 2011) or time-dependent (Visser et al. 2009, 2011; Walsh et al. 2010; Semenov et al. 2010) solutions. However, the effects of the local gas opacity and grain growth in cosmic-ray-induced UV processes are largely overlooked, as the parameters for estimating cosmic-ray-induced photoionization/dissociation rates are usually taken from molecular cloud literature (Gredel et al. 1989; Woodall et al. 2007).

In molecular cloud modeling (Cecchi-Pestellini & Aiello 1992; Shen et al. 2004) it is customary to ignore those effects, as they are not relevant for the cold, gas-poor environment present deep inside molecular clouds and the interstellar medium (ISM).

3. Chemistry in gas-rich environments

Table 3.1: Distance from the star, temperature, and density conditions corresponding to mid-plane regions in the protoplanetary disk structure in Fig. 3.1, following the ProDiMo simulation of a passive irradiated disk (Woitke et al. 2009). The stellar parameters used in this simulation are found in Table 3.2.

r (AU)	T (K)	$n_{\langle H \rangle}$ (cm^{-3})
1	80	10^{14}
3-4	65	10^{12}
7-8	40	10^{11}
10-15	20	10^{10}

Another important factor to consider is grain growth in protoplanetary disks, which reduces dust UV opacity compared to molecular clouds¹. This leads to an enhancement in the cosmic-ray-induced UV flux (Chaparro Molano & Kamp 2012a, Chapter 2) with respect to previous ISM based estimates (Shen et al. 2004), especially in gas-poor regions. This field, which is enhanced by a factor 40 at 10 AU, drives gas phase formation pathways for saturated molecules that can later freeze on the dust surface. Wherever the physical conditions allow for penetration of cosmic rays in disks, our analysis of cosmic-ray driven chemistry applies. Since we aim to perform a quantitative analysis, we chose the physical conditions from a particular disk model. However, our results do not depend on that particular choice.

This chapter is structured as follows. The strategy to implement our model in Section 3.2 is followed by a discussion of the physical conditions in gas-rich regions of the disk midplane in Section 3.3. In Section 3.4 we discuss our treatment of cosmic-ray-induced UV photoprocesses including the effects of gas opacity. Section 3.5 deals with the particulars of our chemical model, followed by a summary (Section 3.6) and a discussion (Section 3.7) of our results. Finally, the main conclusions from this Chapter are summarized in Section 3.8.

¹See D'Alessio et al. (2001) for evidence of grain growth from spectral energy distributions of protoplanetary disks

3.2 Methodology

Our goal is to identify the main chemical contributors to the extinction of cosmic-ray-induced UV (CRUV) photons in different regions of the midplane of a T Tauri disk. The temperature in the disk midplane can be high enough to prevent species from freezing onto the surface of grains immediately after their gas phase formation. This general freeze-out of chemical species is found to happen at distances beyond approximately 10 AU. Thus, we chose the 1-10 AU range of the disk midplane in this Chapter, because the temperature and density conditions are ideal for studying regions with very different gas compositions. For example, the temperature at 7-8 AU (see Table 3.1) coincides with the onset of thermal desorption of CO, which will evaporate from the surface of grains while leaving the abundances of other frozen species for the most part unchanged.

The physical input conditions for our chemical evolution models are given by a ProDiMo model (Woitke et al. 2009), and are listed in Tables 3.1 and 3.2. We implemented a time-dependent calculation of the CRUV photorates that includes the extinction provided by the dust and also by gas species, which depends on their abundance. For this reason, we recomputed the CRUV photorate at each timestep of the simulation to account for the changes in gas phase abundances. This extinction was then integrated over the wavelength range and emission probability of CRUV photons. The emission probability was obtained from Lyman and Werner emission lines of H₂ that is excited either by direct cosmic-ray interactions or by secondary electrons generated in cosmic-ray excitation of H₂ (Prasad & Tarafdar 1983).

Using this scheme, we can trace species that have a strong impact on the absorption of CRUV photons for the midplane of T Tauri disks. By taking into account the extinction contribution of dust grains, we can compare it to the gas extinction, thus obtaining a time-dependent value for the opacities over the CRUV wavelength range. We implemented this method in our time-dependent chemical rate equation solver `chem_compact`, which we previously used for studying ice formation in the comet formation zone (Chaparro Molano & Kamp 2012a, Chapter 2) of a passive T Tauri disk with a low accretion rate. This code was benchmarked against steady-state chemical abundances from the ProDiMo simulation from Woitke et al. (2009).

3.3 Gas-rich regions

Cosmic ray-induced UV photons can be absorbed by the material in the local environment where they are generated. Both gas and dust can absorb these photons and

3. Chemistry in gas-rich environments

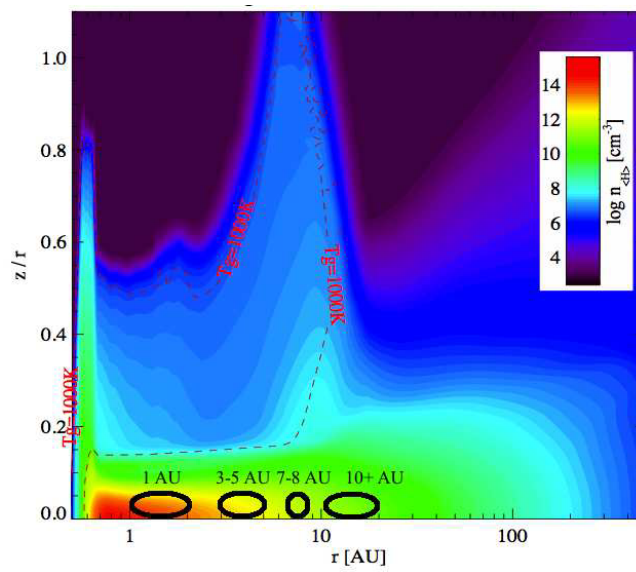


Figure 3.1: Density structure model of a T Tauri disk as a function of radial distance from the star and the relative height, following the ProDiMo simulation (Woitke et al. 2009). The black ovals show the regions of the disk according to Table 3.1. The relevant disk parameters are provided in Table 3.2.

3.3 Gas-rich regions

Table 3.2: Table of modeling parameters.

Parameter	Symbol	Value
Stellar mass	M_*	$1 M_\odot$
Effective temperature	T_{eff}	5770 K
Stellar luminosity	L_*	$1 L_\odot$
Disk mass	M_D	$0.01 M_\odot$
Inner disk radius	R_{in}	0.5 AU
Outer disk radius	R_{out}	500 AU
Gas surface density power law index	ϵ	1.5
Dust-to-gas mass ratio	ρ_d/ρ_g	0.01
Minimum dust grain size	a_{min}	$0.1 \mu\text{m}$
Maximum dust grain size	a_{max}	$10 \mu\text{m}$
Mean molecular weight	μ	1.35
Dust grain size power law index	p	3.5
Dust material mass density	ρ_{gmd}	$2.5 \text{ g}\cdot\text{cm}^{-3}$
Dust grain albedo (UV)	ω	0.57
Dust opacity (UV)	κ_{UV}	$6.8 \times 10^3 \text{ cm}^2\cdot\text{g}^{-1}$
Cosmic ray ionization rate (H_2)	ζ_{H_2}	$5 \times 10^{-17} \text{ s}^{-1}$
Number of active layers	N_{Lay}	2
Adsorption site area	A_{site}	$6.67 \times 10^{-16} \text{ cm}^2$
C adsorption energy	E_b^{C}	630 K
CO adsorption energy	E_b^{CO}	960 K
CO ₂ adsorption energy	$E_b^{\text{CO}_2}$	2000 K
CH ₃ adsorption energy	$E_b^{\text{CH}_3}$	920 K
CH ₄ adsorption energy	$E_b^{\text{CH}_4}$	1100 K
O adsorption energy	E_b^{O}	630 K
O ₂ adsorption energy	$E_b^{\text{O}_2}$	960 K
OH adsorption energy	E_b^{OH}	1000 K
H ₂ O adsorption energy	E_b^{O}	4800 K
Si adsorption energy	E_b^{Si}	2100 K
SiH adsorption energy	E_b^{SiH}	2300 K
SiO adsorption energy	E_b^{SiO}	2800 K
Fe adsorption energy	E_b^{Fe}	3300 K
Mg adsorption energy	E_b^{Mg}	4200 K

3. Chemistry in gas-rich environments

become a source of local extinction, but this depends on the local density and temperature conditions. For instance, at 10 AU most of the material is frozen onto the surface of dust grains, which means that the extinction of CRUV depends entirely on the local dust properties. In the absence of gas extinction, grain aggregation in protoplanetary disks can lead to an enhanced CRUV flux (Chaparro Molano & Kamp 2012a, Chapter 2). In these gas-poor environments CRUV photoprocesses will not be affected by the composition of the gas and the chemistry can be described in a fairly straightforward fashion.

By contrast, in regions closer to the central star the environment is heated up and most of the chemical species will stay in the gas phase while leaving significantly reduced layers of frozen species. Any change in the chemical composition of the gas will either enhance the CRUV field or quench it efficiently, depending on the CRUV cross section of the dominant species in the gas. Thus, if we aim to understand the complex coupling effects between chemistry and CRUV photons, we need to fully incorporate the contribution of the gas in the local CRUV extinction.

In Fig. 3.1 we show the regions under study in a plot of the density structure of the disk obtained using ProDiMo (Woitke et al. 2009), which provides us with a self-consistent hydrostatic structure from which we obtain parameters such as temperature, density, and intensity of the local UV field compared to the ISM Draine field. By studying regions at different distances from the star, we can identify the species that are locally dominant in their CRUV opacity.

The specific temperature and density conditions for each specific region of the disk midplane are found in Table 3.1. Near the inner rim (at 1 AU from the star) we focus on the role of CRUV photoprocesses in the highly efficient OH forming region near the inner rim. Moving farther away from the star, the temperature and the density decrease, which causes more material to freeze onto the surface of dust grains. To understand the role of freeze-out, we probed the disk at two more regions: at 3-4 AU and 7-8 AU. For the 10 AU region we refer the reader to Chapter 2 (Chaparro Molano & Kamp 2012a).

3.4 Cosmic-ray-induced processes

Cosmic rays penetrate to the disk midplane predominantly from the vertical direction because the column density along all other directions is too high. From the analysis of cosmic-ray penetration in Semenov et al. (2004), it follows that in the midplane of the particular generic T Tauri disk chosen in this Chapter (see Table 3.2 for a list

3.4 Cosmic-ray-induced processes

of parameters), at radial distances larger than 1 AU cosmic rays can penetrate almost unhindered. Recent work by Padovani & Galli (2011) on the penetration of cosmic rays in molecular clouds suggests that interaction with magnetic fields is more important than previously thought. However, those results do not necessarily apply for the particular magnetic field geometry of protoplanetary disks, and more detailed modeling is necessary to clear the picture of cosmic-ray and magnetic field interactions.

The main chemical byproducts of direct cosmic-ray ionization are H_3^+ (from H_2^+) and He^+ (Herbst & Klemperer 1973). While He^+ is very good at dissociating molecules and passing on its charge to the products of the reaction, H_3^+ hydrogenates and ionizes CH compounds, and helps create water from atomic oxygen (Chaparro Molano & Kamp 2012a, Chapter 2).

Cosmic rays can also ionize the medium in a more subtle way: by inducing a UV field that comes from secondary ionization of molecular hydrogen. The process, known as the Prasad Tarafdar mechanism (Prasad & Tarafdar 1983), starts when an electron with a typical energy of 30 eV is released after the cosmic-ray ionization of an H_2 molecule. This secondary electron can also ionize another H_2 molecule. A value for the total rate ζ_{H_2} of both direct and secondary ionization of H_2 is not entirely agreed upon, but a conservative value of

$$\zeta_{\text{H}_2} = 5 \times 10^{-17} \text{ s}^{-1} \quad (3.1)$$

has been obtained both for H_3^+ measurements in the ISM (Indriolo et al. 2007) and from theoretical estimations based on measured cosmic-ray spectra (Cecchi-Pestellini & Aiello 1992; Micelotta et al. 2011).

The emitted electron then hits another (neutral) H_2 molecule, which leaves it in an excited electronic state (Sternberg et al. 1987; Riahi et al. 2006), after which it spontaneously decays to the excited vibrational states of the $B \ ^1\Sigma_u^+$ and $C \ ^1\Sigma_u$ levels. In the subsequent decay to excited vibrational states of the ground electronic level $X \ ^1\Sigma_g^+$ of H_2 , Lyman and Werner photons are emitted in the 90-170 nm range. These cosmic-ray-induced UV photons can then either ionize/dissociate a gas species or hit a dust grain.

We define the CRUV photoprocess efficiency as the fraction of CRUV photons that dissociate a species and are not locally absorbed by the gas or dust:

$$\gamma_i = \int_{1.76 \text{ PHz}}^{3.28 \text{ PHz}} \frac{P(\nu)\sigma_i(\nu)}{\sigma_{\text{tot}}(\nu)} d\nu. \quad (3.2)$$

3. Chemistry in gas-rich environments

Here P is the emission probability profile of a CRUV photon, σ_i is the photoprocess cross section (in cm^2 per species), and σ_{tot} is the total (gas+dust) cross section, which is a measure of the local extinction. If a given species with a high CRUV cross section is very abundant in the gas phase, the photo rate of that species will have a maximum value and will be low for all other species in the gas. This shielding effect cannot be ignored in regions where high-density/temperature combinations create a gas-rich environment.

Finally, cosmic rays can directly heat dust grains and cause desorption of ices. We took this effect into account, but it is more predominant in outer regions of the disk.

3.4.1 CRUV emission probability profile

The emission probability profile of CRUV is obtained from the transition probability of the first three electronic levels ($B^1\Sigma_u^+$ and $C^1\Sigma_u$) of molecular hydrogen. The cross section for excitation of H_2 into a level v' is proportional to the optical band oscillator strength $f_{0v'}$.

$$\sigma_{v'0} \propto f_{0v'} . \quad (3.3)$$

We use proportionality here, as it is enough to obtain a normalized emission probability profile. The oscillator strength is

$$f_{0v'} \propto A_{v'0} \frac{g_{v'}}{g_0} \frac{1}{v'^2} . \quad (3.4)$$

Here g is the statistical weight. The emission probability for a transition from the level $v'J'$ of an electronically excited state i to the $v''J''$ level of the ground electronic state is then proportional to the Einstein A coefficient for emission and the cross section for excitation:

$$p(v_{v'J'}^i) \propto \sigma_{v'0}^i A_{v'J',v''J''}^i = f_{0v'}^i A_{v'J',v''J''}^i . \quad (3.5)$$

This probability is normalized over all transitions to $v''J''$ levels of the ground electronic state:

$$P(v_{v'J'}^i) = \frac{f_{0v'}^i A_{v'J',v''J''}^i}{\sum_{v'J'} \sum_{v''J''} f_{0v'}^i A_{v'J',v''J''}^i} . \quad (3.6)$$

Each transition probability is then convolved into a Voigt line profile to account for both natural and thermal broadening:

$$P(v; v_{v'J'}^i) = P(v_{v'J'}^i) \phi_V(v - v_{v'J'}^i) . \quad (3.7)$$

The emission probability profile for each excited electronic state is then

$$P^i(\nu) = \sum_{\nu'J'} P(\nu; \nu'J') . \quad (3.8)$$

Thus, the probability that a CRUV photon will be emitted after an H₂ cosmic-ray ionization process is

$$P(\nu) = P^{B^1\Sigma_u^+}(\nu) + P^{C^1\Sigma_u^+}(\nu) + P^{C^1\Sigma_u^-}(\nu) \quad (3.9)$$

This probability is normalized over the frequency range 1.76 – 3.28 PHz (90-170 nm). We obtained the Einstein *A* coefficients and the frequencies for the relevant transitions from the tables of Abgrall et al. (2000), and the statistical weights were calculated from the guidelines in Appendix A of Ochkin & Kittell (2009).

3.4.2 CRUV gas opacity

The total cross section σ_{tot} in Eq. (3.2) is (in cm² per hydrogen atom)

$$\sigma_{\text{tot}}(\nu) = \tilde{\sigma}_{\langle\text{H}\rangle}^{\text{dust}}(1 - \omega) + \sum_j \xi_j \sigma_j(\nu) . \quad (3.10)$$

Here ω is the grain albedo, $\xi_j = n_j/n_{\langle\text{H}\rangle}$ is the abundance of the species *j*, and $\tilde{\sigma}_{\langle\text{H}\rangle}^{\text{dust}}$ is the grain UV extinction cross section per hydrogen atom. We refer the reader to Eq. (2.10) to see how the cross section relates to the dust UV opacity and other dust parameters in Table 3.2. Since the dust UV extinction curve is fairly flat in the CRUV frequency range, we used a frequency average for this value. Due to photon conservation, the previous expression leads to the following relation:

$$\tilde{\sigma}_{\langle\text{H}\rangle}^{\text{dust}}(1 - \omega)\gamma_{\text{dust}} + \xi_i \gamma_i = 1 . \quad (3.11)$$

Here γ_{dust} is

$$\gamma_{\text{dust}} = \int \frac{P(\nu)}{\sigma_{\text{tot}}(\nu)} d\nu . \quad (3.12)$$

Thus $\xi_i \gamma_i$ measures the fractional contribution from the species *i* to the CRUV extinction. The shape of the radiation field that dissociates or ionizes a species *F*(ν) not only depends on the CRUV emission probability, but also on the CRUV extinction of all other species $\sigma_{\text{tot}}(\nu)$:

$$F(\nu) = \frac{P(\nu)}{\sigma_{\text{tot}}(\nu)} . \quad (3.13)$$

The frequency-dependent opacity for a species *i* can be written as

$$\kappa_i(\nu) = \xi_i \sigma_i(\nu) \frac{n_{\langle\text{H}\rangle}}{\rho_{\text{gas}}} \text{ cm}^2 \text{ g}^{-1} \text{ (gas)} . \quad (3.14)$$

3. Chemistry in gas-rich environments

Table 3.3: Table of chemical species in the chemical networks. # indicates an ice species.

Type	Symbol
Atoms	H, He, C, O, S, Si, Mg, Fe
Ions	He ⁺ , Si ⁺ , Fe ⁺ , H ⁻ , H ⁺ , C ⁺ , O ⁺ , S ⁺ , Mg ⁺
Molecules	H ₂ , H ₂ O, CH ₂ , HCO, SiO, CO ₂ , SiH, CH ₃ , CH ₄ , OH, O ₂ , CO, CH, H ₂ CO
Molecular Ions	HCO ⁺ , CH ₂ ⁺ , H ₃ ⁺ , SiH ⁺ , SiO ⁺ , CH ₄ ⁺ , H ₃ O ⁺ , H ₃ O ⁺ , SiH ₂ ⁺ , CH ₅ ⁺ , CH ₃ ⁺ , H ₂ O ⁺ , SiOH ⁺ , CH ⁺ , H ₂ ⁺ , O ₂ ⁺ , CO ⁺ , OH ⁺ , CO ₂ ⁺
Ice	C#, CO#, CO ₂ #, CH ₃ #, CH ₄ #, O#, O ₂ #, OH#, H ₂ O#, Si#, SiH#, SiO#, Fe#, Mg#

Here $\rho_{\text{gas}} = n_{\langle\text{H}\rangle} \mu m_{\text{H}}$, with μ being the mean molecular weight (see Table 3.2). We can now define a “gray” (frequency averaged) opacity as

$$\langle \kappa_i \rangle = \frac{\int_{1.76 \text{ PHz}}^{3.28 \text{ PHz}} F(\nu) \kappa_i(\nu) d\nu}{\int_{1.76 \text{ PHz}}^{3.28 \text{ PHz}} F(\nu) d\nu}. \quad (3.15)$$

Using Eqs. (3.13) and (3.14) this expression can be rewritten as

$$\langle \kappa_i \rangle = \frac{\xi_i \gamma_i}{\gamma_{\text{dust}} \mu m_{\text{H}}}. \quad (3.16)$$

With this expression, we can accurately measure the opacity of each species throughout a time-dependent chemistry run. The variables ξ_i , γ_i and γ_{dust} are calculated at every timestep of the simulation as part of the CRUV photoprocess rate calculation. Given that the CRUV photoprocess rate constant $k_i \propto \gamma_i$, the resulting rate is then coupled to the abundance of all other species that contribute to the opacity.

Since photoionization/dissociation of species can be continuum and/or line processes, we convolved the line photoprocess cross sections with a Voigt profile in order for both natural and Doppler line broadening. The total cross section is then the sum of the line and continuum processes for each molecule. Values for the cross sections were obtained from the tables in the Leiden photoprocess database

hosted by E. van Dishoeck <http://www.strw.leidenuniv.nl/~ewine/photo/> (van Dishoeck et al. 2006).

It is safe to consider only the effects of dust CRUV extinction if we know *a priori* that most of the gas species are frozen onto the surface of grains. This means that if gas phase abundances are low enough to be neglected in Eq. (3.10), dust grains will be the sole contributor to opacity. This approach is frequently taken in models that include CRUV photoprocesses (Sternberg et al. 1987; Gredel et al. 1987, 1989; Woodall et al. 2007), mostly because it is valid for ISM and molecular cloud conditions (low molecular gas abundances).

At 10 AU the environment is cold enough ($T_{\text{gas}}=20$ K, $n_{\text{H}}=10^{10}$ cm⁻³) to study the chemical evolution without taking into account the gas opacity (Chaparro Molano & Kamp 2012a, Chapter 2). Under these conditions, the CRUV rate constant takes a simplified form that does not depend on species abundances.

3.5 Chemical model

The code `chem_compact`, described in Chapter 2 (Chaparro Molano & Kamp 2012a), is our VODE based (Brown et al. 1989) gas/grain chemical rate equation solver. In it we include a reaction network based on the UMIST06 database for astrochemistry (Woodall et al. 2007) including H₂ formation on grains (Cazaux & Tielens 2002) and ad/desorption reactions: Adsorption and thermal and stellar UV photodesorption from Aikawa et al. (1997b); Leger et al. (1985); Öberg et al. (2009), cosmic-ray direct desorption from Hasegawa & Herbst (1993) and cosmic-ray-induced photodesorption from Roberts et al. (2007). Surface reactions are not considered because they are beyond the scope of this Chapter.

Table 3.3 lists all gas and ice species considered in our model. In this Chapter we use the low metal initial abundances from Jenkins (2009), where absorption lines of these metals are measured² from various clouds against a bright background star. The low abundances imply that Si, Fe, and Mg condense into dust grains before the formation of the disk. This is particularly relevant for the formation of SiO and its maximum abundance levels, although formation of CO and H₂O is not affected.

Initial conditions for our disk model were obtained by running our chemical evolution code under molecular cloud conditions ($T = 20$ K, $n_{\text{H}} = 10^6$ cm⁻³) from

²Despite assuming significant metal depletion, the metal abundances here are about a factor 10 higher than in Graedel et al. (1982) or Lee et al. (1996).

3. Chemistry in gas-rich environments

atomic low-metallicity abundances. The resulting abundances after 10^7 yr were used as initial conditions. Table 3.4 lists the initial abundances for the molecular cloud run (atomic) and those for the disk model. Atomic abundances (column 2 in Table 3.4) were used as input for the molecular cloud run, which yielded the molecular abundances (column 4 in Table 3.4) that we took as initial abundances for our disk model.

We decided to ignore sulphur chemistry beyond ionization of atomic S because its chemical network is only weakly coupled to CO formation and is decoupled from other species considered here (Sternberg & Dalgarno 1995). Atomic sulphur was included as it contributes to the metallicity, and its ionization can be an important source of charge exchange for other species. By ignoring other S-bearing species, we can still arrive at an upper limit for the importance of atomic S in the CRUV gas opacity.

To estimate the effects of gas opacity in the CRUV photoprocess rates and therefore in the chemical evolution, we replaced the relevant rates from the UMIST (Woodall et al. 2007) database with our own rates (Section 3.4). As these rates depend on ξ_i , we recalculated them at every timestep, using the new values for the gas abundances. This means that at every timestep, the integral in Eq. (3.2) needs to be evaluated from the previous timestep.

3.6 Results

To estimate the relevance of gas opacity for protoplanetary disks, we used an estimate of the gas ionization and photodissociation cross sections from Gredel et al. (1989) to compute the mean photo dissociation cross section for various species in the wavelength range of CRUV photons (90-170 nm). Using this value, we computed the abundance that is required for an individual species to produce a gas opacity equal to the dust opacity. We did this for both molecular cloud and protoplanetary disk dust properties.

H₂ does not contribute to the opacity because most of it is in the fundamental vibrational level of the ground electronic state $X^1\Sigma_g^+$. Therefore it is unable to absorb CRUV that are generated in transitions from excited electronic states to vibrationally excited levels of the $X^1\Sigma_g^+$ state.

Using the results from Table 3.5, we can check to which extent the simplifying assumption holds that gas opacity is negligible compared to that of the dust for CRUV photoprocesses. At regions located at distances of $r \lesssim 8$ AU chemical abundances of

Table 3.4: Table of initial abundances, atomic (column 2) and molecular (column 3). The symbol # indicates an ice species.

Species (Atomic)	Abundance ξ_i	Species (Molecular)	Abundance ξ_i
H	1	H ₂	5.00×10^{-1}
He	8.51×10^{-2}	He	8.51×10^{-2}
O	3.31×10^{-4}	CO	1.76×10^{-4}
C	1.78×10^{-4}	H ₂ O#	1.09×10^{-4}
Fe	5.01×10^{-6}	O	3.55×10^{-5}
Mg	2.24×10^{-6}	OH	5.66×10^{-6}
S	1.90×10^{-6}	Fe#	5.01×10^{-6}
Si	1.78×10^{-6}	H	2.56×10^{-6}
		H ₂ O	2.55×10^{-6}
		Mg#	2.24×10^{-6}
		S	1.73×10^{-6}
		H ₂ CO#	1.63×10^{-6}
		SiO#	1.02×10^{-6}

3. Chemistry in gas-rich environments

Table 3.5: Comparison between the gas and dust opacity: average photoprocess cross section (column 2), maximum gas phase abundance required to produce an opacity equal to the dust opacity for ISM type dust (column 3) and for protoplanetary disk type dust (column 4).

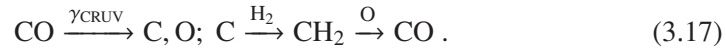
Species (i)	$\bar{\sigma}_i$ (cm ²) (90-170 nm)	Req. $n_i/n_{\langle H \rangle}$ (PPD)	Req. $n_i/n_{\langle H \rangle}$ (ISM)
C	3.85×10^{-18}	3.98×10^{-5}	5.20×10^{-4}
CH	6.61×10^{-18}	2.31×10^{-5}	1.68×10^{-5}
CH ⁺	4.86×10^{-18}	3.15×10^{-5}	4.12×10^{-4}
CH ₂	1.50×10^{-17}	1.02×10^{-5}	9.47×10^{-5}
CH ₃	1.32×10^{-16}	1.16×10^{-6}	1.52×10^{-5}
CH ₄	6.13×10^{-16}	2.50×10^{-7}	3.26×10^{-6}
OH	7.82×10^{-18}	1.96×10^{-5}	2.56×10^{-4}
H ₂ O	4.00×10^{-18}	3.83×10^{-5}	2.87×10^{-4}
Fe	1.80×10^{-18}	8.49×10^{-5}	1.11×10^{-3}
Mg	9.20×10^{-19}	1.66×10^{-4}	4.12×10^{-4}
CO	1.82×10^{-17}	8.40×10^{-6}	1.10×10^{-4}
Si	2.14×10^{-17}	7.14×10^{-6}	9.33×10^{-5}
HCO	2.99×10^{-16}	5.12×10^{-7}	6.69×10^{-6}
SiH	6.35×10^{-17}	2.41×10^{-6}	3.15×10^{-5}
H ₂ CO	3.58×10^{-16}	4.27×10^{-7}	5.59×10^{-6}
O ₂	7.20×10^{-18}	2.13×10^{-5}	5.77×10^{-5}
S	3.36×10^{-18}	4.55×10^{-5}	5.95×10^{-4}
CO ₂	9.10×10^{-18}	1.68×10^{-5}	5.81×10^{-5}
SiO	2.07×10^{-16}	7.41×10^{-7}	9.68×10^{-6}

the listed molecules easily exceed the boundary values of Table 3.5. This means that the effects of gas opacity have to be included in chemical models of the midplane of protoplanetary disks inside 10 AU.

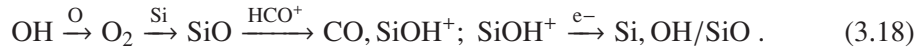
3.6.1 Chemistry at 1 AU

In this region, the moderately high temperature (80 K) ensures that most of the chemical species stay in the gas phase. Adsorption of gas phase H_2O is much more efficient than thermal desorption, which causes gas phase H_2O to have a very low abundance. CO , O_2 , CO_2 , SiO , CH_4 , and oxygen in atomic form are the dominant species in the gas phase, whereas H_2O and to a lesser extent SiO are the only species with a significant ice abundance. Fig. 3.2a shows the time-dependent evolution of the species abundances when considering an appropriate protoplanetary disk dust size distribution³ and including the effects of CRUV gas opacity.

CO is very abundant in the initial conditions run, and remains the most abundant species besides H_2 . CO is kept at this level through two main pathways. It can be photodissociated by CRUV into C and O , which later recombine in the following way:

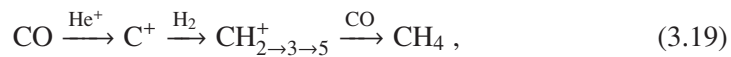


CO is mainly formed via electron recombination of HCO^+ . However, SiO also acts as a catalyst for the formation of CO because its reaction with HCO^+ is very rapid. Hence, whenever SiO is present, it efficiently converts HCO into CO , without SiO having to be very abundant itself. The OH to SiO to CO chemical pathway is the following:



HCO^+ is formed in the reaction of CO with H_3^+ , which as noted above in Section 3.4 is a byproduct of cosmic-ray ionization of H_2 . This cycle ensures a steady supply of OH as a primer for sustained formation of SiO and CO , as seen in Fig. 3.2ab.

CH_4 is also steadily formed from He^+ ionization of CO :



although at a very low abundance (10^{-7}). The latter part of that reaction is curbed because the first step is reversed by O_2 :



³Our choice of dust size distribution parameters is typical of a Class II source, but limited to current knowledge based on observations.

3. Chemistry in gas-rich environments

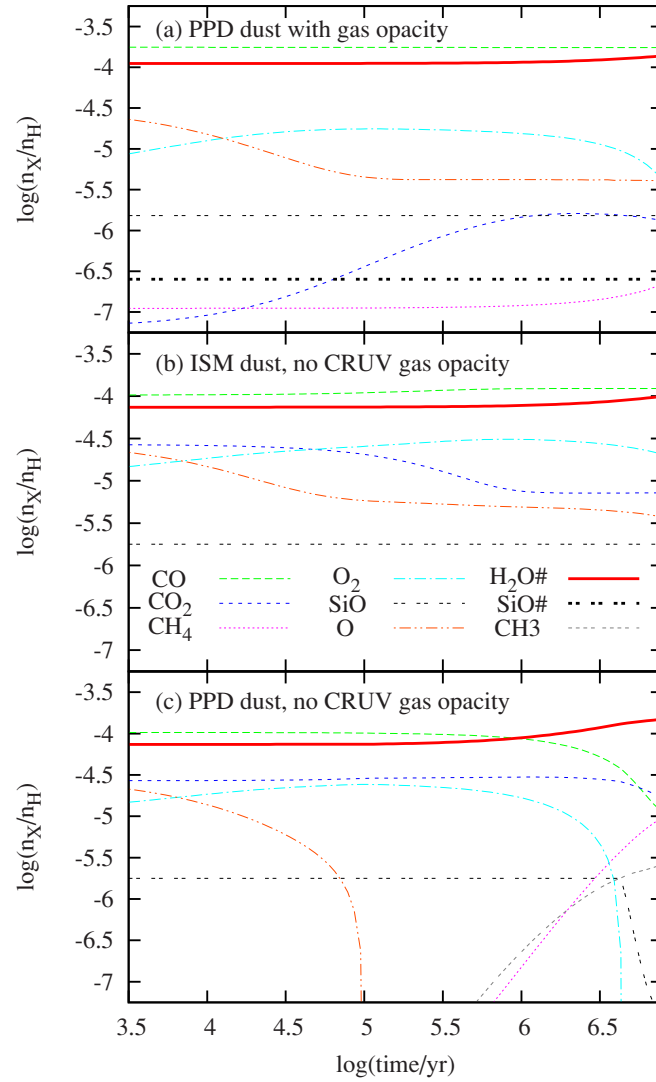


Figure 3.2: Chemical abundance evolution at a distance of 1 AU from the central star: (a) Using an ISM dust value for $\sigma_{(H)}^{UV}$ and ignoring CRUV gas opacity, (b) using an appropriate $\sigma_{(H)}^{UV}$ for protoplanetary disk conditions and ignoring CRUV gas opacity, and (c) using an appropriate $\sigma_{(H)}^{UV}$ for protoplanetary disk conditions and including the effects of CRUV gas opacity.

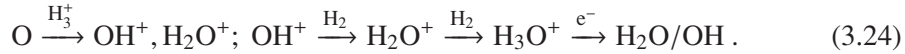
Atomic oxygen is depleted after 10^4 yr, favoring the formation of O_2 and CO_2 . Abundances of CO_2 along with OH are enhanced due to the reactions



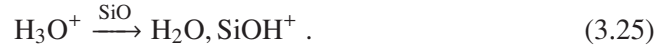
The OH enhancement is also curbed by the very efficient O_2/CO_2 formation reactions, which help keep the atomic oxygen abundance low:



Atomic oxygen is constantly generated thanks to the steady CRUV photodissociation of CO, O_2 , and CO_2 . This atomic oxygen partly goes into the formation of water vapor, which is promptly adsorbed onto the grain surface due to the temperature and density conditions at 1 AU:



This water vapor formation pathway explains the long-term ability of the system to keep forming water ice, through which it becomes the main oxygen reservoir at very long timescales. OH is recovered partly from $SiOH^+$ and also from the following H_3O^+ reaction, which can form water or OH at the same branching ratio:



Combining reactions (3.18) and (3.25) we can see how near the end, the oxygen in O_2 transfers to H_2O :



Gas-phase water created in the previous reaction freezes out almost immediately, as mentioned above (see Fig. 3.2a). In Fig. 3.3 we can see that after 10^4 yr the gas opacities reach a maximum of about 40% with respect to the dust opacity, which remains constant⁴. The late O_2 enhancement (Fig. 3.2a) implies that it is providing most of the CRUV gas extinction, and consequently SiO absorbs fewer CRUV photons. Thus O_2 slows down atomic oxygen formation via photodissociation of SiO, which is a more efficient formation mechanism than the CRUV photodissociation of O_2 . This causes a rebound effect after 10^5 yr, as O_2 needs a constant supply of atomic oxygen to form. Because OH is free to react with CO (instead of reacting with O), CO_2 formation is enhanced. However, CRUV photodissociated atomic oxygen from SiO and CO is necessary to sustain CO_2 production via reaction (3.21). This causes CO_2 to reach a saturation level near the end of the simulation.

⁴For simplicity, we did not include self-consistent grain growth models here.

3. Chemistry in gas-rich environments

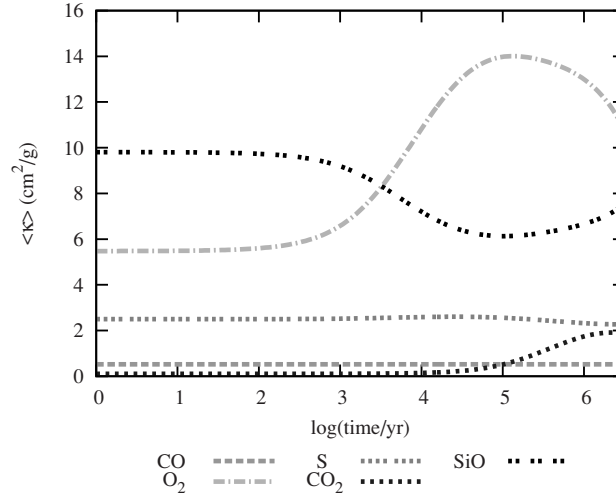


Figure 3.3: CRUV gas opacity vs. time at 1 AU. For reference, the dust opacity is $68 \text{ cm}^2/\text{g}$ (gas).

Table 3.6: Ratios between various species abundances and CO at 1 AU after 10^6 yr for three cases: Including the effects of gas opacity, considering only dust extinction from ISM dust parameters, and considering only dust extinction from protoplanetary disk dust parameters.

Ratio	With gas	No gas opacity	
	opacity, $\sigma_{\text{dust}}^{\text{PPD}}$ yr	$\sigma_{\text{dust}}^{\text{ISM}}$	$\sigma_{\text{dust}}^{\text{PPD}}$
$\text{H}_2\text{O}\#/\text{CO}$	0.69	1	0.66
O_2/CO	0.09	0.19	0.28
CO_2/CO	0.01	0.33	0.07
CH_4/CO	7×10^{-4}	2×10^{-3}	10^{-5}

Comparison to our previous work

To understand the effects of gas opacity, we also ran the simulation considering dust as the only sink for CRUV photons. We used the simplified formula for CRUV photoprocess rates from Chapter 2 (Chaparro Molano & Kamp 2012a), where the total extinction cross section is simply the grain extinction cross section. Since this calculation is not dependent on the gas phase abundances, the rate coefficients are constant throughout the simulation.

When considering a UV extinction cross section based on a protoplanetary disk dust size distribution, the CRUV photon flux is higher than for ISM dust parameters (Chaparro Molano & Kamp 2012a, Chapter 2). This is because dust coagulation processes in protoplanetary disks increase the average size of dust grains, which in turn decreases the effective area for dust absorption of UV photons. For protoplanetary disk conditions the UV extinction cross section $\sigma_{\langle H \rangle}^{\text{UV}}$ is 13.5 times lower than the typical ISM value, $\sigma_{\langle H \rangle}^{\text{UV}} = 2 \times 10^{-21} \text{ cm}^{-1}$.

Fig. 3.2b shows the time-dependent evolution of the chemical abundances for the ISM-like dust parameters used adopted for the calculation of CRUV rates in UMIST. Here, the main carriers of carbon are CO and CO₂, followed by the slightly less abundant CH₄ and CH₃. After a few 10⁵ years the carbon is almost equally divided among CH₄, CO, and CO₂. SiO is the second most important gas phase oxygen carrier up to a few Myr, when it stops to form. This is because the grains are cool enough to hold a large amount of water ice on their surface, effectively stopping OH formation and the SiO formation pathway (3.18). As the oxygen in CO, CO₂, and SiO is transferred to water ice near the end of the disk lifetime, carbon binds with H₃⁺ and H₂, which enhances the formation rates of molecules such as CH₃ and CH₄.

When comparing the chemical evolution obtained when using ISM dust parameters (Fig. 3.2b) vs. appropriate protoplanetary disk dust parameters (Fig. 3.2c), the impact of the larger CRUV flux on the abundance of various species is evidenced. As mentioned above, CRUV photodissociation processes are up to 13.5 times more efficient in protoplanetary disks than when estimated using the interstellar UV extinction cross section value used in UMIST (Chaparro Molano & Kamp 2012a, Chapter 2). Because the effects of gas extinction are neglected, the CRUV flux is enhanced uniformly for all species. This affects specifically the long-term formation of SiO, O₂, and hydrocarbons. For instance, CH₃ and CH₄ are not efficiently formed because they are very sensitive to CRUV photoprocesses. CH₄ photodissociates into CH₂, and CH₃ photodissociates into CH, CH₂ and CH₃⁺. If the CRUV field is strong enough,

3. Chemistry in gas-rich environments

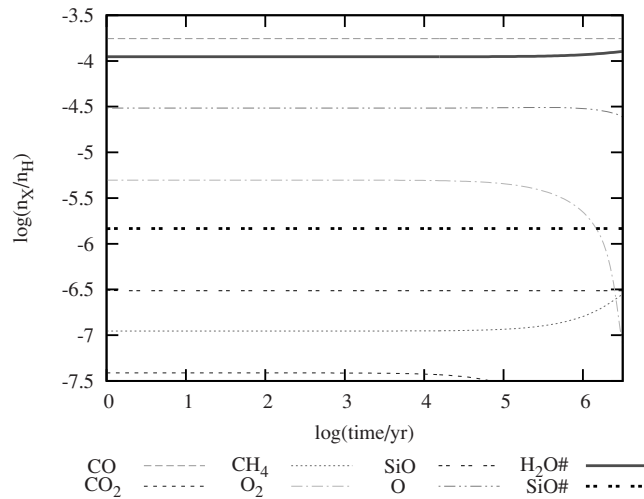


Figure 3.4: Chemical abundance evolution at a distance of 3-5 AU from the central star.

CH₃ and CH₄ will be destroyed at the expense of CO on a timescale similar to their formation timescale.

The CRUV photodissociation of CO, SiO, and CO₂ is very efficient for high CRUV fluxes. These photoprocesses steadily produce atomic oxygen at a higher rate than when considering the effects of gas opacity. This efficient formation of atomic oxygen forms OH from HCO in reaction (3.21) and preserves the OH, SiO cycle in reaction (3.18). This means that SiO is never depleted even at extremely long timescales (below 10⁸ yr). Even though CO₂ is also created from OH at the expense of CO, it never reaches a high abundance because it is destroyed via CRUV photodissociation, which ensures that the CO₂ abundances stay low compared to those seen in Fig. 3.2a.

Most notably, the CO₂/CO, O₂/CO, and CO/CH_{3,4} ratios change enormously between the three cases, as shown in Table 3.6. This shows that the chemical evolution obtained when considering the effects of gas opacity cannot be obtained by a simple interpolation between a low and a high CRUV field, but it has to be studied for each species separately.

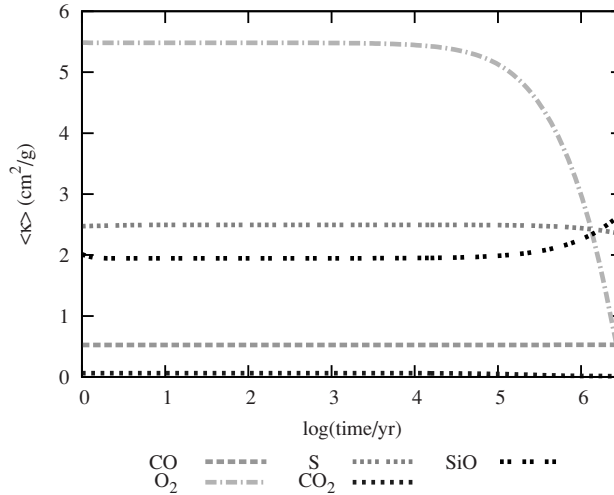


Figure 3.5: CRUV gas opacity vs. time at a distance of 3-5 AU. For reference, the dust opacity is $68 \text{ cm}^2/\text{g}$ (gas).

3.6.2 Chemistry at 3-5 AU

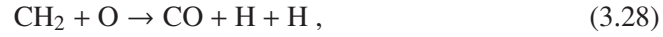
Figure 3.4 shows the chemical evolution in a region located at 3-5 AU from the central star, where $n_{\text{H}}=10^{12} \text{ cm}^{-3}$ and $T=65 \text{ K}$ (Woitke et al. 2009). In this region, reactions (3.17), (3.19), (3.26), and (3.24) still take place. However, as the temperature here is lower than at 1 AU, SiO is now mostly in the ice phase, and retains a small gas phase abundance. It is kept at a stable but low level throughout the simulation by the following feedback reaction, similar to reaction (3.18):



Therefore, OH formation is not as efficient as it was at 1 AU. The low OH formation rate cannot sustain the formation of O_2 in reaction (3.22) when it is forming H_2O , and the oxygen in O_2 transfers to H_2O via reaction 3.26. As the O_2 abundance starts to decrease, the backwards reaction (3.20) is stopped, which allows CO to form CH_4 more efficiently via reaction 3.19 (see Fig. 3.4). The consequent decrease in O_2 opacity seen in Fig. 3.5 causes the CRUV photorates to increase for other molecules, as it allows more CRUV photons to dissociate or ionize other species. This is shown in Fig 3.5, where the SiO opacity increases as the O_2 opacity decreases. Now CH_4 CRUV photodissociation becomes very efficient at forming CH_2 , which causes the

3. Chemistry in gas-rich environments

following reaction



to be favored over reaction (3.22). This exacerbates the depletion of O_2 , as seen at the end of the simulation in Fig. 3.4. The gas opacity in this region (Fig. 3.5) is less than half the value at 1 AU (Fig. 3.3, note the different vertical scale), which is caused by the lack of efficient O_2 formation and the freeze-out of SiO. The first part of reaction (3.21) is reversed by the following reaction:



which keeps the CO_2 levels low. This is enabled by an increase in effectivity of electron recombination reactions vs. neutral reactions brought about by the low-density conditions, compared to the 1 AU region.

3.6.3 Chemistry at 7-8 AU

In this region, the physical conditions are $n_{\langle\text{H}\rangle} = 10^{11} \text{ cm}^{-3}$ and $T = 50 \text{ K}$ (Woitke et al. 2009). As we can see from the chemical evolution plot in Fig. 3.6, H_2O and SiO are completely frozen after only 1 yr, with negligible gas phase abundances. However, the chemical evolution for the other significant species remains more or less the same. The lack of SiO in the gas phase impacts the late formation of H_2O that appears at 1-5 AU. Since O_2 is not consumed via reaction (3.26, its depletion is not as dramatic as in the 3-5 AU region. Now the main reaction that removes O_2 from the gas is



This reaction, which does not have an activation energy barrier and is very rapid at very low temperatures (Smith et al. 2004), allows reaction (3.19) to form CH_4 very late in the simulation in the same way that we observed for the previous region (3-5 AU). Reactions (3.17,3.22,3.24) are also responsible for the formation of CO, O_2 , and H_2O , respectively. Just as in the 3-5 AU region, CO_2 is not efficiently formed because its formation via reaction (3.21) is stopped by the backreaction (3.29). The gas opacity here (Fig. 3.7) is very similar to that observed at 3-5 AU (Fig. 3.5). The absence of SiO opacity due to freeze-out enhances the CRUV rates for all other species, including CO.

3.7 Discussion

We have included the gas opacity of all atoms and molecules that are photoprocessed by cosmic-ray-induced UV photons in our chemical evolution model. By doing this,

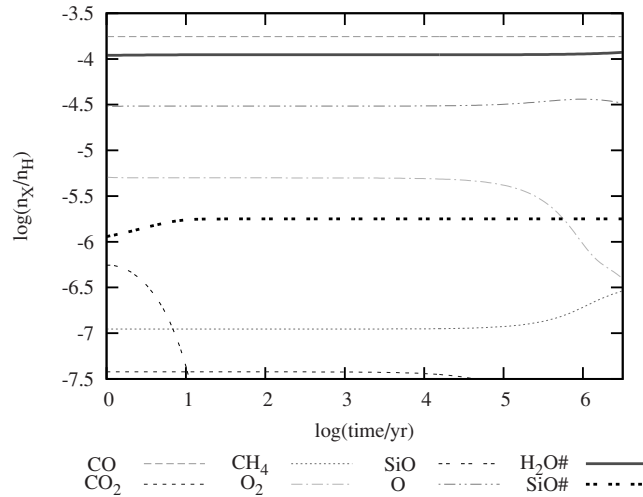


Figure 3.6: Chemical abundance evolution at a distance of 7-8 AU from the central star.

we were able to assess whether a given species is relevant for the extinction of CRUV in the midplane of a protoplanetary disks. By studying the impact that the gas opacity of individual species has on the chemistry and vice versa, we can simplify the chemical model by including only the most important species. As some opacities increase, an important shielding effect appears and changes the CRUV photoprocess rates. This affects the chemical formation pathways for both gas- and ice-phase species.

As discussed in Section 3.5, the most important species that contribute to the gas opacity are O_2 , SiO , S , CO , and CO_2 consistently throughout the 1-10 AU region of the disk midplane. We found that the opacities of O_2 , SiO (and CO_2 in the warm regions around 1 AU) are the most variable in time and hence are the ones that require most attention. As the CO abundance remains more or less constant in those regions, its opacity remains fairly constant as well. Even though we did not include sulphur chemistry beyond ionization, its CRUV opacity ranges from 2.5 to 3.5 cm^2/g gas (see Figs. 3.3, 3.5, 3.7 and 3.8), reaching its highest contribution with respect to the total gas opacity (70%) and with respect to the total dust and gas opacity (3.4%) at 10-15 AU.

When comparing the gas opacity to the total CRUV opacity in Table 3.7, it is evident that its effect cannot be easily dismissed. In the region 1-2 AU the contribution from the gas is up to 30% of the combined gas and dust opacity. At 7-8 AU,

3. Chemistry in gas-rich environments

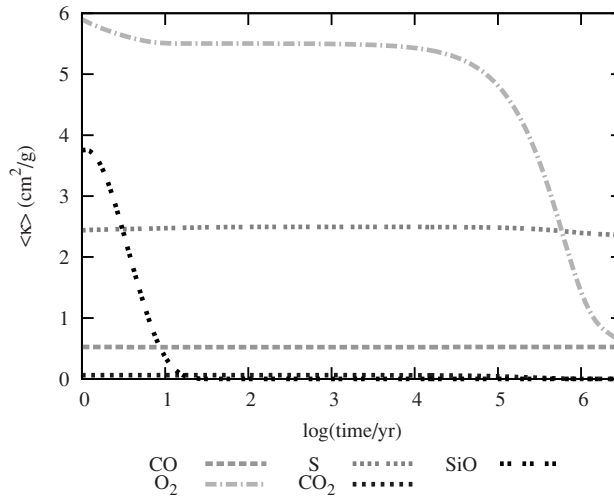


Figure 3.7: CRUV gas opacity vs. time at a distance of 7-8 AU. For reference, the dust opacity is $68 \text{ cm}^2/\text{g}$ (gas).

the contribution is up to 10%, mostly because of SiO freeze-out. Finally, at 10 AU the temperature becomes sufficiently low to freeze CO, CO₂ and CH₄ onto the grain surface, and the contribution of the gas opacity becomes very low (5%). Therefore, future chemical models that aim to include this treatment of CRUV gas and dust opacity can consider the contribution of the most significant species that our models yield for the probed regions of the disk.

The general chemical composition of the disk midplane obtained using our models compare favorably to that in Walsh et al. (2010), particularly in the freeze-out of water at distances above 1 AU, and in the significant gas phase presence of CO (and CO₂ to a lesser degree) throughout the studied region. We notice the same low abundances of H₂CO and OH. These similarities are caused by the temperature structure, which controls the adsorption and desorption processes.

3.7.1 The role of OH

The availability of OH caused by the high and steady abundance of SiO at 1 AU causes a late O and O₂ enhancement. The products of SiO dissociation later form H₃O⁺, which via dissociative recombinations (Si, e⁻) forms water vapor. Atomic oxygen is very abundant at 1 AU thanks to cosmic-ray-induced dissociation of CO

Table 3.7: Total gas opacity as a function of time and distance. Percentage relative to the total dust ($68 \text{ cm}^2/\text{g gas}$) and gas opacity is given in parentheses.

Distance	Total gas opacity $\langle \kappa_{\text{gas}} \rangle$ ($\text{cm}^2/\text{g gas}$)		
	10^4 yr	10^5 yr	10^6 yr
1 AU	23.6 (25.8%)	25.4 (27.2%)	26.7 (28.2%)
3-5 AU	11.5 (14.5%)	11.1 (14%)	9.2 (12%)
7-8 AU	9.5 (12.3%)	9 (11.7%)	5.4 (7.4%)
10-15 AU	3.6 (5%)	3.7 (5.2%)	4.2 (5.8%)

and SiO. However, oxygen-driven OH formation acts as a catalyst for steady CO formation. A rebound effect is observed at a late stage (10^5 yr), as O_2 self-shields the CRUV photons that drive the OH driven pathways for its formation.

Even though SiO is formed in reaction (3.18) at 3-5 AU, under these conditions it is very efficiently adsorbed onto the grain surface. This affects the formation of OH and thus O_2 is depleted at long timescales, favoring CO formation via CH_4 and later CH_2 reactions with O. As the gas phase SiO is depleted, no O_2 is transformed into H_2O , which avoids the complete depletion of O_2 . At 7-8 AU there is an overall enhancement of CRUV rates because of this. After 10 AU, the total gas opacity is sufficiently low for OH to drive the chemistry. Indeed, Fig. 3.8 shows the gas opacity at 10 AU, in which OH is seen to contribute. This agrees with the results from Chapter 2 (Chaparro Molano & Kamp 2012a).

3.7.2 Survival of SiO in the $A_V = 1$ region

The longevity of SiO in our models of the disk midplane (see Figs. 3.2a and 3.4) could have potential consequences beyond the midplane of the disk. We explored the chemistry at 1 AU in a direction perpendicular to the disk plane upwards to densities of $n_{\langle \text{H} \rangle} = 10^{11} \text{ cm}^{-3}$. We saw that the abundance of SiO remains steadily high, meaning that SiO can be formed even above the midplane.

Following Aikawa (2007), the vertical drift timescale τ_{vd} of a molecule formed in the midplane of the disk that moves up to a distance $z = \lambda$ above the midplane can be

3. Chemistry in gas-rich environments

estimated via the disk viscosity⁵ ν (Shakura & Sunyaev 1973):

$$\tau_{\text{vd}} = \frac{\lambda^2}{\nu}. \quad (3.31)$$

A simple calculation for $\lambda = 0.1$ AU, corresponding to the $A_V = 1$ region (at $r = 1$ AU) of the disk, yields

$$\tau_{\text{vd}} \simeq 280 \text{ yr}. \quad (3.32)$$

If the SiO photodissociation timescale at $A_V = 1$ is longer than the vertical drift timescale, it should be possible for SiO to accumulate on the surface where it could be observed. We can roughly estimate this timescale, which depends on the strength of the local UV field χ . Using the detailed radiative transfer model of Woitke et al. (2009), we derive a value for χ in the range 1-10 at the $A_V = 1$ line. Accordingly, an SiO molecule can survive for approximately 10^3 yr if $\chi = 1$. This means that it may be possible for SiO to accumulate around $A_V = 1$ and be detectable. For example, SiO masers are detected in the circumstellar regions around asymptotic giant branch (AGB) stars, and their maser lines are found to originate from regions below the dust evaporation radius (Habing 1996). More recently, gas phase SiO has been detected in the debris disk around η Corvi (Lisse et al. 2012). Hence it should be possible to detect accumulated SiO even if there are dust grains present. Our low ISM metal abundances already take Si incorporation into dust grains into account. Given that the region where SiO is being formed has a small radial extent ($r \leq 1 - 5$ AU), detection of SiO could prove to be very difficult in the near future, except for high-sensitivity, high-spatial-resolution observations that ALMA could carry out.

3.8 Conclusions

We have developed a tool for including the effects of gas extinction of cosmic-ray-induced UV photons in the chemical evolution in the disk midplane. The most important species that contribute to the gas opacity in the 1-8 AU region of the disk midplane are O_2 , SiO, S, CO, and CO_2 . Because the CO abundance is steady in those regions, its opacity remains fairly constant as well. Even though CO competes with water ice for being the most abundant species, CO is not a major contributor to the opacity, whereas CO_2 play a more important role in the opacity while not being as chemically abundant as CO.

⁵The value of $\nu = \alpha c_s h$ depends on the sound speed c_s , the scale height h of the disk and the Shakura Sunyaev α parameter, for which we chose a value of 0.1 corresponding to a young disk with $\dot{M} \simeq 10^{-8} M_\odot/\text{yr}$. This mass accretion rate value suggests an age for the disk in the range $10^{5.5}$ - $10^{6.5}$ yr, according to Hartmann et al. (1998).

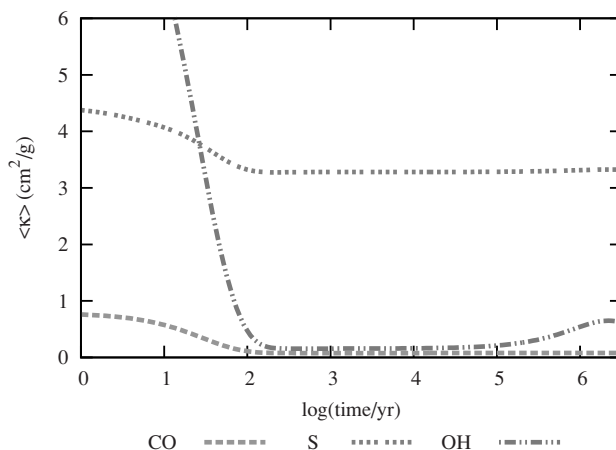


Figure 3.8: CRUV gas opacity vs. time at a distance of 10 AU. For reference, the dust opacity is $68 \text{ cm}^2/\text{g}$ gas).

We find that the opacities of O_2 , SiO (and CO_2 in the warm regions around 1 AU) are highly variable in time, and their effects on the gas and ice chemistry cannot be easily dismissed. Therefore, future models should include the gas opacity of these species in the calculation of CRUV photoprocess rates.

As most of the emission in recent IR observations of OH and H_2O in disks (Carr & Najita 2008; Najita et al. 2010; Fedele et al. 2011; Meeus et al. 2012) is likely coming from layers well above the midplane, the catalytic role of OH in the midplane is not necessarily something we can prove by observing its surface abundance.

Finally, we found that if SiO is steadily created in the midplane at long timescales, it can drift vertically upwards and accumulate around the $A_V = 1$ region, which suggests a possibility for future detections of SiO in protoplanetary disks.

Acknowledgments We would like to thank Malcolm Walmsley for asking the basic question that triggered this research.

Appendix: Cross-section data

Table 3.8 presents the information on all CRUV photoprocesses considered here, based on the UMIST06 reaction database (Woodall et al. 2007). Column 2 lists whether the photoprocess ionizes or dissociates the species. Column 3 shows the products of the reaction. Column 4 references the source for the photoprocess cross section, which for most of them is Ewine van Dishoeck's Leiden photoprocess database <http://www.strw.leidenuniv.nl/~ewine/photo/> (van Dishoeck et al. 2006). Column 5 refers to whether the photoprocess is a discrete and/or continuum absorption process.

Table 3.8: Cosmic ray-induced UV photoprocess list.

Species	Proc.	Products	Source	Type
C	Ion.	C ⁺ +e ⁻	Leiden	Cont.
CH	Dis.	C+H	Leiden	Line/Cont.
CH ⁺	Dis.	C ⁺ +H	Leiden	Line/Cont.
CH ₂	Ion.	CH ₂ ⁺ +e ⁻	UMIST06 (Gredel et al. 1989)	Cont.
CH ₂	Dis.	CH+H	Leiden	Line/Cont.
CH ₃	Ion.	CH ₃ ⁺ +e ⁻	UMIST06 (No ref. data)	Cont.
CH ₃	Dis.	CH ₂ +H	Leiden	Line
CH ₃	Dis.	CH+H ₂	Leiden	Line
CH ₄	Dis.	CH ₂ +H ₂	Leiden	Line/Cont.
OH	Dis.	O+H	Leiden	Line/Cont.
H ₂ O	Dis.	OH+H	Leiden	Cont.
Mg	Ion.	Mg ⁺ +e ⁻	Leiden	Line/Cont.
CO	Dis.	C+O	Leiden	Line
Si	Ion.	Si ⁺ +e ⁻	Leiden	Cont.
HCO	Dis.	CO+H	Leiden	Line
HCO	Ion.	HCO ⁺ +e ⁻	UMIST06 (Gredel et al. 1989)	Cont.
SiH	Dis.	Si+H	Leiden	Line
H ₂ CO	Dis.	CO+H ₂	Leiden	Line/Cont.
O ₂	Dis.	O+O	Leiden	Line/Cont.
O ₂	Ion.	O ₂ ⁺ +e ⁻	Leiden	Line
S	Ion.	S ⁺ +e ⁻	Leiden	Cont.
CO ₂	Dis.	CO+O	Leiden	Line/Cont.
SiO	Dis.	Si+O	Leiden	Line
Fe	Ion.	Fe ⁺ +e ⁻	Leiden	Cont.



4 Chemical evolution of the cosmic-ray dominated midplane of protoplanetary disks

—G. Chaparro Molano, I. Kamp, W.-F. Thi & P. Woitke—

In preparation

*Time weighs down on you like an old, ambiguous dream.
You keep on moving, trying to sleep through it.
But even if you go to the ends of the earth,
you won't be able to escape it.
Still, you have to go there- to the edge of the world.
There's something you can't do unless you get there.
— Haruki Murakami, *Kafka on the Shore* —*

Abstract

Context. The formation of ices on the surface of dust grains allow a comparison between the composition of the midplane of disks and the composition of ices in Solar System bodies.

Aims. We analyze the history of formation of icy species on the surface of grains, focusing on the effects of cosmic ray-induced processes in the disk midplane. Cosmic ray-induced UV photons have a similar effect on the overall chemistry as stellar or interstellar UV radiation, via photoionization and photodissociation of gas species and photodesorption of ice species.

Methods. We implement a new way of calculating cosmic ray-induced photo-process rates in a 2D, time-dependent chemical model of the early solar nebula, focusing on the disk midplane. The calculation of these rates is consistent with the local gas and dust extinction properties. We apply this to a fully converged model of the Early Solar Nebula obtained with the thermo-chemical disk modeling code ProDiMo.

Results. We find that the gas opacity in the gas-rich regions of the disk midplane is dominated by CO₂. We also find that the midplane abundance of ice species such as CO#, CO₂#, CH₄#, Si#, and H₂CO# is underpredicted in steady state models, and they may in fact form in the early stages of the disk evolution. Because of ice layering, species formed at timescales smaller than the lifetime of the disk can be preserved in the bottom layers of the ice mantle of dust grains.

4.1 Introduction

The midplane of protoplanetary disks is the most likely place where planets are born (Johansen et al. 2007), and their composition will depend crucially on the chemical conditions in which they are formed. In our own solar system, comets and meteorites are remainders from that epoch. Other protoplanetary disks are themselves going through the chemical evolution that sets the local conditions in the regions where exoplanets are born.

Most models agree that the midplane of protoplanetary disks at distances below a few AU is not significantly ionized from stellar or interstellar radiation (Gammie 1996). In such an environment chemical processes will be very slow, and mostly neutral-neutral reactions will take place. However, cosmic rays are among the few sources of ionization that can theoretically penetrate such regions and drive the chemistry there¹. Thus, wherever stellar UV radiation cannot penetrate, cosmic rays become the dominant source of ionization in the midplane of the disk. This characterizes the disk midplane (outside of the $r \simeq 1$ AU region) as a cosmic-ray dominated region.

Grain size distributions in protoplanetary disk models consider larger grains than in molecular cloud models because of grain growth, which observations (D'Alessio et al. 2001) and analyses of chondrules in the solar nebula (Ormel et al. 2008) seem to support. An increase in the average grain size will decrease the surface area per unit volume, which means that grains will become less efficient in absorbing UV photons, especially locally generated cosmic ray-induced UV (CRUV) photons (Chaparro Molano & Kamp 2012a, Chapter 2). Grain growth can cause an enhancement of a factor 40 in the CRUV flux in gas-poor regions of the disk (Chaparro Molano & Kamp 2012a, Chapter 2). As the temperature in the inner regions of the disk midplane range from 80-300K, most chemical species will stay in the gas phase. Therefore, local gas extinction of CRUV photons can play a significant role in the chemical evolution. A comprehensive treatment of this effect was developed in Chapter 3 (Chaparro Molano & Kamp 2012b), who show that the effect of gas opacity cannot be trivially disentangled from the CRUV-driven chemistry using a simple correction factor.

Steady-state models of the chemistry of protoplanetary disks (Woitke et al. 2009; Willacy & Woods 2009; Gorti et al. 2011; Thi et al. 2011) are limited because the

¹The maximum column density for cosmic ray penetration was found to be $\Sigma \sim 150 \text{ g cm}^{-2}$ by Umebayashi & Nakano (1981). A brief discussion of the effects of magnetic fields in cosmic ray deflection Padovani & Galli (2011) can be found in Chapter 3 (Chaparro Molano & Kamp 2012b).

4. The cosmic-ray dominated region of disks

timescale for reaching steady state in the midplane of disks can be longer than the disk lifetime (Woitke et al. 2009), which is of a few 10^6 yr (Hernández et al. 2008; Fedele et al. 2010; Haisch et al. 2010; Semenov & Wiebe 2011). Hence, the best approach is through a time-dependent analysis of the chemistry (Visser et al. 2009, 2011; Walsh et al. 2010; Semenov et al. 2010). This enables us to study the history of ice formation and the time evolution of the ice composition, which can be compared to that of cometary bodies (Chaparro Molano & Kamp 2012a, Chapter 2).

In order to obtain a chemical model of the ice formation history in the disk midplane, we implemented a self-consistent treatment of CRUV photoprocesses in ProDiMo (Woitke et al. 2009). This implementation is based on the theoretical framework developed in Chapter 2 (Chaparro Molano & Kamp 2012a) and Chapter 3 (Chaparro Molano & Kamp 2012b). In Section 2 we summarize the general principles of CRUV photoprocesses. In Section 3 we explain how we achieve a self-consistent treatment of CRUV photorates for a model of the early solar nebula. This is followed by a comparative discussion of the time evolution models obtained with and without including our CRUV implementation (Section 4). In Section 5, we summarize the main results of this Chapter.

4.2 Cosmic-ray-induced UV photoprocesses

Cosmic rays can be an important source of ionization and heating in the disk (Glassgold et al. 2007). Their main chemical by-products are H_3^+ , He^+ and ~ 30 eV electrons coming from the ionization of molecular hydrogen. The cosmic ray-ionization rate of H_2 , ζ_{H_2} is the of the order of $\zeta_{\text{H}_2} = 5 \times 10^{-17} \text{ s}^{-1}$ (Indriolo et al. 2007) in the ISM. In protoplanetary disks it is important to use an attenuation factor based on the maximum surface density for penetration of cosmic rays, $\Sigma_{\text{crit}} \simeq 150 \text{ cm}^{-2}$ (Umebayashi & Nakano 1981). This attenuation factor at a location z, r in the disk can be written as (Semenov et al. 2010):

$$\zeta_{\text{H}_2}(r) = \zeta_{\text{H}_2}^{\text{ISM}} \left[\exp(-\Sigma_{\text{top}}(z, r)/\Sigma_{\text{crit}}) + \exp(-\Sigma_{\text{bottom}}(z, r)/\Sigma_{\text{crit}}) \right]. \quad (4.1)$$

Here, the labels 'top' and 'bottom' refer to the surface density of the top and the bottom side of the disk, as cosmic rays enter from both sides. At 1 AU the surface density of a T Tauri disk is 163 g cm^{-2} , which is similar to the penetration limit quoted above. This means that at radial distances beyond 1 AU, cosmic rays can penetrate relatively unscathed.

Electrons coming from the ionization of H_2 can subsequently excite neutral H_2 , which spontaneously emit Lyman and Werner photons in the 90 – 170 nm range.

4.2 Cosmic-ray-induced UV photoprocesses

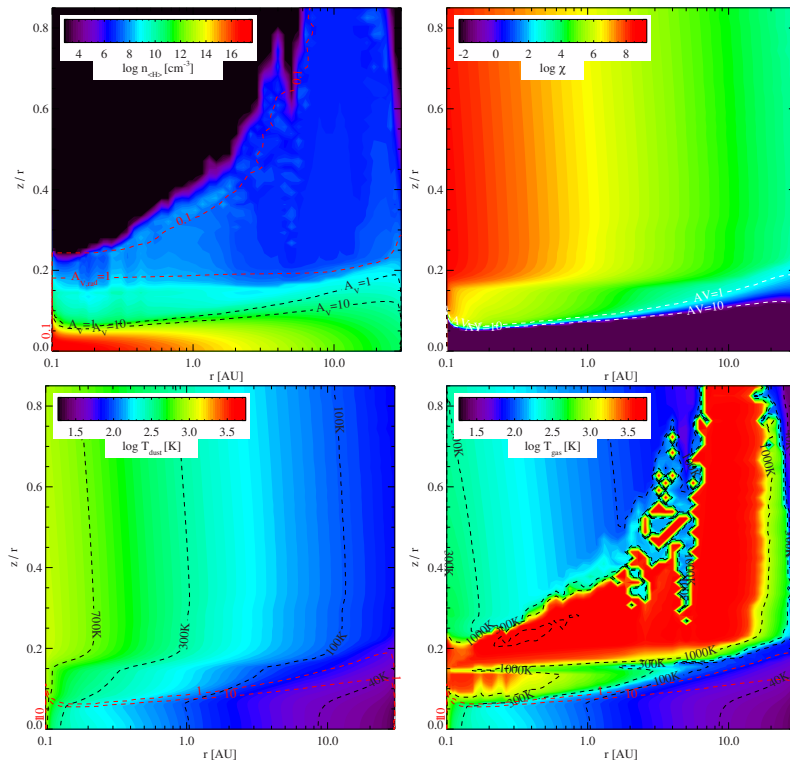


Figure 4.1: Density, UV field strength, dust temperature and gas temperature of an Early Solar Nebula model obtained using the parameters in Table 4.1.

4. The cosmic-ray dominated region of disks

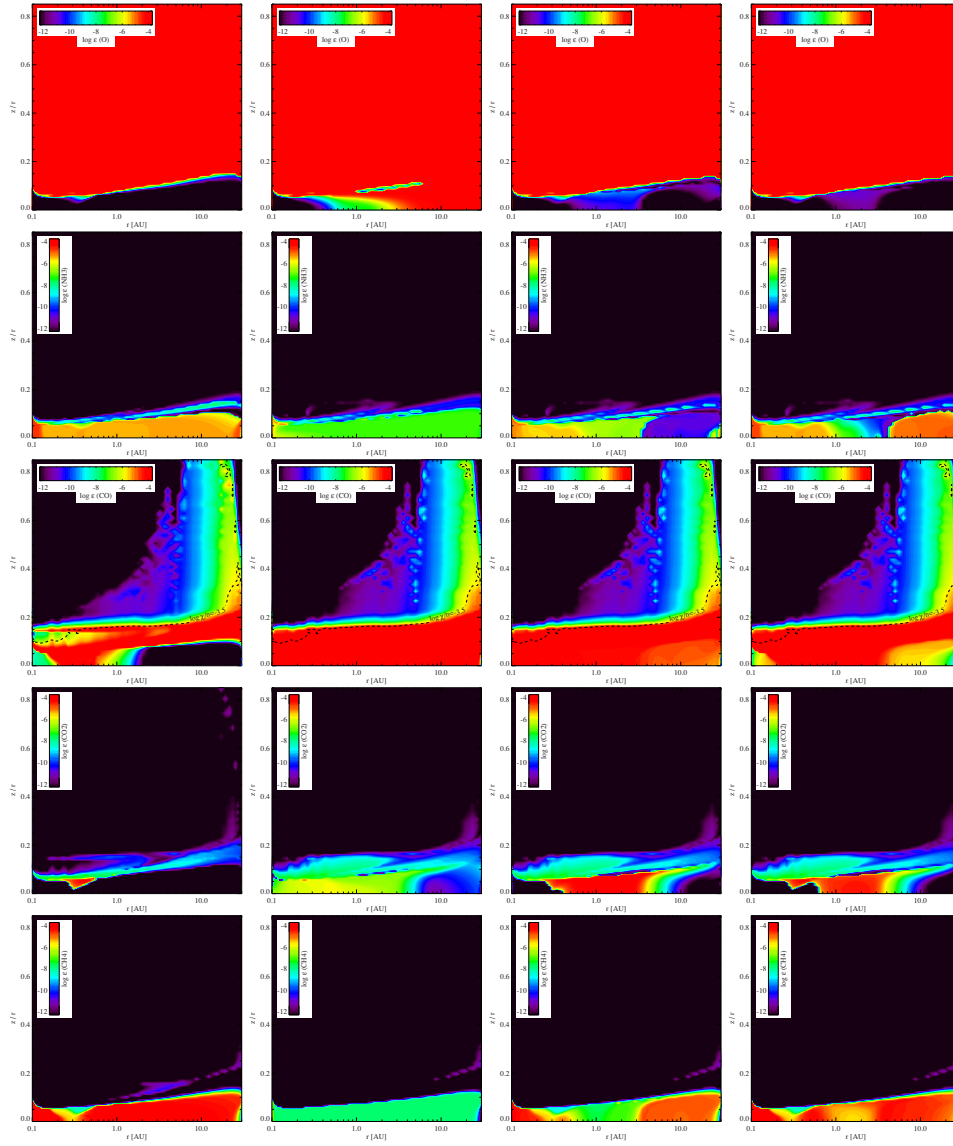


Figure 4.2: Chemical abundances of an early solar nebula model without self-consistent CRUV photoprocessing. The plots on the left (Col. 1) correspond to a steady-state solution for the chemistry (Model LS in the text), and the time evolution (Model LT in the text) plots for 10^3 , 10^6 and 10^7 yr are shown from left to right (Col. 2-4).

4.2 Cosmic-ray-induced UV photoprocesses

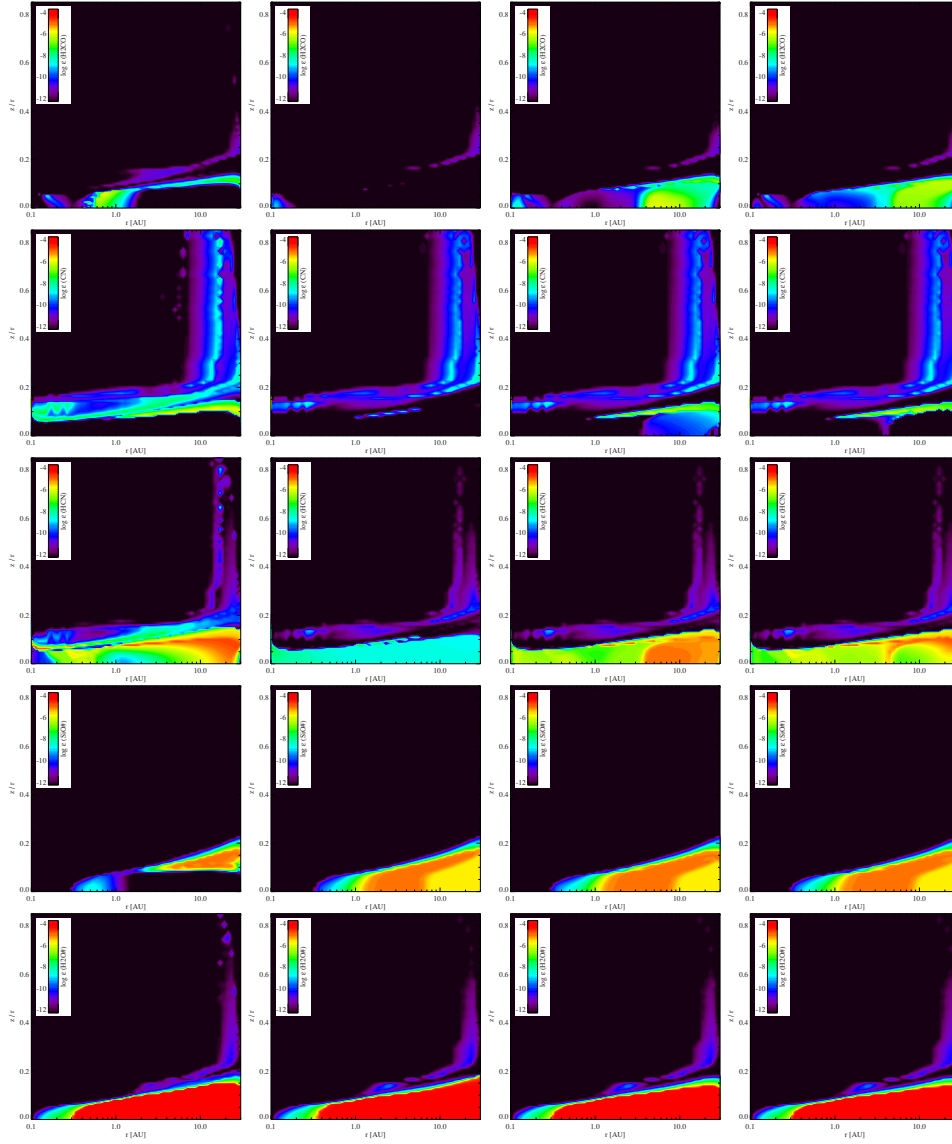


Figure 4.3: Chemical abundances of an early solar nebula model without self-consistent CRUV photoprocessing. The plots on the left (Col. 1) correspond to a steady-state solution for the chemistry (Model LS in the text), and the time evolution (Model LT in the text) plots for 10^3 , 10^6 and 10^7 yr are shown from left to right (Col. 2-4).

4. The cosmic-ray dominated region of disks

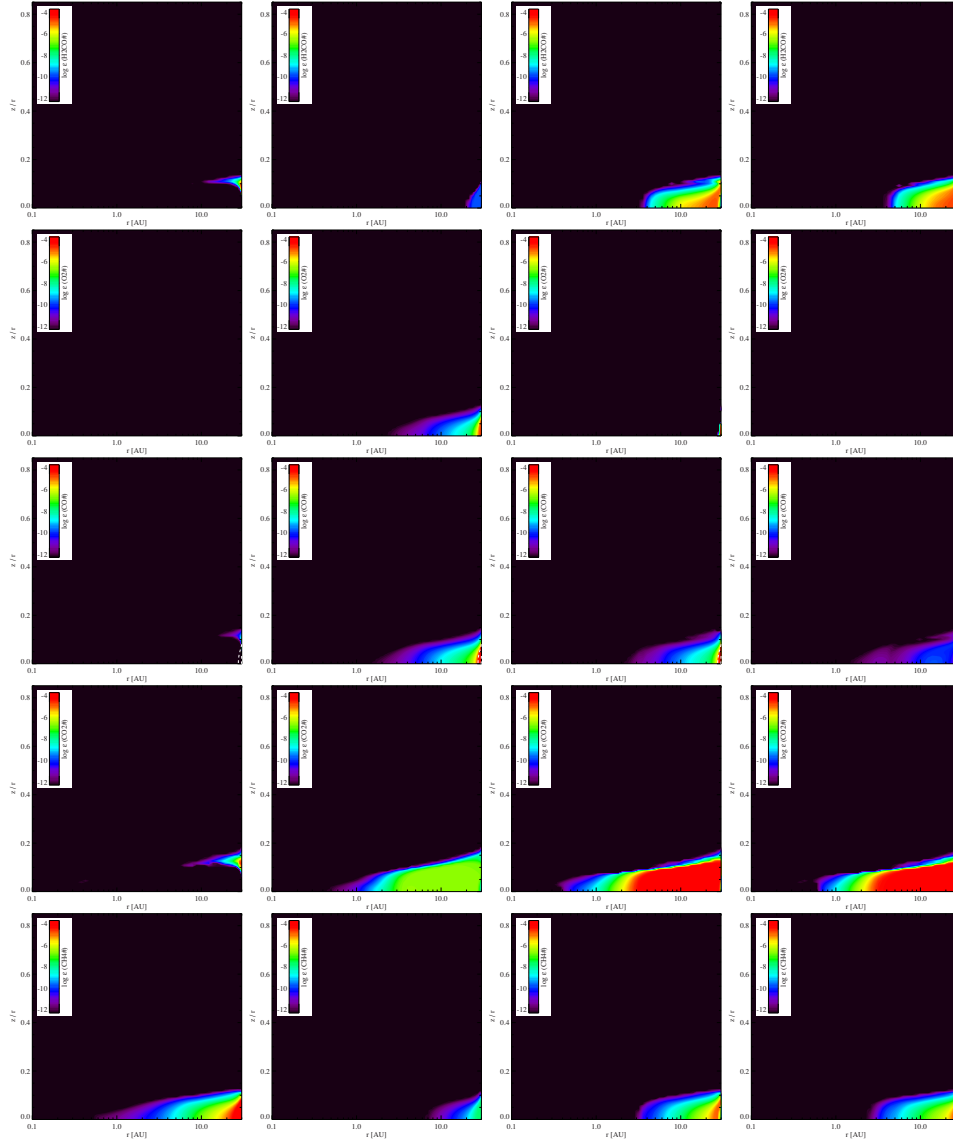


Figure 4.4: Chemical abundances of an early solar nebula model without self-consistent CRUV photoprocessing. The plots on the left (Col. 1) correspond to a steady-state solution for the chemistry (Model LS in the text), and the time evolution (Model LT in the text) plots for 10^3 , 10^6 and 10^7 yr are shown from left to right (Col. 2-4).

4.2 Cosmic-ray-induced UV photoprocesses

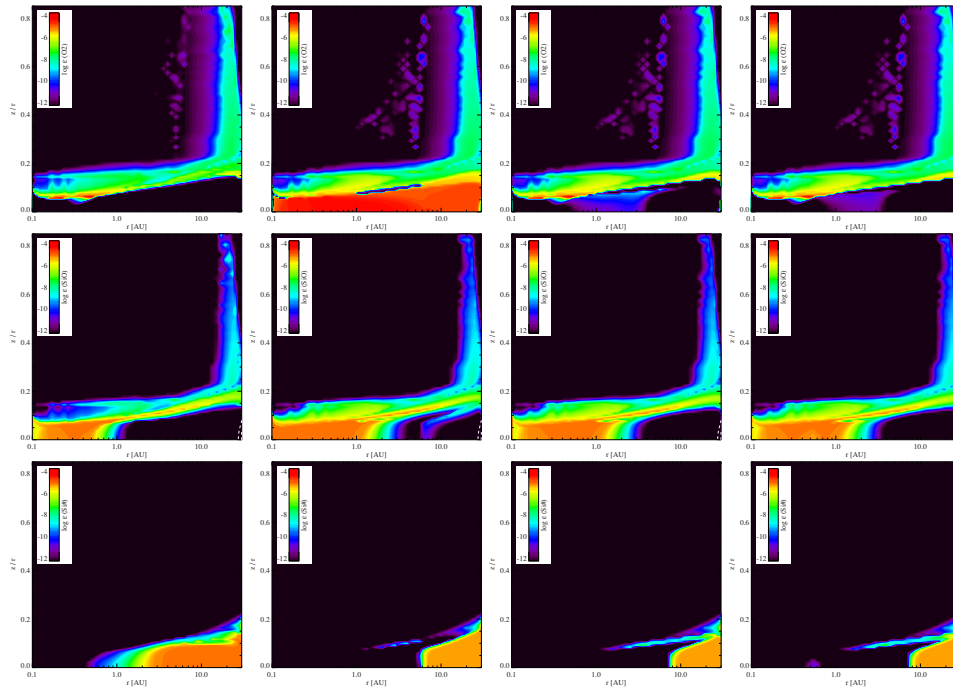


Figure 4.5: Chemical abundances of an early solar nebula model without self-consistent CRUV photoprocessing. The plots on the left (Col. 1) correspond to a steady-state solution for the chemistry (Model LS in the text), and the time evolution (Model LT in the text) plots for 10^3 , 10^6 and 10^7 yr are shown from left to right (Col. 2-4).

4. The cosmic-ray dominated region of disks

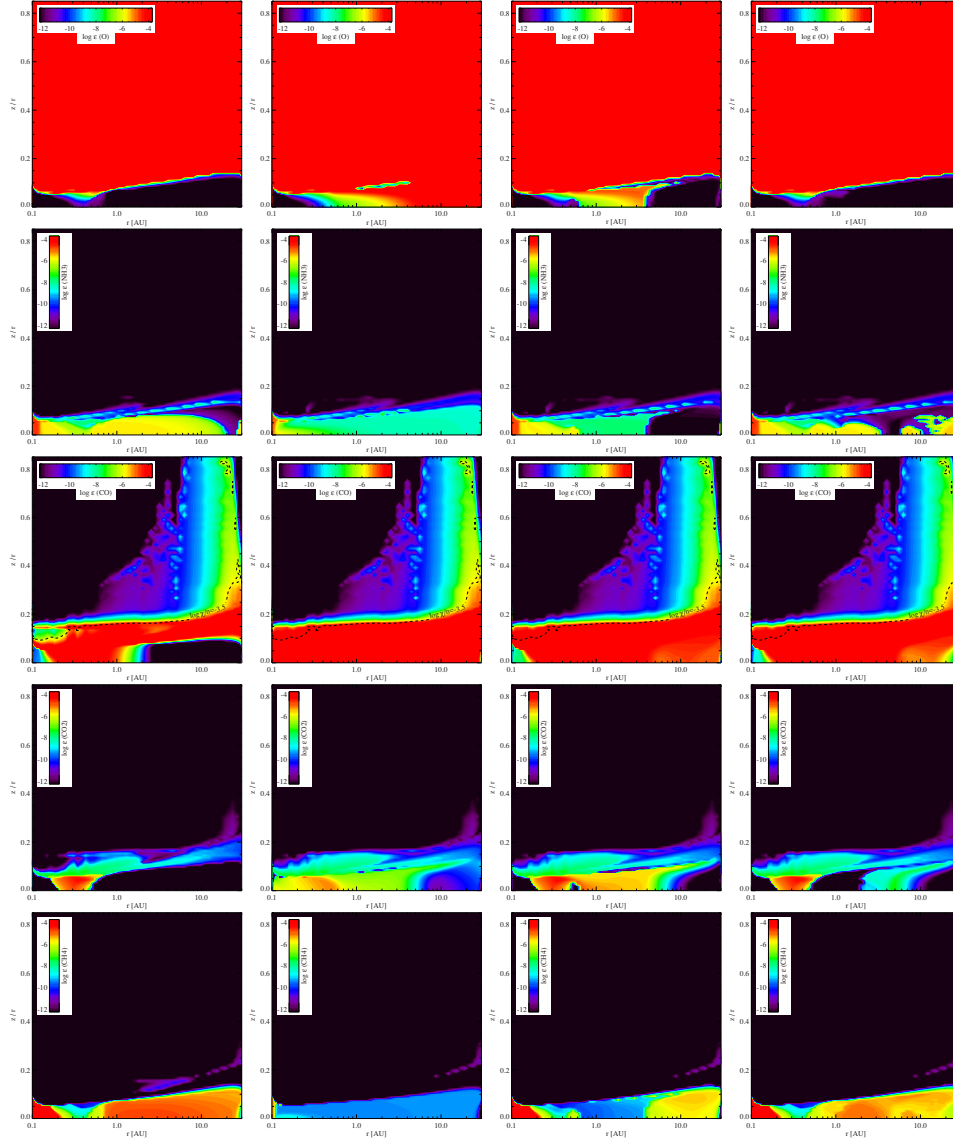


Figure 4.6: Chemical abundances of an early solar nebula model obtained using a CRUV photorate calculation that is consistent with the dust properties of the disk but neglecting the local gas extinction. The plots on the left (Col. 1) correspond to a steady-state solution for the chemistry (Model HS in the text), and the time evolution (Model HT in the text) plots for 10^3 , 10^6 and 10^7 yr are shown from left to right (Col. 2-4).

4.2 Cosmic-ray-induced UV photoprocesses

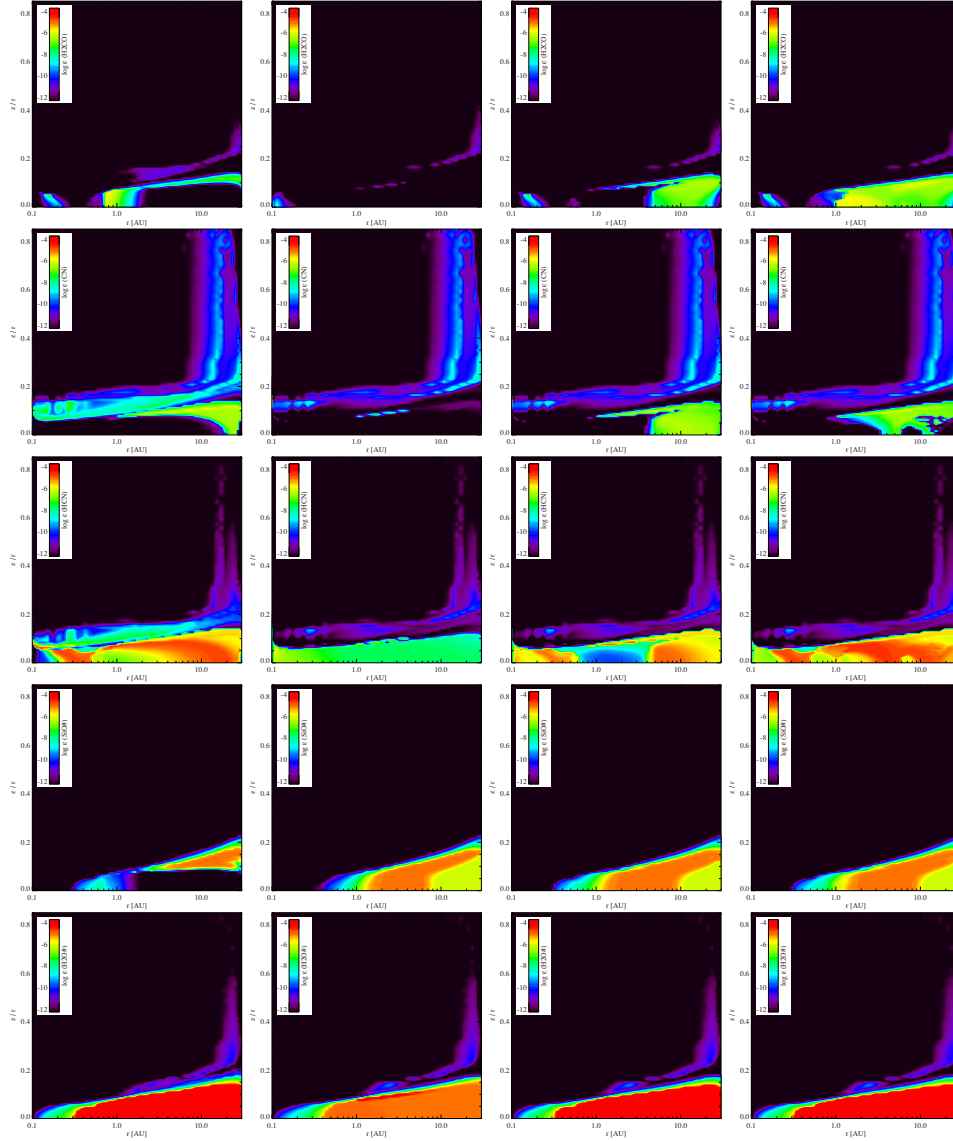


Figure 4.7: Chemical abundances of an early solar nebula model obtained using a CRUV photorate calculation that is consistent with the dust properties of the disk but neglecting the local gas extinction. The plots on the left (Col. 1) correspond to a steady-state solution for the chemistry (Model HS in the text), and the time evolution (Model HT in the text) plots for 10^3 , 10^6 and 10^7 yr are shown from left to right (Col. 2-4).

4. The cosmic-ray dominated region of disks

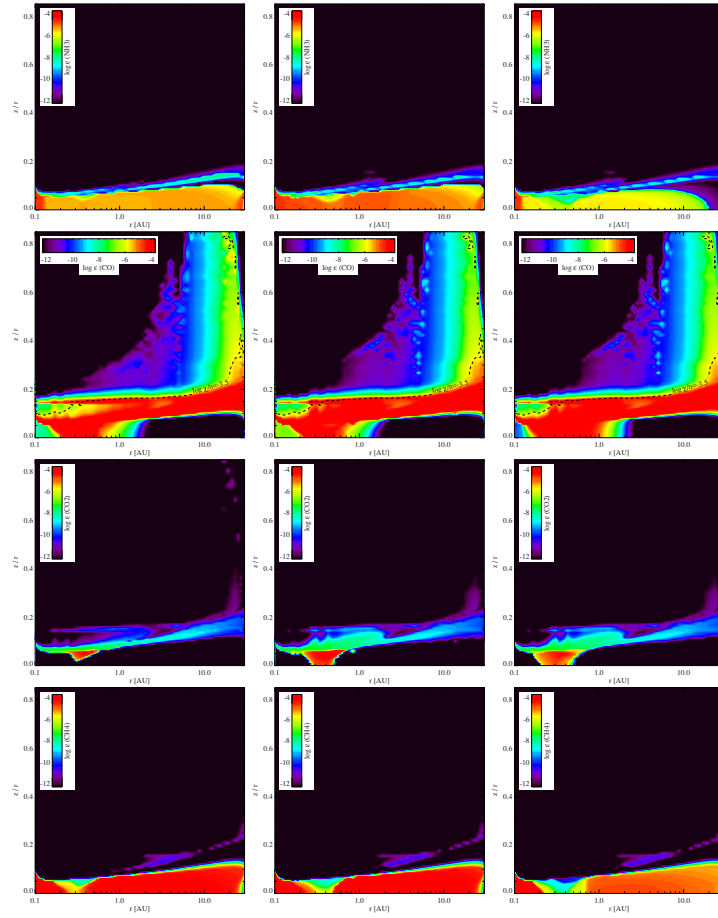


Figure 4.8: Comparison between steady-state chemical abundances obtained using model LS (left column), model SS (center column), and model HS (right column).

4.2 Cosmic-ray-induced UV photoprocesses

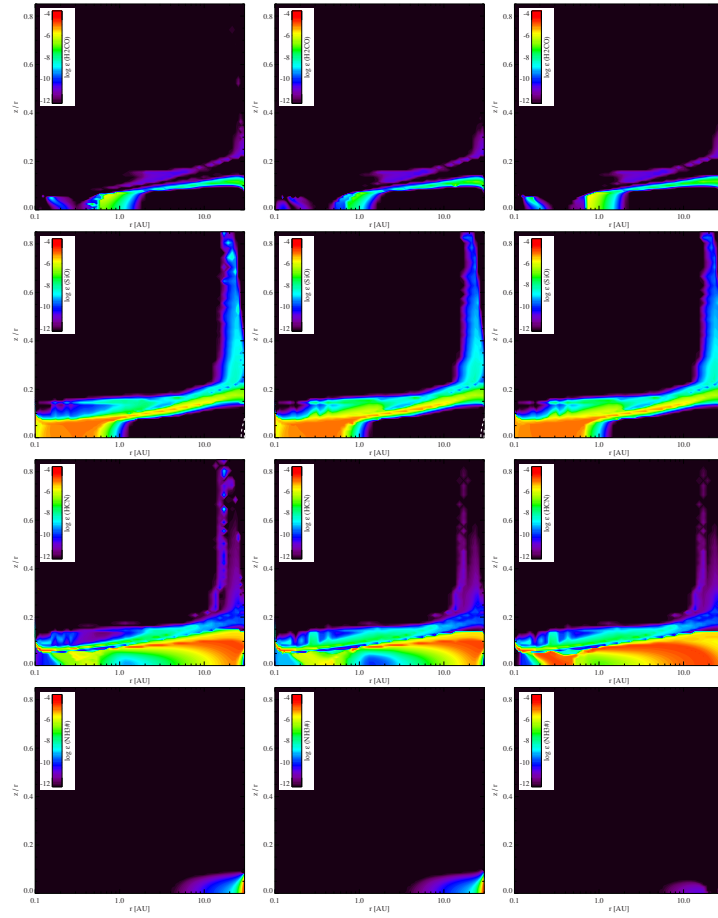


Figure 4.9: Comparison between steady-state chemical abundances obtained using model LS (left column), model SS (center column), and model HS (right column).

4. The cosmic-ray dominated region of disks

Table 4.1: Table of modeling parameters.

Parameter	Symbol	Value
Stellar mass	M_*	$1 M_\odot$
Effective temperature	T_{eff}	5770 K
Stellar luminosity	L_*	$1 L_\odot$
Disk mass	M_{D}	$0.01 M_\odot$
Inner disk radius	R_{in}	0.1 AU
Outer disk radius	R_{out}	30 AU
Dust-to-gas mass ratio	ρ_d/ρ_g	0.01
Minimum dust grain size	a_{min}	$0.1 \mu\text{m}$
Maximum dust grain size	a_{max}	$10 \mu\text{m}$
Dust material mass density	ρ_{gmd}	$2.5 \text{ g}\cdot\text{cm}^{-3}$
Gas surface density power law index	ϵ	1.5
Dust grain size power law index	p	3.5
Dust composition (Draine & Lee 1984)	-	100% Silicate
Abundance of PAHs relative to ISM	f_{PAH}	0.0001
Cosmic ray ionization rate (H_2)	ζ_{H_2}	$5 \times 10^{-17} \text{ s}^{-1}$
Number of active layers	N_{Lay}	2
Adsorption site area	A_{site}	$6.67 \times 10^{-16} \text{ cm}^2$

4.2 Cosmic-ray-induced UV photoprocesses

Table 4.2: Table of adsorption energies.

C adsorption energy	E_b^C	630 K
CO adsorption energy	E_b^{CO}	960 K
CO ₂ adsorption energy	$E_b^{CO_2}$	2000 K
CH ₃ adsorption energy	$E_b^{CH_3}$	920 K
CH ₄ adsorption energy	$E_b^{CH_4}$	1100 K
O adsorption energy	E_b^O	630 K
O ₂ adsorption energy	$E_b^{O_2}$	960 K
OH adsorption energy	E_b^{OH}	1000 K
HCO adsorption energy	E_b^{HCO}	1200 K
NH ₃ adsorption energy	$E_b^{NH_3}$	880 K
H ₂ CO adsorption energy	$E_b^{H_2CO}$	1400 K
H ₂ O adsorption energy	$E_b^{H_2O}$	4800 K
S adsorption energy	E_b^S	870 K
Si adsorption energy	E_b^{Si}	2100 K
SiH adsorption energy	E_b^{SiH}	2300 K
SiO adsorption energy	E_b^{SiO}	2800 K
Fe adsorption energy	E_b^{Fe}	3300 K
Mg adsorption energy	E_b^{Mg}	4200 K

4. The cosmic-ray dominated region of disks

This mechanism creates a secondary UV field throughout the midplane of the disk, which can ionize or dissociate molecules (Prasad & Tarafdar 1983). This field is locally extinguished by the local gas and grain opacities. For this reason, the rate of cosmic ray induced UV (CRUV) photoprocesses is given by the photoionization/dissociation cross-section (van Dishoeck et al. 2006) and the dust extinction cross-section (Chaparro Molano & Kamp 2012a, Chapter 2) integrated over the emission probability profile of H₂ (Abgrall et al. 2000).

We estimate a value for the CRUV dust extinction for protoplanetary disk grain parameters, and use this value instead of the standard UMIST (Woodall et al. 2007) value. Thus, we get a lower dust extinction (than in the ISM) because of our use of a larger-grain distribution, and thus we obtain a higher CRUV field in gas-poor regions, which has a significant impact in the chemical evolution of the disk midplane (Chaparro Molano & Kamp 2012a, Chapter 2). This means that we propagate the dust grain extinction properties to the CRUV rates, and thus to the gas-grain chemistry.

For a typical protoplanetary disk dust size distribution $f(a) \sim a^{-p}$, where a is the dust radius (see Table 4.1 for a list of relevant parameters), we can calculate the UV dust opacity for pure silicate grains from the efficiency Q :

$$\kappa_{\text{dust}}^{\text{ext}}(\nu) = \int_{a_{\text{min}}}^{a_{\text{max}}} \pi a^2 Q_{\text{ext}}(a, \nu) f(a) da . \quad (4.2)$$

This opacity has the units of cm² per gram dust. We obtain values for the optical constants from Draine & Lee (1984), assuming a dust composition of 100% silicate. Thus we can also obtain a value for the UV grain extinction cross section per hydrogen nucleus which is 13.6 times lower (Chaparro Molano & Kamp 2012a, Chapter 2) than the one used implicitly in the UMIST rates for CRUV photoprocesses (Sternberg et al. 1987; Woodall et al. 2007). The maximum CRUV photon flux in a gas-poor region of a protoplanetary disk is about 40 times larger here than in molecular clouds (Chaparro Molano & Kamp 2012a, Chapter 2), when compared to previous estimates of 10⁴ photons cm⁻²s⁻¹ (Shen et al. 2004). This CRUV flux is also higher than the stellar UV flux in the disk midplane, which is $F \simeq 0.001 F_{\text{Draine}}$ (Figure 4.1).

CRUV photoprocess rate constants are given in Chapter 3 (Chaparro Molano & Kamp 2012b), and describe the competition for the locally-generated UV photons between a species i and the rest of the gas and dust grains:

$$k_i = 2\zeta_{\text{H}_2} \frac{n_{\text{H}_2}}{n_{\langle\text{H}\rangle}} \int_{1.76 \text{ PHz}}^{3.28 \text{ PHz}} \frac{P(\nu)\sigma_i(\nu)}{\sigma_{\text{tot}}(\nu)} d\nu . \quad (4.3)$$

Here $\sigma_i(\nu)$ is the photo-process cross-section (van Dishoeck et al. 2006), $P(\nu)$ is the H_2 line emission probability for CRUV photons, and $\sigma_{\text{tot},i}(\nu)$ is the total extinction (of both gas and grains) cross-section. In the UMIST (Woodall et al. 2007) literature for CRUV photoprocesses (Gredel et al. 1989), the UV grain extinction dominates over the extinction provided by the gas, and in the interstellar medium this is true to a large extent. This assumption is very convenient for computing the chemical rate equations, as the rate constant does not depend on the gas-phase species abundances. However, this does not apply for gas-rich regions of protoplanetary disks (Chaparro Molano & Kamp 2012b, Chapter 3). In regions of the midplane where temperatures reach values above 20 K, the most important contributors to CRUV gas opacity thermally desorb very efficiently from the surface of grains. Thus, it is very important to include the effects of gas opacity in the chemical models of the midplane of protoplanetary disks. For this reason a consistent calculation of CRUV photoprocess rates should include species abundances and photoprocess cross-sections for relevant gas phase molecules.

4.3 Model description

ProDiMo (Woitke et al. 2009) is a versatile code that allows the calculation of hydrostatic disk models using full 2D dust radiative transfer, gas and ice phase chemistry, photochemistry, and detailed heating and cooling balance for the gas in a self-consistent way. An iterative approach is used to achieve vertical hydrostatic equilibrium that is consistent with the physical conditions set as input parameters. ProDiMo can run a time-dependent chemical model on top of a fully converged disk structure model. The density, dust and gas temperature and UV field strength 2D structure for an Early Solar Nebula model obtained with ProDiMo using the parameters in Table 4.1 are shown in Figure 4.1. Our early solar nebula model was obtained using the prescription for a Minimum Mass Solar Nebula (MMSN) (Weidenschilling 1977), in which the mass and abundances of solids in the solar system are used to estimate a lower limit for the mass distribution of the proto-solar disk. We assume that the disk is passive, which means that the timescale for transport processes is large enough to allow formation of ices on the surface of grains.

We wrote a module for ProDiMo that includes a treatment of CRUV photoprocesses that is consistent with the local physical and chemical conditions prevalent in the midplane of protoplanetary disks. This module includes the effects of CRUV photon flux enhancement due to dust aggregation (Chaparro Molano & Kamp 2012a, Chapter 2) and local gas extinction of CRUV photons (Chaparro Molano & Kamp 2012b, Chapter 3). This allows us to study the time-evolution of the disk midplane

4. The cosmic-ray dominated region of disks

and its ice composition by comparing the models with and without a detailed CRUV treatment, contrasting with the results from Chapter 3 (Chaparro Molano & Kamp 2012b). Benchmarking of this code was also included in Chapter 2 (Chaparro Molano & Kamp 2012a), where the resulting chemical abundances coincide with those obtained from a steady-state chemical model from Woitke et al. (2009), using solar metallicities for the initial abundances. Here we use low metal abundances Jenkins (2009), assuming that Si, Fe, and Mg are condensed on the bulk material of dust grains (Table 4.4).

Table 4.3 shows the 90 species included in our chemical model, including PAH and ice-phase species. For the considered species, 930 chemical reactions from the UMIST (Woodall et al. 2007) database were included in the chemical network. In addition, other special reactions such as H₂ formation on grains (Cazaux & Tielens 2002), ad/desorption processes (Woitke et al. 2009) and PAH reactions were included, for a total of 1100 reactions. For species such as Si, Mg and Fe, adsorption onto the surface of dust grains represents condensation of such elements into the solid phase.

Our chemical models of the Early Solar Nebula correspond to steady-state (S) and time-dependent (T) models in which the CRUV rates are calculated in three different ways: using our self-consistent treatment that includes gas and dust CRUV extinction (S), using a calculation that is consistent with the dust properties while ignoring the effects of local gas CURV extinction, corresponding to a high CRUV field (H), and using a calculation that assumes molecular cloud-like dust extinction while ignoring gas CRUV extinction, corresponding to a low CRUV field (L). Of these six models the time dependent model that includes a self-consistent treatment of CRUV rates is not included here due to computing power limitations. The five models considered here are defined as follows: LS=low CRUV/steady-state, LT=low CRUV/time-dependent, HS=high CRUV/steady-state, HT=high CRUV/time-dependent, and SS=self-consistent CRUV/steady-state.

4.4 Results

In this section we present the main results from the different models of the chemical evolution in the disk midplane for selected species that are relevant to our analysis.

4.4.1 Time dependent models

Model H, which is consistent with the dust parameters of our early solar nebula model, provides a better description of the chemistry in the disk midplane than model

Table 4.3: Table of chemical species in the chemical networks. # indicates an ice species.

Type	Symbol
Atoms	H, He, C, N, O, S, Si, Mg, Fe, Na
Ions	He ⁺ , Si ⁺ , Fe ⁺ , H ⁻ , H ⁺ , C ⁺ , N ⁺ , O ⁺ , S ⁺ , Mg ⁺ , Na ⁺
Molecules	H ₂ , H ₂ O, CH ₂ , HCO, SiO, CO ₂ , NH, NH ₂ , NH ₃ , N ₂ , CN, HCN, NO, SiH, CH ₃ , CH ₄ , OH, O ₂ , CO, CH, H ₂ CO
Molecular Ions	HCO ⁺ , CH ₂ ⁺ , H ₃ ⁺ , SiH ⁺ , SiO ⁺ , CN ⁺ , HCN ⁺ , NH ⁺ , NH ₂ ⁺ , NH ₃ ⁺ , HN ₂ ⁺ , CH ₄ ⁺ , H ₃ O ⁺ , H ₃ O ⁺ SiH ₂ ⁺ , CH ₅ ⁺ , CH ₃ ⁺ , H ₂ O ⁺ , SiOH ⁺ , CH ⁺ , H ₂ ⁺ , NO ⁺ , O ₂ ⁺ , CO ⁺ , OH ⁺ , CO ₂ ⁺
Ice	C#, CO#, CO ₂ #, CH ₃ #, CH ₄ #, S#, HCO#, NH ₃ #, O#, O ₂ #, OH#, H ₂ O#, H ₂ CO#, Si#, SiH#, SiO#, Fe#, Mg#
PAH	PAH, PAH ⁻ , PAH ⁺ , PAH ⁺⁺ , PAH ⁺⁺⁺

Table 4.4: Table of elemental abundances.

Element	$\log(n_X/n_{(H)})$
He	-1.125
C	-3.886
O	-3.538
S	-5.721
Si	-5.1
Mg	-5.377
Fe	-5.367
N	-4.670
Na	-5.00

4. The cosmic-ray dominated region of disks

L, which assumes molecular cloud-like conditions for estimating the CRUV rates. However, model H is only valid in regions of the disk where gas phase abundances are low (Chaparro Molano & Kamp 2012b, Chapter 3). Thus, it is useful to explore the effects of CRUV in the disk midplane chemical evolution, but keeping in mind that those results might not be valid in gas-rich regions of the disk midplane.

Gas phase species

- **Atomic oxygen:** Atomic oxygen is almost completely gone from the midplane in both the steady-state and in the time evolution after 10^3 yr for the low CRUV models LS, LT (Fig. 4.2). In the time-dependent high CRUV model HT (Fig. 4.6) atomic oxygen remains in the 1-5 AU region at 10^6 yr, although it is gone from the midplane in the steady-state model HS (Fig. 4.6).
- **NH₃:** In models LS and HS (Figs. 4.2 and 4.6) there is a moderately high abundance of NH₃ in the midplane. It is interesting to note that in model HS the midplane abundances are a factor 0.2-0.4 lower than in LS. This means that NH₃ is affected by CRUV processes. On the other hand, the NH₃ abundance in the HT and LT (Figs. 4.2 and 4.6) models is much lower, which suggests that its formation timescale is of the order of the disk lifetime.
- **CO:** In the steady state models LS and HS (Fig. 4.2 and 4.6), CO is depleted beyond 3 AU. In the time evolution model LT (Fig. 4.2), CO is evenly distributed throughout the midplane, except at long timescales (10^7 yr) beyond 10 AU. This CO-poor region is smaller in model HT (Fig. 4.6) because the high CRUV flux enhances the formation of gas-phase CO (see Chaparro Molano & Kamp 2012a, Chapter2).
- **CO₂:** Models LS and HS (Figs. 4.2 and 4.6) show only a small region below 1 AU that has a high abundance of CO₂. This CO₂ ring shows up as a pretty stable feature in many models, but has not been discussed in a paper so far. Depending on stellar and dust properties, the ring position and extent move around in r , but it is always around the water snow line. In the LT model (Fig. 4.2), the initial low molecular cloud abundance of CO₂ in the 0.5-3 AU region of the midplane increases from 10^{-6} at 10^3 yr to 10^{-5} at 10^6 yr, and stays at this high level up to 10^7 yr. By contrast, model HT (Fig. 4.6) shows a faster depletion of CO₂ which is caused by the increased CRUV photodissociation rate.
- **CH₄:** This species is very abundant throughout the midplane in the LS and HS model (Figs. 4.2 and 4.6), although model HS shows a lower abundance than

model LS because of enhanced CRUV photodissociation of CH_4 . The initial abundance of CH_4 from molecular cloud conditions increases from 10^3 yr to 10^6 yr in models LT and HT (Figs. 4.2 and 4.6). In this epoch, there is a high (10^{-5}) abundance of CH_4 in two regions of the midplane: from the inner rim to 0.5 AU, and from 3 to 20 AU, although model HT shows a lower abundance in the outer region, caused by CRUV-driven formation of CO. The region in the middle is not fully depleted of CH_4 but has a significantly lower abundance (10^{-7}).

- **H_2CO :** Models LS and HS (Figs. 4.3 and 4.7) show a very small region near 1 AU where this species is moderately abundant. However, the time-dependent models suggest that H_2CO can be present in regions beyond a few AU even at long timescales. The higher CRUV flux favors a higher abundance in model HT (Fig. 4.7).
- **CN:** CN is present in a thin layer in all models, but in the HT models (Fig. 4.7) it also appears in a more extended volume in the outer disk beyond a few AU, especially at 10^6 yr.
- **HCN:** This species is moderately abundant in the regions beyond a few AU in the LT and HT models (Figs. 4.3 and 4.7) at a timescale of 10^6 yr. The region where HCN is abundant corresponds to the same region where the abundance of NH_3 is low. Model HS (Fig. 4.3) shows that HCN formation is enhanced outside of the 3 AU line. This binds approximately 80% of the carbon produced in photodissociation of CH_4 (Figs. 4.2).
- **O_2 :** Molecular oxygen is temporarily abundant in the disk midplane at 10^3 yr (Model LT, Fig. 4.5), but is almost completely gone at 10^6 yr and in model LS. There are no significant differences between the high- and low-CRUV models.

Ice species

- **SiO ice:** Throughout the time evolution (Models LT and HT, Figs. 4.3 and 4.7) SiO ice is present in the 1-30 AU region of the disk, decreasing from 10^{-5} in the 2-5 AU region to 10^{-6} in the 5-30 AU region of the midplane below $z/r = 0.1$. In the HT model, the abundance in this region is about 10 times lower due to the enhanced CRUV field. In the steady state models LS and HS (Figs. 4.3 and 4.7), there is no SiO ice in the 5-30 AU region, although the thin SiO ice region located around $z/r = 0.1$ remains.
- **H_2O ice:** Water ice is very stable and abundant throughout the disk midplane

4. The cosmic-ray dominated region of disks

in all models, although its formation is faster in model LT (Fig. 4.3) than in model HT (Fig. 4.7) due to the lower CRUV flux.

- **H₂CO ice:** Model LT (Fig. 4.4) shows that H₂CO ice forms at an abundance of 10^{-5} - 10^{-4} in the 5-20 AU region of the midplane. On the other hand, it is not present significantly in model LS (Fig. 4.4). There are no significant differences between the high- and low-CRUV models.
- **O₂ ice:** Model LT (Fig. 4.4) shows that this species has a moderate-to-low (below 10^{-8} cm⁻³) abundance beyond 10 AU at 10^3 yr, corresponding to the high gas phase O₂ abundance shown in Fig. 4.5. However, there is no significant presence of O₂ ice in the midplane after 10^6 yr nor it does appear in model LS (Fig. 4.4), suggesting that its survival timescale is lower than 10^4 yr. Oxygen in O₂ goes to CO₂ and CO₂ ice at 10^6 yr (Figs. 4.2 and 4.4). There are no significant differences between the high- and low-CRUV models.
- **CO ice:** A moderate-to-low (below 10^{-8}) abundance of CO ice outside of the 10 AU region is seen in model LT (Fig. 4.4) at 10^3 - 10^6 yr. After this, and in model LS (Fig. 4.4), CO does not form on the surface of grains anywhere in the disk because the radial distribution of dust temperature sets midplane temperatures above 40 K, which are too high to allow efficient formation. We discuss this further in Section 4.4.3. There are no significant differences between the high- and low-CRUV models, and hence we did not plot the corresponding HT, HS models.
- **CO₂ ice:** Model LT (Fig. 4.4) shows that the CO₂ ice abundance increases from 10^{-7} at 10^3 yr to 10^{-4} at 10^6 - 10^7 yr in the 2-30 AU region of the disk midplane. In model LS (Fig. 4.4), CO₂ ice is almost completely gone from the midplane, except in the outer disk ($r \geq 30$ AU). There are no significant differences between the high- and low-CRUV models.
- **CH₄ ice:** Model LT (Fig. 4.4) shows that in the outer regions of the disk midplane (20-30 AU) the abundance of CH₄ ice increases from 10^{-9} at 10^3 yr to 10^{-5} - 10^{-7} at 10^6 - 10^7 yr, respectively. In model LS (Fig. 4.4), the region where the CH₄ abundance is above 10^{-5} extends from 15-30 AU. There are no significant differences between the high- and low-CRUV models.
- **Si (solid):** This species is formed in the 5-30 AU region of the midplane, at an abundance of 10^{-5} throughout the time evolution in model LT (Fig. 4.5). In model LS (Fig. 4.5), the Si ice abundance is similar, but it extends to the 3-30 AU region of the midplane. These high-Si ice abundance regions correspond to the same region where the SiO ice (Fig. 4.3) and SiO (Fig. 4.5) abundances

are low. There are no significant differences between the high- and low-CRUV models.

4.4.2 Comparison with Model SS

In this section we will compare the main results of models LS and HS with the SS model, which includes a self-consistent calculation of the CRUV rates. With this comparison we are able to locate the regions of the midplane where the low-gas opacity assumption used in model HS no longer holds.

Gas phase species

- **NH₃**: (Fig. 4.8) As mentioned in the previous section, this species has a lower gas-phase abundance in model HS than in model LS due to CRUV photodissociation. However, the CRUV photodissociation rate of NH₃ is lower in model SS due to the local gas extinction of CRUV photons. This leads to a factor ~ 7 higher NH₃ abundances in model SS compared to model HS.
- **CO**: (Fig. 4.8) In the inner disk, close to the midplane, model LS agrees with model SS because the high gas phase abundances in this region suppress the effect of the enhanced CRUV flux. Near the $A_V = 1$ surface (Fig. 4.1) and inside 0.5 AU, model HS agrees better with model SS, although this is a very small region.
- **CO₂**: (Fig. 4.8) In the inner disk, the vertical and radial extent of the CO₂ ring discussed in Section 4.4.1 is larger in models SS and HS than in model LS. This means that gas-phase CO₂ molecules are contributing to the CRUV gas opacity in this region (see Chaparro Molano & Kamp 2012b, Chapter 3).
- **CH₄**: (Fig. 4.8) All models agree in that CH₄ is evenly distributed throughout the midplane. However, its abundance is lower in the HS model than in the LS and SS models. This means that CH₄ is contributing to the CRUV gas opacity in the 1–20 AU region of the midplane. The radial gap located near 0.5 AU is caused by the CO₂ ring in models SS and HS, which in those regions also contributes to the CRUV gas opacity.
- **H₂CO**: (Fig. 4.9) Formation of this species in steady-state models is not very efficient. Model SS shows that its inner disk abundance is lower than in the other models.

4. The cosmic-ray dominated region of disks

- **SiO:** (Fig. 4.9) In this case all models look similar, but models SS and HS agree in the vertical extent of the region where SiO is being formed, which is larger than in the LS model.
- **HCN:** (Fig. 4.9) Models SS and LS agree, although there is slightly less HCN close to the midplane in the 1-2 AU region. Thus, we can infer that we see from the comparison that gas opacity is important and thus we trust model SS better than model HS to capture the relevant chemical processes.

Ice species

The ice content of the disk is for the most part independent of the chosen steady-state model (LS, SS, HS).

- **NH₃ ice:** (Fig. 4.9) Models LS and SS agree that there is a small region beyond 20 AU where this species is very abundant. This was expected, as we had shown earlier that gas opacities should not matter in those regions.

4.4.3 Disk ice content

A first-order approximation for the number of monolayers of ice adsorbed on the surface of a spherical dust grain of size a , assuming that each adsorption cell occupies a cubic volume h^3 , is provided by the following formula²:

$$N_{\text{ML}} = \left(\frac{3}{4\pi} \frac{n_{\text{ice}}}{n_{\text{dust}}} + \left(\frac{a}{h} \right)^3 \right)^{1/3} - \frac{a}{h}. \quad (4.4)$$

Here n_{ice} is the total number density of icy species and n_{dust} is the dust number density.

Throughout the midplane, the number of ice monolayers for all models is of the order $N_{\text{ML}} \simeq 500$. However, the number of ice monolayers increases a factor 2 from 10^3 yr to 10^7 yr in the LT and HT models. This suggests that the ice has at least two main layers, a first layer formed before 10^3 yr with a thickness of 500 ML, and a second layer formed before 10^6 yr with a thickness of 500 ML. Figures 4.10 to 4.12 show how the ice composition of the ice mantle of dust grains across the midplane changes at different timescales. Thus, ice species that are formed early in the disk can be preserved in deep layers of the ice mantle of dust grains throughout the time evolution.

²For $N_{\text{ML}} \gg 10$. See Section 5.2 for a detailed derivation of this formula.

Figure 4.12 shows that the steady-state models of the disk chemistry the ice content of the disk is dominated by H₂O, followed by Si and CH₄. At 30 AU, some NH₃ ice shows up as well. These species (with the exception of Si) are found in cometary bodies (Bockelée-Morvan 2010). In particular, the CH₄/H₂O and the NH₃/H₂O abundance ratios agree with those measurements (Table 4.5). In the time dependent models other ice species are also formed within a timescale of 10⁶ yr (Figure 4.11), such as SiO, CO, and H₂CO.

The radial dust temperature profile in Fig. 4.1 shows a shallow temperature gradient³, which has a two-fold effect on the ice composition of the disk. On one hand, temperatures that are low enough to be compatible with a high abundance of CO ice, as observed in our previous models and expected from cometary measurements, are only available in the outermost region of the disk, at distances in the range 25-30 AU. On the other hand, the snow line in our model is closer than 1 AU. This is caused by the dust opacities, which are calculated from dust properties, which to a large extent are free parameters. A different dust parameter choice in the model will cause a steeper dust temperature distribution, which will move the dust line to a larger radius and generate lower dust temperatures in the outer disk. Grain growth can also affect the dust opacities. For example, an ice mantle of 1000 ML thickness will increase the size of a representative dust grain ($a \sim 0.25 \mu\text{m}$) by a factor 2. Besides the dust opacities, viscous accretion can also change the location of the snow line (Min et al. 2011).

4.5 Conclusions

Our time dependent chemical models of the disk midplane show that species such as O, H₂CO, HCN, SiO, CO#, CO₂#, CH₄#, Si#, and H₂CO# form on timescales that are smaller than the lifetime of the disk. The regions of the midplane where such species may form are shown in Table 4.6. Steady-state models yield predictions for the abundances of those species that are too low, except for CH₄# and Si#. These species are formed on very long timescales, thus making steady state models over-predict the true abundance.

The ice mantle of dust grains in the disk midplane has a thickness of 1000-2000 ML. This mantle increases the size of a 0.25 μm sized grain by at least a factor 2. The different ice compositions obtained for different timescales show that some ice species such as CO₂, etc. formed at early stages of the disk evolution may survive

³ProDiMo cannot estimate the disk midplane temperature to a high degree of accuracy due to its limited grid points in the radiative transfer, especially at high optical depths (Pinte et al. 2009).

4. The cosmic-ray dominated region of disks

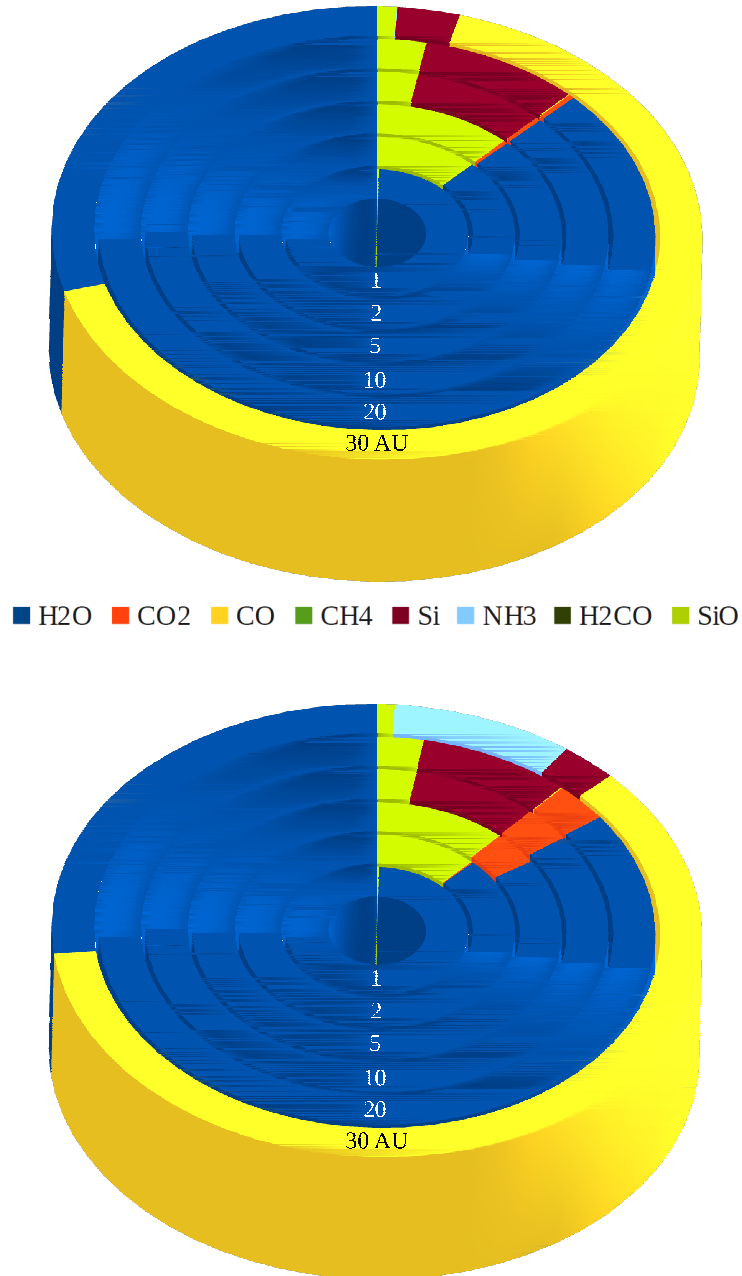


Figure 4.10: Ice content in the midplane by percentage, at 10^3 and 10^4 yr in the time dependent model LT. Radial distances not at scale.

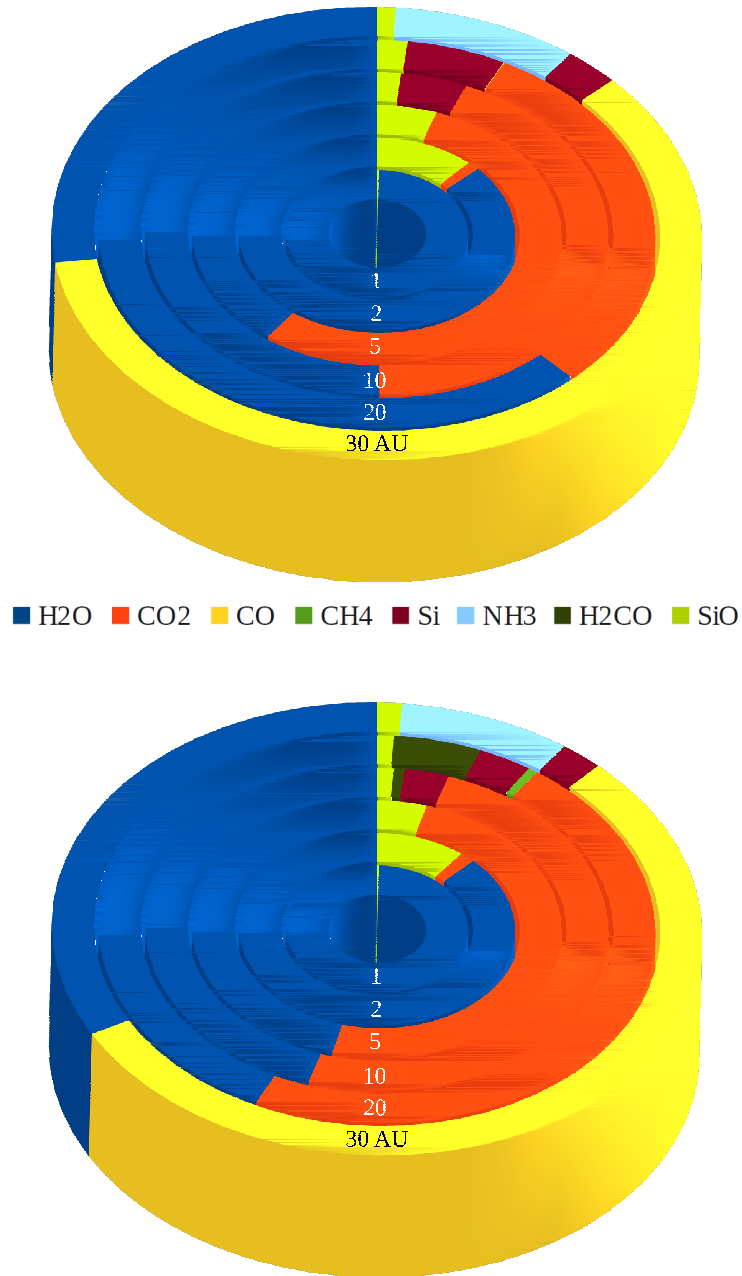


Figure 4.11: Ice content in the midplane by percentage, at 10^5 and 10^6 yr in the time dependent model LT. Radial distances not at scale.

4. The cosmic-ray dominated region of disks

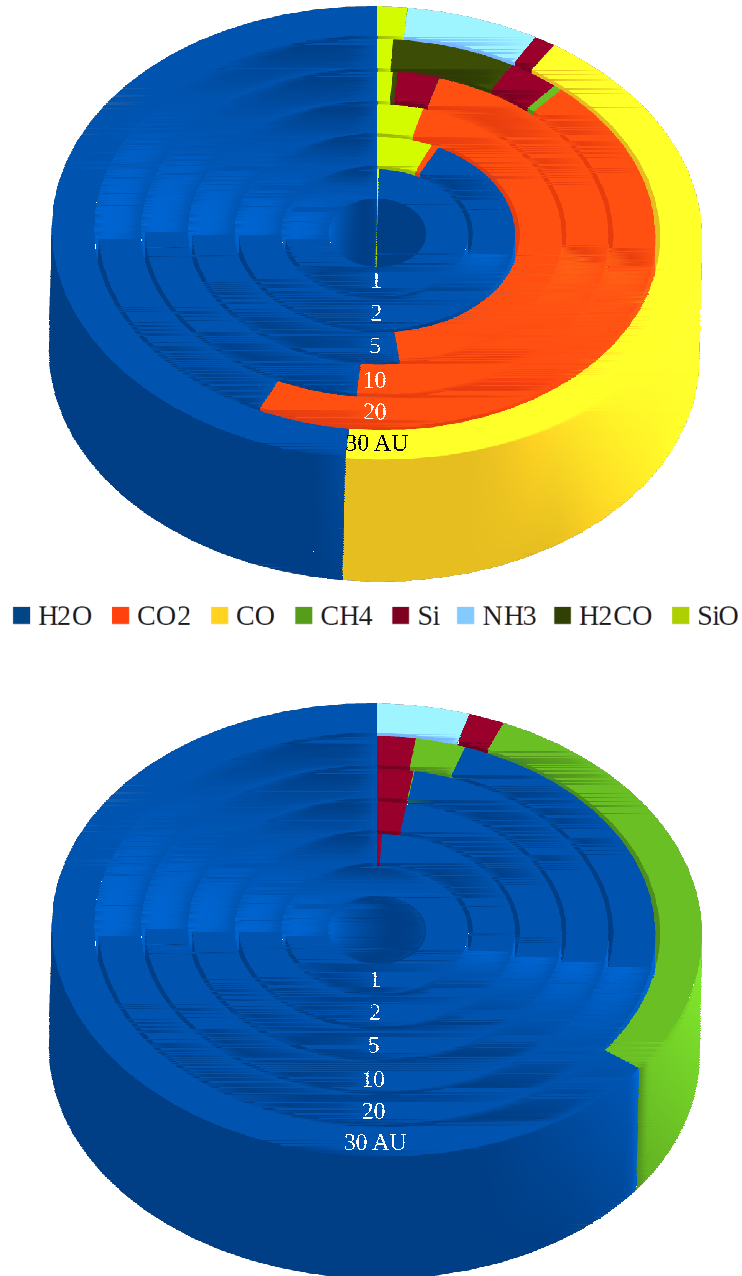


Figure 4.12: Ice content in the midplane by percentage, at 10^7 yr in the time dependent model LT and in the steady-state model SS. Radial distances not at scale.

Table 4.5: Estimated ice ratios in the midplane of the disk obtained with the steady-state (SS) and the time dependent (LT, at 10^6 yr) chemical models. # indicates an ice species.

Ice ratio	Cometary value	SS/LT value	Location
$n_{\text{CH}_4\#}/n_{\text{H}_2\text{O}\#}$	0.005-0.02	0.03-0.45 (SS) 0.03 (LT)	20-30 AU 20 AU
$n_{\text{NH}_3\#}/n_{\text{H}_2\text{O}\#}$	0.007-0.02	0.06 (SS) 0.25 (LT)	30 AU 30 AU
$n_{\text{H}_2\text{CO}\#}/n_{\text{H}_2\text{O}\#}$	0.002-0.02	– (SS) 0.02-0.12 (LT)	10-20 AU
$n_{\text{CO}\#}/n_{\text{H}_2\text{O}\#}$	0.005-0.2	– (SS) 1.5 (LT)	30 AU
$n_{\text{CO}_2\#}/n_{\text{H}_2\text{O}\#}$	0.02-0.11	– (SS) 1.1 (LT)	5-30 AU

buried in the layers closest to the grain solid core.

A comparison between the steady-state models including the effects of CRUV photoprocesses in various degrees of rigor shows that the effects of CRUV gas opacity of CO_2 and CH_4 cause an enhancement in their chemical abundances with respect to those obtained assuming that extinction: for CO_2 this occurs inside of 1 AU and for CH_4 this occurs in the 1–30 AU region. This also causes an enhancement in the formation of NH_3 and $\text{NH}_3\#$.

The CRUV field enhances the formation of SiO and CO near the $A_V = 1$ line in the inner rim, which agrees with results from 3. This could lead to future ALMA detections of SiO in the inner disk.

Appendix: Jacobian for CRUV photoprocesses

In order to obtain a solution for the chemistry it is necessary to compute the jacobian of the chemical rate equation. For the case of CRUV photoprocesses, the corresponding jacobian terms are trivial when the effects of gas opacity are ignored. This happens because the rate coefficients are independent of other chemical abundances. However, if the rate coefficients depend on gas-phase abundances, the corresponding

4. The cosmic-ray dominated region of disks

Table 4.6: Table of chemical species that form in the disk midplane in time dependent models in timescales shorter than the disk lifetime ($\sim 10^6$ yr) and for which steady-state models yield very low abundances in those regions. A # symbol denotes an ice-phase species.

Species	Region
O	>1 AU
H ₂ CO	> 3 – 5 AU
HCN	> 3 – 5 AU
SiO	<1 AU
CO#	>10 AU
CO ₂ #	>5 AU
CH ₄ #	>20 AU
Si#	>10 AU
H ₂ CO#	>10 AU

Jacobian terms are no longer trivially computed. In this addendum to this Chapter, a method for calculating these Jacobian terms is outlined. This implementation is part of the module written for a self-consistent calculation of CRUV rates used in this Chapter.

For $l = 1, N_{\text{CRUV reactions}}$, the CRUV photoprocess rate constant is:

$$\kappa_l = \zeta_{\text{H}_2} \gamma_l . \quad (4.5)$$

Here γ_l is the CRUV photoprocess efficiency as described in Chapter 3 (Chaparro Molano & Kamp 2012b):

$$\gamma_l = \int \frac{P(\nu)\sigma_l(\nu)}{\sigma_{\text{tot}}(\nu)} d\nu . \quad (4.6)$$

If A_i is the total number of reactions that photodissociate a species i , we can rewrite the previous expression as:

$$\gamma_{l(a_i)} = \int \frac{P(\nu)\sigma_{l(a_i)}(\nu)}{\sigma_{\text{tot}}(\nu)} d\nu . \quad (4.7)$$

For $a_i = 1, A_i$. Here $l(a_i)$ is the reaction number of the a_i -th reaction that photodissociates a species i . We define the coefficient $\Gamma_j^{l(a_i)}$ as:

$$\Gamma_k^{l(a_i)} = \frac{\partial \gamma_{l(a_i)}}{\partial n_k} . \quad (4.8)$$

This yields:

$$\Gamma_k^{l(a_i)} = \frac{\partial}{\partial n_k} \left(\int \frac{P(\nu) \sigma_{l(a_i)}(\nu)}{\sigma_{\text{tot}}(\nu)} d\nu \right). \quad (4.9)$$

$$\Gamma_k^{l(a_i)} = - \int \frac{P \sigma_{l(a_i)}}{\sigma_{\text{tot}}^2} \left(\frac{\partial \sigma_{\text{tot}}}{\partial n_k} \right) d\nu \quad (4.10)$$

Since

$$\frac{\partial \sigma_{\text{tot}}}{\partial n_k} = \frac{\partial}{\partial n_k} \left(\tilde{\sigma}_{\langle \text{H} \rangle}^{\text{dust}} (1 - \omega) + \sum_j \frac{n_j}{n_{\langle \text{H} \rangle}} \sigma_j(\nu) \right). \quad (4.11)$$

Thus,

$$\frac{\partial \sigma_{\text{tot}}}{\partial n_k} = \frac{\sigma_j(\nu)}{n_{\langle \text{H} \rangle}}. \quad (4.12)$$

Here

$$\sigma_j(\nu) = \sum_{a_j}^{A_j} \sigma_{l(a_j)}(\nu). \quad (4.13)$$

Therefore, the Γ coefficients are:

$$\Gamma_k^{l(a_i)} = - \frac{1}{n_{\langle \text{H} \rangle}} \int \frac{P \sigma_{l(a_i)}}{\sigma_{\text{tot}}^2} \sum_{a_j}^{A_j} \sigma_{l(a_j)} d\nu. \quad (4.14)$$

This means that the derivative of the rate coefficient k w.r.t. to the molecular abundance of species k is:

$$\frac{\partial \gamma_{l(a_i)}}{\partial n_k} = \zeta_{\text{H}_2} \Gamma_k^{l(a_i)}. \quad (4.15)$$

The rate of formation/destruction of species i is:

$$\frac{dn_i}{dt} = -R_i^- + R_i^+. \quad (4.16)$$

Therefore, the jacobian term (i, k) is:

$$\frac{\partial \left(\frac{dn_i}{dt} \right)}{\partial n_k} = - \frac{\partial R_i^-}{\partial n_k} + \frac{\partial R_i^+}{\partial n_k}. \quad (4.17)$$

The first term is:

$$\frac{\partial R_i^-}{\partial n_k} = \frac{\partial}{\partial n_k} n_i \sum_{a_i}^{A_i} \kappa_{l(a_i)} = \delta_{ik} \sum_{a_i}^{A_i} \kappa_{l(a_i)} + n_i \sum_{a_i}^{A_i} \Gamma_k^{l(a_i)}. \quad (4.18)$$

4. The cosmic-ray dominated region of disks

If B_i is the total number of CRUV photoreactions that have the species i as a product, we can write the second term in the r.h.s of Eq. (4.17):

$$\frac{\partial R_i^+}{\partial n_k} = \frac{\partial}{\partial n_k} \sum_{b_i}^{B_i} n_{i'(b_i)} \mathcal{K}_{l(b_i)} = \sum_{b_i}^{B_i} \delta_{i'(b_i)k} \mathcal{K}_{l(b_i)} + \sum_{b_i}^{B_i} n_{i'(b_i)} \Gamma_k^{l(b_i)}. \quad (4.19)$$

Here $l(b_i)$ is the reaction number corresponding to the b_i -th reaction producing species i from the photodissociation of species $i'(b_i)$. Thus, we can write the jacobian term (i, k) as:

$$\frac{\partial \left(\frac{dn_i}{dt} \right)}{\partial n_k} = -n_i \sum_{a_i}^{A_i} \Gamma_k^{l(a_i)} + \sum_{b_i}^{B_i} n_{i'(b_i)} \Gamma_k^{l(b_i)} + (\dots). \quad (4.20)$$

Here (...) refers to the abundance independent jacobian terms, i.e. the terms calculated in ProDiMo (`chemjacobi`) from the reaction rates. The other two terms are computed in `cruvjac`.

5 Modeling the layering of ices in protoplanetary disks

—G. Chaparro Molano & I. Kamp—

In preparation

*Many years later, as he faced the firing squad,
General Aureliano Buendía was to remember
that distant afternoon
when his father took him to discover ice.*
— Gabriel García Márquez, *One Hundred Years of Solitude* —

Abstract

The study of ice formation and its layering on the surface of dust grains raises an important issue regarding dust grain evolution: grain size distribution models used in protoplanetary disk simulations are very sensitive to ice formation, especially in the dense environment of the disk midplane. In such regions, the amount of ice that adsorbs onto the surface of grains can increase the mean size of dust grains by a non-negligible factor. This effect, along with grain growth due to collisions can affect the grain size distribution on timescales which are shorter than the disk lifetime. We find that in the region of the midplane of our Early Solar Nebula model located at a radial distance of 30 AU from the central star favors the formation of ice mantles with a similar chemical composition to cometary bodies (H_2O , CO , CH_4 , and H_2CO). In this region, the formation of an ice mantle of up to 600 monolayer thickness can increase the size of a $0.2 \mu\text{m}$ grain by a factor 1.76. This yields an ice-to-dust mass fraction of 30% at 10^6 yr, which agrees within an order of magnitude with the assumed ice-to-dust cometary mass ratio of 1:1. Grain growth due to ice mantle formation will then shift the grain size distribution function to larger values, depending on the thickness of the ice mantle. Thus, time-dependent grain growth models need to include the formation of ice layers on dust grain surfaces. This line of research is of particular interest to formation of cometary ices, and is also relevant for dust opacities evolving with time and hence the thermal disk structure changing with time.

5.1 Introduction

The increasing sensitivity of infrared observations of molecular clouds and young stellar objects have revealed the presence of an ever increasing number of icy species. Interstellar ices are detected through their vibrational absorption spectra at infrared wavelengths. Such detections of ices in molecular clouds showed that in highly extinguished regions, mantles of H₂O ice (Gillett et al. 1973) can form on the surface of interstellar grains (Williams et al. 1992). Furthermore, high-resolution observations led to the detection of solid CO along with H₂O in the Taurus dark cloud (Chiar et al. 1995). More recent observations have shown the presence of CO₂ in dark clouds (Whittet et al. 1998, 2007), along with NH₃ (Knez et al. 2005) and CH₄ (Pontopidan et al. 2004). Even more complex, organic species such as formaldehyde and methanol ices have also been detected in molecular clouds and young stellar objects (Gibb et al. 2004; Herbst & van Dishoeck 2009).

One of the earliest surface chemical models for ice formation in molecular clouds was the *ab initio* surface chemical model by Allen & Robinson (1977). A few years later, Tielens & Hagen (1982) developed a more complete surface chemical network model based on inter-atomic reactions using the master equation approach. Hasegawa et al. (1992) used a time-dependent rate equation formalism with a surface chemistry reaction network in order to match observations of H₂O, CO, and CH₄ ices in dark interstellar clouds. More recently, Stantcheva et al. (2002) developed a diffusive model for surface reactions based on reactions among H, O, and CO.

Since Whittet et al. (1998) and Papoular (2005) showed that ice formation is favored in radiation-shielded environments and is sensitive to whether grains are bare or already covered with an ice mantle, interest in a multi-layered approach to interstellar ice formation has grown (Fayolle et al. 2011). Cuppen & Herbst (2007) developed a Monte Carlo model of microscopic growth of monolayers of H₂O ice through its surface-formation, using a small surface reaction network. In a more recent model, Taquet et al. (2012) follow the layering of ices considering up to 60 monolayers in a porous grain surface and show differentiation within the ice mantle material. Current models are greatly improved by surface reaction parameters obtained via laboratory experiments, e.g. Fuchs et al. (2009), Öberg et al. (2009), Ioppolo (2010), and Dulieu et al. (2013).

Another important aspect of surface chemistry is the catalysis of gas-phase species through grain surfaces. McCrea & McNally (1960); Gould & Salpeter (1963); Cazaux & Tielens (2004) showed that observed H₂ abundances could be explained by its for-

5. Ices in protoplanetary disks

mation on the surface of interstellar grains from the exothermic reaction between two adsorbed H atoms. Exothermic surface reactions similar to H₂ formation on grains can also help to form gas-phase H₂O (Ioppolo et al. 2008; Cazaux et al. 2010). Such models are based on Monte Carlo simulations using a grain surface chemical network, while focusing on the importance of hydrogenation and oxygenation effects at different temperatures. At low temperatures (10-20 K), hydrogenation of ices leads to increasing complexity in C- and O-based ices (Charnley et al. 1997; Watanabe & Kouchi 2002) which then form H₂CO and CH₃OH in the ice mantle. These icy molecules are indeed found in embedded young stellar objects (Gibb et al. 2004). At higher temperatures (> 20 K) oxygenation of surface species is found to form O₂, O₃, and subsequently H₂O and other observed ice species (Tielens & Hagen 1982).

In the midplane of protoplanetary disks the local thermochemical conditions allow for the gas-phase formation of molecules such as H₂O, CO, CO₂, CH₄, and H₂CO, which can be rapidly adsorbed onto the surface of dust grains. Except in the hot inner regions of the disk, adsorption of gas-phase species will create a mantle of ices covering the surface of dust grains. In fact, this mantle of ices can be of the order of a few hundred monolayers thick (Chapter 4), which means that the mean grain size is increased by a few tenths of a micrometer.

For typical dust grains in young protoplanetary disks this increment can be of the order of the mean size of the dust grains. Protoplanetary disks older than 1–2 Myr show infrared emission caused by millimeter-sized grains, which means that the average grain size is fairly large. Thus, grain growth by ice mantles is largely important in the youngest phase of a protoplanetary disk when the initial ISM distribution is starting to change due to grain growth into larger sized grains.

This means that grain growth by mantle formation can be a significant effect, especially in studying cometary compositions (Bockelée-Morvan 2010; Chaparro Molano & Kamp 2012a). Whether gas-phase formation of icy species in cometary bodies is the main formation mechanism for ice species, or whether they are formed via surface reactions (A’Hearn et al. 2012) still remains to be seen.

In this Chapter, we analyze the effect of grain growth by ice mantle formation in the chemical evolution of the midplane of protoplanetary disks, focusing on the stratification of icy species within the ice mantle. The structure of this Chapter is as follows: In Section 5.2 we introduce the basics of grain growth of spherical dust grains by formation of icy mantles. Section 5.3 presents the method used for including this effect into our protoplanetary disk chemical models. We present the results in

Section 5.4, and we finish with a discussion and concluding remarks in Section 5.5.

5.2 Spherical dust grain growth

A spherical dust grain that grows an ice mantle will be able to accommodate more ice material per monolayer as its surface area grows. In order to find the number of monolayers of the ice mantle sitting on top of dust grains we need to compare the amount of adsorption sites with the amount of ice that is adsorbed.

The number density of adsorption sites n_{cells} can be derived from the number density of dust grains n_{dust} and the number of adsorption sites per grain, N_{cells} ,

$$n_{\text{cells}} = N_{\text{cells}} n_{\text{dust}} . \quad (5.1)$$

On the other hand, if all available adsorption sites are covered, the number of occupied cells per volume n_{cells} should be equal to the number density of ice species¹, n_{ice} , and thus,

$$n_{\text{ice}} = N_{\text{cells}} n_{\text{dust}} . \quad (5.2)$$

The total number of cells is the fraction between the total adsorption area A_{tot} , i.e. the combined area of all monolayers, and the area of each adsorption site A_{cell} . Thus we can rewrite the previous expression,

$$\frac{A_{\text{tot}}}{A_{\text{cell}}} = \frac{n_{\text{ice}}}{n_{\text{dust}}} . \quad (5.3)$$

Assuming that each adsorption site is a cubic volume of size $h \approx 0.25$ nm, the separation between each monolayer is also h , and $A_{\text{cell}} = h^2$. Thus, the i -th monolayer of ice will increase the grain size $a = \langle a^2 \rangle^{1/2}$ by ih and its area will increase as well,

$$A_i = 4\pi(a + ih)^2 . \quad (5.4)$$

The total area of adsorption will then be the sum of the areas of all monolayers,

$$A_{\text{tot}} = \sum_{i=0}^{N_{\text{ML}}} A_i = \sum_{i=0}^{N_{\text{ML}}} 4\pi(a + ih)^2 . \quad (5.5)$$

Substituting this into Eq. (5.3) we obtain,

$$\sum_{i=0}^{N_{\text{ML}}} 4\pi(a + ih)^2 = \frac{n_{\text{ice}}}{n_{\text{dust}}} h^2 . \quad (5.6)$$

¹This is the sum of the number densities of all species in the ice phase, $n_{\text{ice}} = \sum_i n_{i\#}$.

5. Ices in protoplanetary disks

For $N_{\text{ML}} \gg 1$, the sum reduces to,

$$4\pi \left(\frac{h^2}{3} N_{\text{ML}}^3 + ahN_{\text{ML}}^2 + a^2 N_{\text{ML}} \right) = \frac{n_{\text{ice}}}{n_{\text{dust}}} h^2. \quad (5.7)$$

This expression can be rewritten as,

$$\left(N_{\text{ML}} + \frac{a}{h} \right)^3 = \frac{3}{4\pi} \frac{n_{\text{ice}}}{n_{\text{dust}}} + \left(\frac{a}{h} \right)^3. \quad (5.8)$$

Solving for N_{ML} ,

$$N_{\text{ML}} = \sqrt[3]{\frac{3}{4\pi} \frac{n_{\text{ice}}}{n_{\text{dust}}} + \left(\frac{a}{h} \right)^3} - \frac{a}{h} \quad (5.9)$$

For the particular dust size distribution chosen here (see Table 4.1), $n_{\text{dust}} = 6.04 \times 10^{-14} n_{\text{(H)}}$ and $a = \langle a^2 \rangle^{1/2} = 0.21 \mu\text{m}$. Thus, for a given number of monolayers N_{ML} , the mean dust grain size will increase by an amount $h \cdot N_{\text{ML}}$.

The adsorption rate, and hence the number of ice species deposited on the grain surface per unit time, scales with the mean area of the dust grain. Consequently, the number of monolayers that covers each grain N_{ML} will be the same regardless of its size. Each dust grain then grows in size by a radius given by the same number of monolayers of ice N_{ML} , the minimum and maximum grain sizes increase by the same amount, $a'_{\text{min,max}} = a_{\text{min,max}} + N_{\text{ML}}h$. Since the number of dust grains in a given size interval is conserved, the probability distribution function $f(a)$ is shifted by the same amount by which grains grow, i.e. $f'(a) = f(a - N_{\text{ML}}h)$. After an ice mantle of thickness $N_{\text{ML}}h$ has been deposited on the grain surface, the new mean grain area is,

$$\langle a'^2 \rangle = \int_{a'_{\text{min}}}^{a'_{\text{max}}} a'^2 f'(a) da. \quad (5.10)$$

Substituting a for $a - N_{\text{ML}}h$, we obtain,

$$\langle a'^2 \rangle = \int_{a_{\text{min}}}^{a_{\text{max}}} (a + N_{\text{ML}}h)^2 f(a) da. \quad (5.11)$$

Thus, the new mean area can be calculated from the original distribution moments,

$$\langle a'^2 \rangle = \langle a^2 \rangle + 2\langle a \rangle N_{\text{ML}}h + N_{\text{ML}}^2 h^2. \quad (5.12)$$

This new area can then be used for estimating the new adsorption rate,

$$k_i^a = 4\pi \langle a'^2 \rangle S \sqrt{\frac{kT_g}{2\pi m_i}} n_{\text{dust}}, \quad (5.13)$$

for a sticking probability $S = 1$.

Table 5.1: Distance from the star, temperature, and density conditions corresponding to midplane regions in the Early Solar Nebula Model in Chapter 4, for which the assumption $T_{\text{gas}} = T_{\text{dust}}$ holds. The relevant disk and stellar parameters are found in Table 4.1.

r (AU)	T (K)	$n_{\langle\text{H}\rangle}$ (cm^{-3})
1	100	5×10^{14}
10	40	1×10^{12}
20	30	1.5×10^{11}
30	20	7×10^{10}

5.3 Model

We model the chemical evolution of the midplane of the Early Solar Nebula by solving the chemical rate equation with the solver `chem_compact` at different radii from the star. This solver uses a chemical network based on the UMIST database for Astrochemistry (Woodall et al. 2007), which includes more than 5000 astrophysically relevant gas-phase reactions. Gas-grain reactions such as adsorption and thermal, photo- and cosmic ray-induced desorption are also included (Chaparro Molano & Kamp 2012a, Chapter 2). We also include a treatment of cosmic-ray induced UV photons that is consistent with the local gas and dust extinction (Chaparro Molano & Kamp 2012b, Chapter 3). The local temperature, density and radiation conditions for each probed region of the disk midplane (Table 5.1) are given by the Early Solar Nebula model developed in Chapter 4, obtained using the thermochemical disk modeling code ProDiMo (Woitke et al. 2009)

In order to account for grain growth due to ice mantle formation, at each timestep the total ice content is used to calculate the thickness (in monolayers) of the ice mantle using Eq. (5.9). This value is then used to calculate the new mean radius of the dust grain according to Eq. (5.12), which is used to modify the adsorption rate at each timestep ($k_i^{\text{ads}} \propto \langle a^2 \rangle$). Thus we can trace the grain growth across the time evolution, along with the chemical composition of different layers of the ice mantle.

5.4 Results

Figure 5.1 shows how the mean dust grain radius grows as gas-phase material adsorbs onto the grain surface. Even at a radius of 1 AU, the ice mantle is thick enough to increase the grain size by 38%. This primary mantle is then covered by a secondary mantle, which at radii smaller than 30 AU (corresponding to temperatures of the order of 20 K) causes an additional growth in radius of the order of a few percent. Figure 5.3 shows the number of monolayers in the primary mantle, which is ~ 300 at radial distances above 10 AU. At 1 AU this value is slightly lower because of the higher thermal desorption rate due to warmer temperatures.

On the other hand the thickness of the ice mantle at 30 AU (Figure 5.1) almost doubles in size on a timescale of 10^3 yr, and at 10^6 yr it experiences another increment of 14%. This corresponds to an increment in grain size of 38% from $1-10^3$ yr, 71% at 10^5 yr, and 76% at 10^6 yr. The composition of the different ice mantles formed at 30 AU is shown in Figure 5.4. The primary mantle is mostly made of water ice, followed by CO ice. Si, SiO, and H_2CO ice are also present in this mantle, although at low abundances.

At 10^3 yr a secondary mantle of 250 monolayers of ice is formed, mostly made of CO ice. This secondary mantle is not formed at smaller radial distances because the temperature becomes too high (see Table 5.1) to allow efficient CO ice formation. At this stage, water ice is not very abundant, as the gas-phase water formation is not able to bind all the available oxygen, while the gas-phase formation of CO does. A tertiary mantle, 50 monolayers thick, forms at 10^6 yr and is composed mostly of OH and H_2O ice (Figure 5.4), although some CH_4 ice is also present.

At distances below 20 AU the ice mass is mostly composed of water ice. For this reason, the total ice mass increases the dust mass by about 10% even at 10^6 yr. At 30 AU, the total ice mass increases the dust mass by approximately 16% at 1 yr to 30% at 10^6 yr.

At 1 AU (Figure 5.5) CO gas and water ice contain most of the available oxygen, even though there are small quantities of O_2 . The only species in the ice mantle is H_2O , as the temperature is too high to allow other species to stay on the grain surface. SiO and CO_2 are also present in the gas phase. At larger radial distances this is not the case.

At 10 AU (Figure 5.6) Si, SiO, and H_2CO ice are formed on the grain surface,

although the dominant component is water ice. CO is the main carrier of oxygen in the gas phase, although atomic oxygen is significantly abundant.

At 20 AU (Figure 5.7) the situation is very similar, and the ice mass does not change much. However, at 30 AU there is a richer composition of ices, which can be seen in more detail in Figure 5.8. Cosmic ray induced photodissociation of CO becomes very efficient at a timescale of 10^6 yr (Chaparro Molano & Kamp 2012a, Chapter 2), which frees some of the available oxygen for formation of water, while the remaining carbon goes into CH₄ ice. The high abundance of OH ice is also explained by its high gas-phase formation rate due to cosmic ray-induced UV processes, especially in such gas-poor regions (Chaparro Molano & Kamp 2012b, Chapter 3). If surface reactions were being considered, OH ice would efficiently form gas-phase H₂O (Cazaux et al. 2010), as OH is a radical that would efficiently react with adsorbing H atoms.

Given that we use the Solar Nebula as a base model, the total particle density is slightly different from the the T Tauri model in Chapter 2. Hence, the region in which comets can be formed in this model is pushed outwards in terms of radial distance from the star. CO, H₂CO and CH₄ ice are present, similar as in Chapter 2 but CO₂ is not present in the ice mantle.

5.5 Conclusions

We find that in our Early Solar Nebula Model, the thermal conditions at 30 AU ($T \approx 20$ K) make this a plausible region for the formation of the icy dust grains precursors to cometary bodies. This icy dust contains contains H₂O, CO, CH₄, and H₂CO that is formed in the gas phase and is then adsorbed in a stratified manner onto the surface of dust grains.

The ice composition in our Early Solar Nebula model lacks the presence of CO₂, which is present in our T Tauri model (Chapter 2). This is probably caused by gas extinction of cosmic ray-induced UV photons, which are crucial for the formation of CO₂ ice (Chaparro Molano & Kamp 2012a, Chapter 2). We find that formaldehyde can be trapped in the first ice mantle, and can thus be preserved at very long timescales (from $10^3 - 10^6$ yr). This suggests that the abundance of some icy species is higher than expected when not considering stratification of ices.

The ice/solid fraction of 30% obtained in our Early Solar Nebula model at 30 AU is closer to the cometary ratio of 1:1 for the nucleus (Prialnik 1997) than for our T

5. Ices in protoplanetary disks

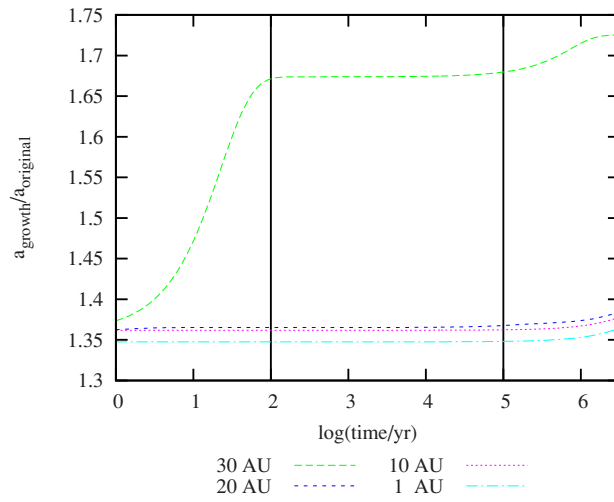


Figure 5.1: Evolution of the mean grain growth size ratio in an Early Solar Nebula model at different radii, showing grain growth due to the formation of an ice mantle (Bare grain mean radius is $\sim 0.21 \mu\text{m}$).

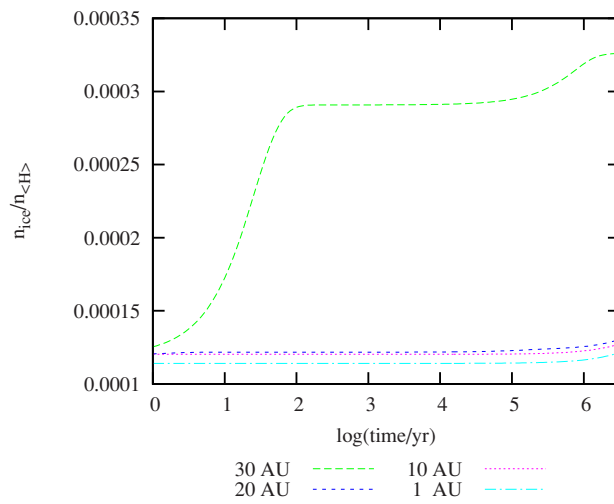


Figure 5.2: Evolution of the total ice abundance in an Early Solar Nebula model at different radii. The abundance (vertical scale) is linear.

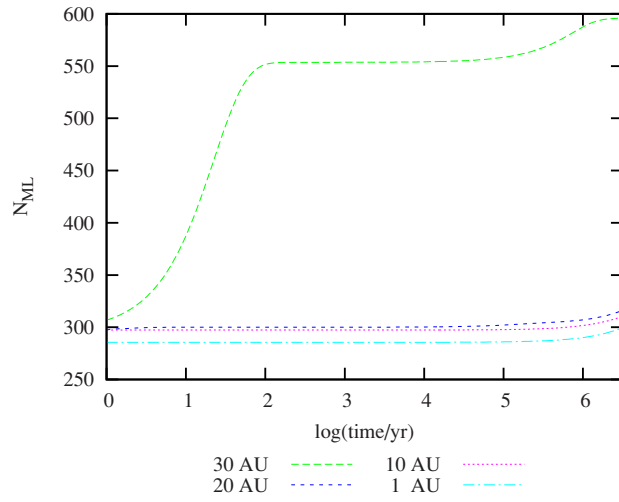


Figure 5.3: Monolayer growth of the ice mantle forming on dust grains in an Early Solar Nebula model.

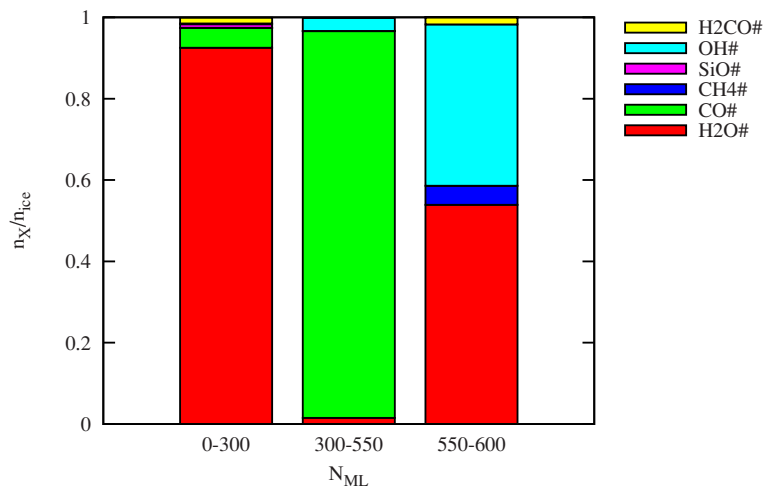


Figure 5.4: Chemical composition of stratified layers in the ice mantle forming on the surface of dust grains at 30 AU.

5. Ices in protoplanetary disks

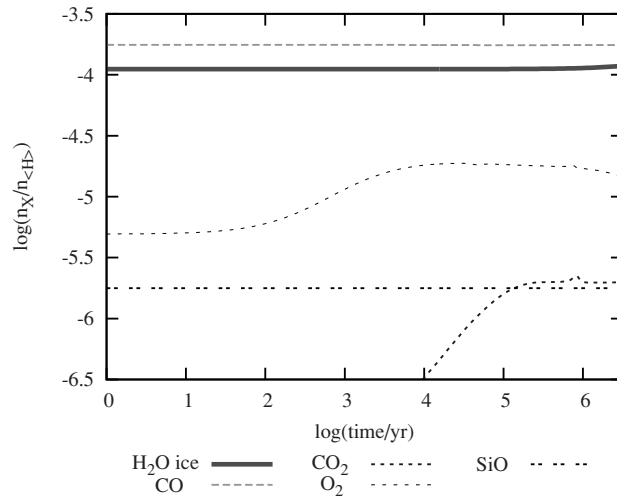


Figure 5.5: Example of the time evolution of gas/ice abundances (thin/thick lines) at 1 AU for an Early Solar Nebula Model.

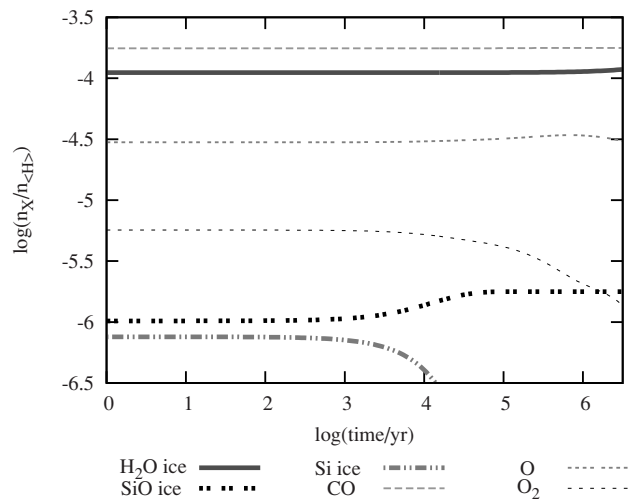


Figure 5.6: Example of the time evolution of gas/ice abundances (thin/thick lines) at 10 AU for an Early Solar Nebula Model.

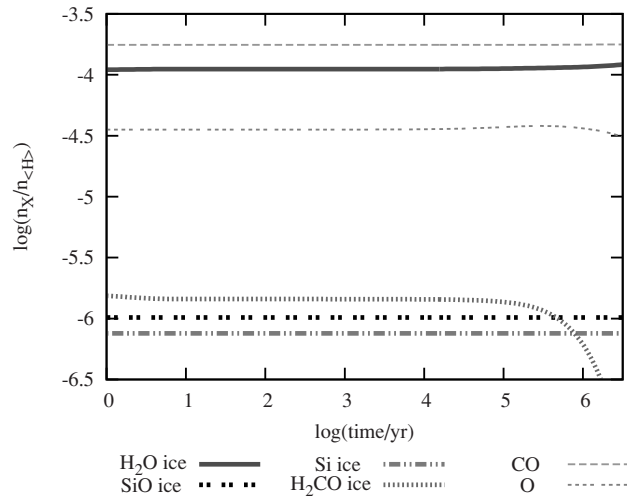


Figure 5.7: Example of the time evolution of gas/ice abundances (thin/thick lines) at 20 AU for an Early Solar Nebula Model.

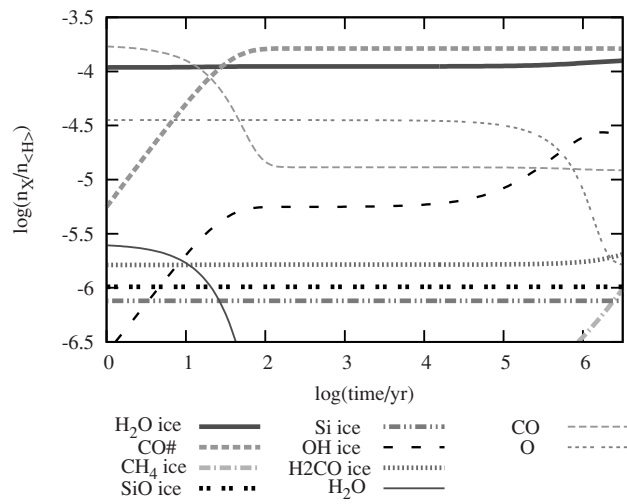


Figure 5.8: Example of the time evolution of gas/ice abundances (thin/thick lines) at 30 AU for an Early Solar Nebula Model.

5. Ices in protoplanetary disks

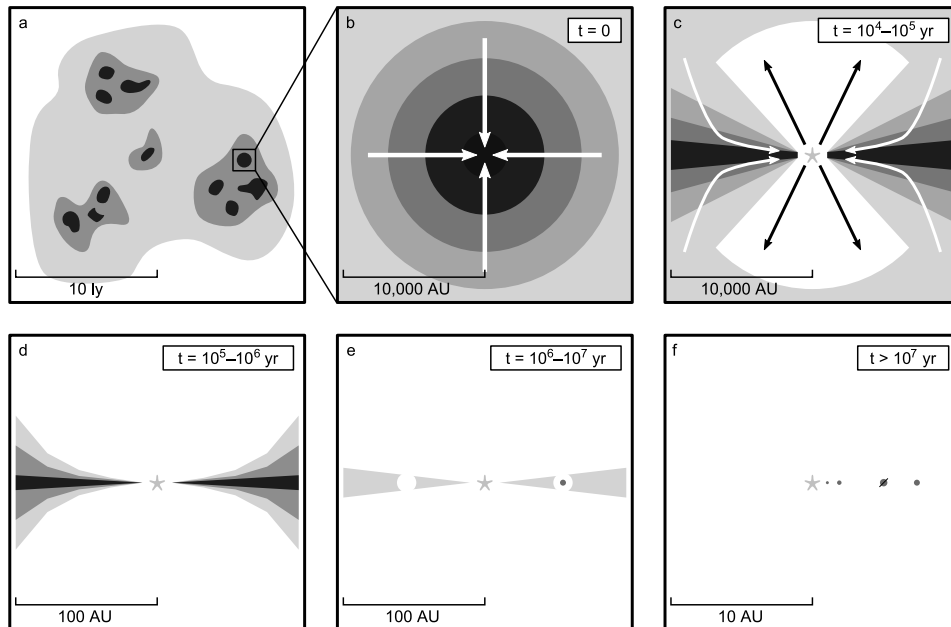
Tauri model in Chapter 2 (25%). The offset may be explained by further processing of small dust grains via aggregation processes along the path to grow into cometary bodies. This is of particular relevance to grain growth models where sticking after a collision may depend on the elasticity and thus on the thickness of the ice mantles.

We show that in most regions of the disk midplane the ice mantle increases the size of dust grains by 38%, and at 30 AU this value goes up to 76%, almost doubling the mean size of the original dust grains. We observe that the effects of grain growth by ice mantle formation are significant enough to change the dust size distribution and the extinction coefficients. This will lead to a change in dust opacities which will in turn affect the thermal structure of the disk midplane. This suggests that in future work the ice information should be used to recalculate the dust opacities in a way that is self-consistent with gas-ice chemistry.

A final consideration is that a three-phase model, where an actively reacting layer of ice sits atop an inert layer of ice which itself sits atop the grain is the next logical step (Wakelam et al. 2010; Fayolle et al. 2011) in implementing a time-dependent simulation of the resulting ice surface chemistry in local models of the midplane of protoplanetary disks. It would also be important to implement new results of diffusion in astrophysical ices research into protoplanetary disk simulations.

Nederlandse Samenvatting

De meest opvallende hint die zou kunnen helpen bij het ontrafelen van de ontstaansgeschiedenis van ons zonnestelsel is het feit dat de banen van de planeten allemaal in hetzelfde vlak liggen en in dezelfde richting om de zon draaien. Deze overeenkomsten suggereren dat de materie waaruit planeten ontstaan zijn, zich oorspronkelijk in een dunne, roterende, schijfvormige wolk bevond. De vraag blijft hoe de ontstaansgeschiedenis van de zon samenvalt met de vorming van planeten. Dateringen van hemellichamen binnen ons zonnestelsel gecombineerd met waarnemingen van jonge sterren lijken erop te wijzen dat de zon tegelijk met de protoplanetaire schijf gevormd is. Dit betekent dat de zon en haar planeten een gemeenschappelijke oorsprong hebben: een oerwolk met een diameter van tientallen lichtjaren en een massa van miljoenen zonsmassa's die bestaat uit moleculair gas en stofdeeltjes. Als een fragment van deze wolk onder invloed van de zwaartekracht in elkaar stort, zou dit kunnen leiden tot de vorming van de zon samen met een circumstellaire schijf. Dit kan dan later evolueren in het zonnestelsel zoals we dat vandaag de dag kennen (Figuur 1). Dit model voor de vorming van het zonnestelsel wordt ook wel de nevelhypothese genoemd, naar de theorie die in de 18e eeuw door Swedenborg, Kant en Laplace ontwikkeld is. Zij stelden dat de ineenstorting van een enkele nevel tot de vorming van het zonnestelsel geleid zou kunnen hebben. Waarnemingen van jonge sterren met hun eigen circumstellaire, of protoplanetaire schijf lijken erop te wijzen dat dit proces niet uniek is voor de vorming van ons eigen zonnestelsel. Sterren met een massa ongeveer gelijk aan die van de zon die omringd zijn door een schijf, worden ook wel T Tauri sterren genoemd. Een ster die omgeven is door stofdeeltjes met een diameter van een μm tot een mm zendt extra veel infrarood (IR) licht uit. Dit effect loopt door tot licht met golflengtes korter dan een mm. Ons doel in dit boekwerk is het samenweven van de theorieën en waarnemingen van de chemische en fysische evolutie van protoplanetaire schijven, samen met onderzoek aan het zonnestelsel, in



Figuur 5.9: De vorming van het zonnestelsel. De oerwolk is gefragmenteerd (a) en één van deze fragmenten wordt een donkere kern (b), die in het centrum van de ineenstorting een protoster vormt. Om het oorspronkelijke hoekmoment van de wolk te behouden, vormt zich binnenin de kern een schijf rond de protoster. In deze fase wordt de protoster afgeschermd door de optisch dichte omhullende wolk (c). Nadat dit omhulsel is weggesneden door gasstromen blijft er een dunne accretieschijf over (d). Nadat accretie en verdamping door licht hebben plaatsgevonden, wordt er een schijf van puin gevormd (e) en zijn er al planeten zichtbaar. Tenslotte vangen de planeten het overgebleven stof van de schijf op en is er een planetair systeem gevormd (f). Bron: Ioppolo/Visser/Hogerheijde.

een model voor de vorming van het zonnestelsel.

Van stof tot planeten

Stofdeeltjes in de oerschijf kunnen groeien door een proces dat coagulatie heet. In dit proces klonteren stofdeeltjes samen onder invloed van botsingen bij langzame snelheden. Een ander belangrijk proces is sedimentatie, waarbij stofdeeltjes boven het draaiingsvlak van de schijf afzinken naar dit vlak. Samen zorgen coagulatie en sedimentatie ervoor dat stofdeeltjes van ongeveer een micrometer doorsnede samenklonteren tot klompen van ongeveer een meter doorsnede. Als sedimentatie plaatsvindt kunnen lokale zwaartekrachtsinstabiliteiten de coagulatie versnellen. Dit leidt tot de

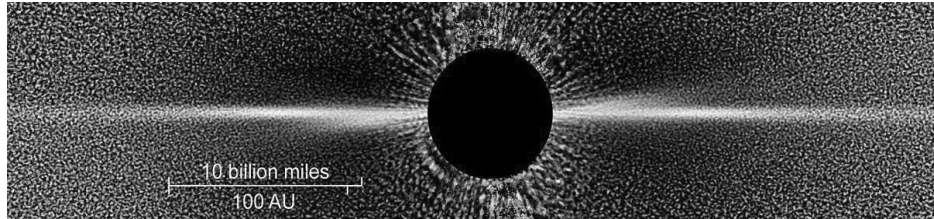
vorming van planeetachtige objecten, klompen materie van ongeveer een kilometer doorsnede die de bouwstenen van planeten vormen. Op afstanden van de centrale ster kleiner dan de zogenoemde kritische straal is de temperatuur van de schijf zodanig hoog dat het onmogelijk is om ijs-achtige substanties te vormen. In dit gebied worden de pure steenplaneten, zoals de Aarde, gevormd. In het geval van massievere entplaneten leidt invang van gas uit de voedingszone op de entplaneten tot de vorming van Jupiter-achtige gasplaneten.

Meteorieten en kometen

Meteorieten en kometen zijn hemellichamen uit ons eigen zonnestelsel die oorspronkelijk deel uitmaakten van de protoplanetaire schijf waaruit de planeten zijn gevormd. Bij deze objecten werd het groeiproces gestopt voordat ze konden volgroeien tot planeten. Meteorieten kunnen, afhankelijk van hun samenstelling, ingedeeld worden in grofweg drie categorieën: Steenachtige, IJzerachtige en Steen-IJzer meteorieten. Steenmeteorieten zijn met 80 - 90% de meest voorkomende categorie, gevolgd door de IJzermeteorieten (4 - 20%). Steenmeteorieten zijn op hun beurt weer onderverdeeld in chondritische en achondritische meteorieten. De term chondritisch slaat op de aanwezigheid van chondrules, oude silicium-houdende stofkorrels van een paar micrometer tot ongeveer een centimeter doorsnede, die tijdens hun vorming zijn blootgesteld aan temperaturen van ongeveer 1600 K. Kometen hebben ongeveer dezelfde minerale samenstelling als chondritische meteorieten, maar bevatten daarnaast ook nog bevroren H₂O, CO en CO₂ en veel verschillende organische stoffen. Aangezien kometen ijs bevatten, denkt men dat zij voorbij de huidige baan van Jupiter gevormd zijn. Metingen van de samenstelling van het ijs in kometen, zowel vanaf de Aarde als vanuit de ruimte, tonen een duidelijke correlatie aan met de overeenkomstige interstellair abundancies. Deze correlatie geldt echter niet voor CO₂ en CH₄, welke wel gevonden worden in kometen maar zeer weinig voorkomen in het interstellair medium. Dit betekent dat een interstellair oorsprong van kometen is uitgesloten.

Waarnemingen van schijven

De Infra-Rode Astronomische Satelliet (IRAS) was in 1983 de eerste grootschalige poging om sterke infrarode bronnen zowel binnen als buiten de Melkweg waar te nemen. In dit overzicht werden enkele jonge sterren gevonden die extra veel licht in het infrarood uitzonden. Men ging er van uit dat deze infrarode overmaat tot stand kwam doordat de sterren omhuld worden door een sluier van warme stofdeeltjes met een doorsnede van enkele micrometers. β Pictoris was een van de eerste sterren waarbij de infrarode overmaat werd geïnterpreteerd als een teken van een schijf van

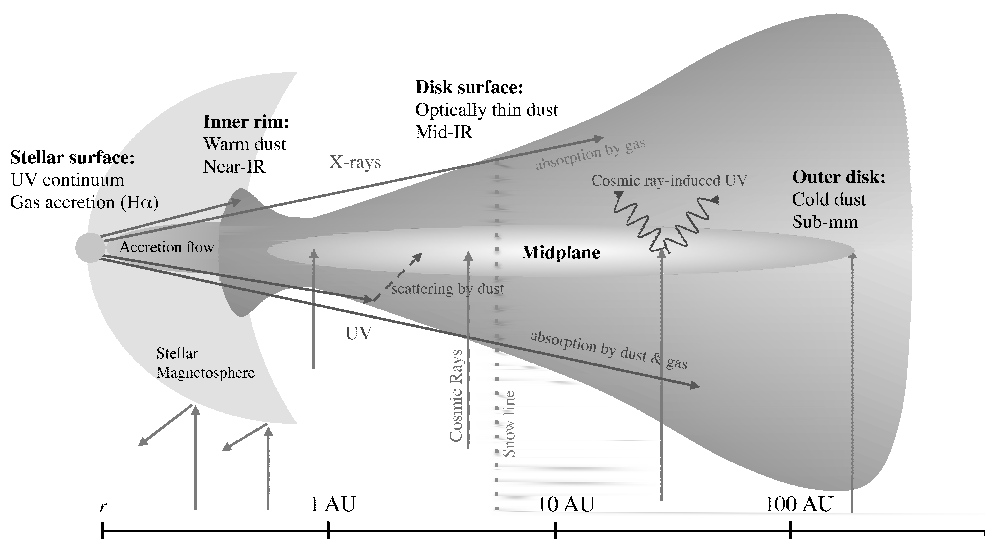


Figuur 5.10: Een afbeelding van de circumstellaire schijf rondom β Pictoris, gemaakt door de Hubble Space Telescope. (Bron: ESA).

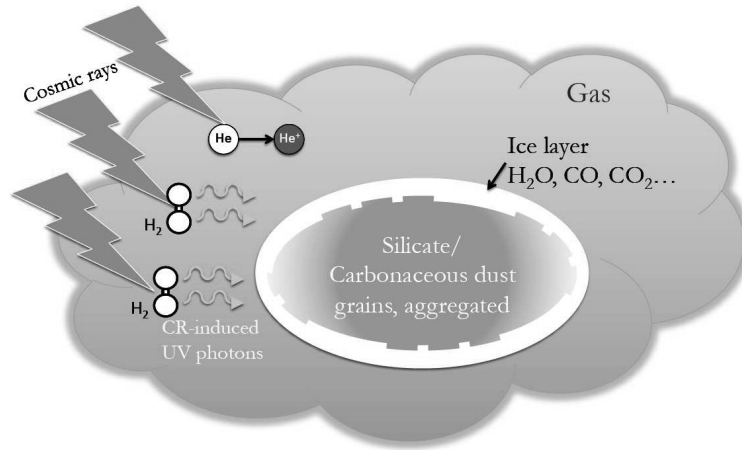
circumstellair stof (Figuur 2). Meer waarnemingen van jonge, zon-achtige sterren met een circumstellaire schijf leerden dat β Pic een voorbeeld is van een gas-arme puinschijf. Aan de andere kant kwam men er achter dat sterren met een gasrijke circumstellaire schijf hun jongere tegenhanger zijn, die nu bekend staan als T Tauri sterren. Deze T Tauri sterren hebben een veel sterkere infrarode overmaat, hetgeen verklaard kan worden door de aanwezigheid van een massieve circumstellaire schijf van stof en gas. Het hemellichaam T Tauri is sindsdien een prototype geworden voor alle pre-hoofdreeks sterren van ongeveer een zonsmassa die omringd worden door een schijf van stof en gas. Het is een van de vele sterren van dit type die gevonden zijn in Taurus-Auriga, een stervormingsgebied op een afstand van 140 parsec. Taurus-Auriga bevat naast T Tauri sterren ook zogenoemde donkere wolken en Herbig Ae/Be sterren. Donkere wolken ontleen hun naam aan het feit dat zij alleen op ver-infrarode golflengtes zichtbaar zijn, en Herbig Ae/Be sterren vertonen dezelfde kenmerken als T Tauri sterren, afgezien van hun massa, die groter is dan twee zonsmassa's. Protoplanetaire schijven worden gekarakteriseerd door een spectrale energie verdeling (Spectral Energy Distribution, SED), waarvoor verschillende waarnemingen in golflengtegebieden variërend van nabij-infrarood tot millimeter-emissie met elkaar gecombineerd worden. Het is mogelijk om vanuit een meer-zones perspectief de structuur van een schijf te reconstrueren uit de algemene eigenschappen en specifieke kenmerken van een SED (Figuur 3).

Kosmische straling en de chemie van een schijf

Kosmische straling bestaat uit hoog-energetische deeltjes die isotropisch ontstaan in schokgolven. Deze schokgolven zijn het resultaat van supernova's en vinden plaats in de hele Melkweg. Deze kosmische straling werd in het begin van de 20e eeuw voor het eerst gedetecteerd tijdens experimenten met radioactieve elementen. Het werd gedetecteerd doordat er toch ionisaties, veroorzaakt door de kosmische straling,



Figuur 5.11: Structuur van een schijf en de belangrijkste stralingskenmerken. Chemisch gezien kan de protoplanetaire schijf verdeeld worden in drie lagen. Aan het oppervlak van de schijf zorgt UV-straling van de centrale ster voor een hete laag ($T > 1000$ K) van geioniseerde en atomaire stoffen (C^+ , C, N, H, O). Onder deze laag worden in de gasfase moleculen gevormd (H_2 , CO, HCN, OH, H_2O , CO_2 , N_2). Deze moleculen kunnen overleven dankzij de warme omstandigheden ($T > 100$ K). In het koude middenvlak ($T < 80$ K) van de schijf, condenseren veel stoffen vanuit de gasfase op de stofdeeltjes (CO, CH_4 , CO_2). In dit gedeelte van de schijf worden ook de eenvoudige organische moleculen gevormd die in kometen gedetecteerd zijn, zoals CH_4 en H_2CO . Figuur is gebaseerd op Dullemond & Monnier (2010).



Figuur 5.12: Het milieu van gas en stofdeeltjes en de processen die door kosmische straling gestart worden.

plaatsvonden in de reactiekamer terwijl er geen radioactief sample aanwezig was. Kosmische straling bestaat voor het grootste gedeelte uit protonen en atoomkernen en de gemiddelde kinetische energie heeft een ordegrrootte van ongeveer 1 GeV per nucleon. Men verwacht dat deze kosmische straling een belangrijke rol speelt bij het ioniseren en verhitten van de materie in een protoplanetaire schijf. Het bestuderen van de invloed van kosmische straling op de chemische evolutie van het middenvlak van de schijf geeft inzicht in de manier waarop ijs en eenvoudige organische verbindingen worden gevormd in protoplanetaire schijven.

Dit proefschrift

In dit proefschrift proberen we de chemische omstandigheden van het prille zonnestelsel vast te leggen. Dit doen we door modellen van de chemische evolutie van protoplanetaire schijven te analyseren en te vergelijken met onze huidige kennis van de chemische samenstelling van hemellichamen binnen ons zonnestelsel, zoals kometen. Om dit te kunnen bereiken hebben we consistente stralings- en hydrodynamische modellen van protoplanetaire schijven nodig. Met deze modellen kunnen we de lokale temperatuur, dichtheid en het stralingsveld bepalen van de omgeving waar de gas- en stofchemie plaatsvindt. Gegeven het feit dat het gedeelte van de protoplanetaire schijf waar de planeten (en kometen) gevormd worden samenvalt met het middenvlak dat gedomineerd wordt door kosmische straling, richten we onze aandacht ook op het begrijpen van de rol van processen die afhankelijk zijn van kosmische

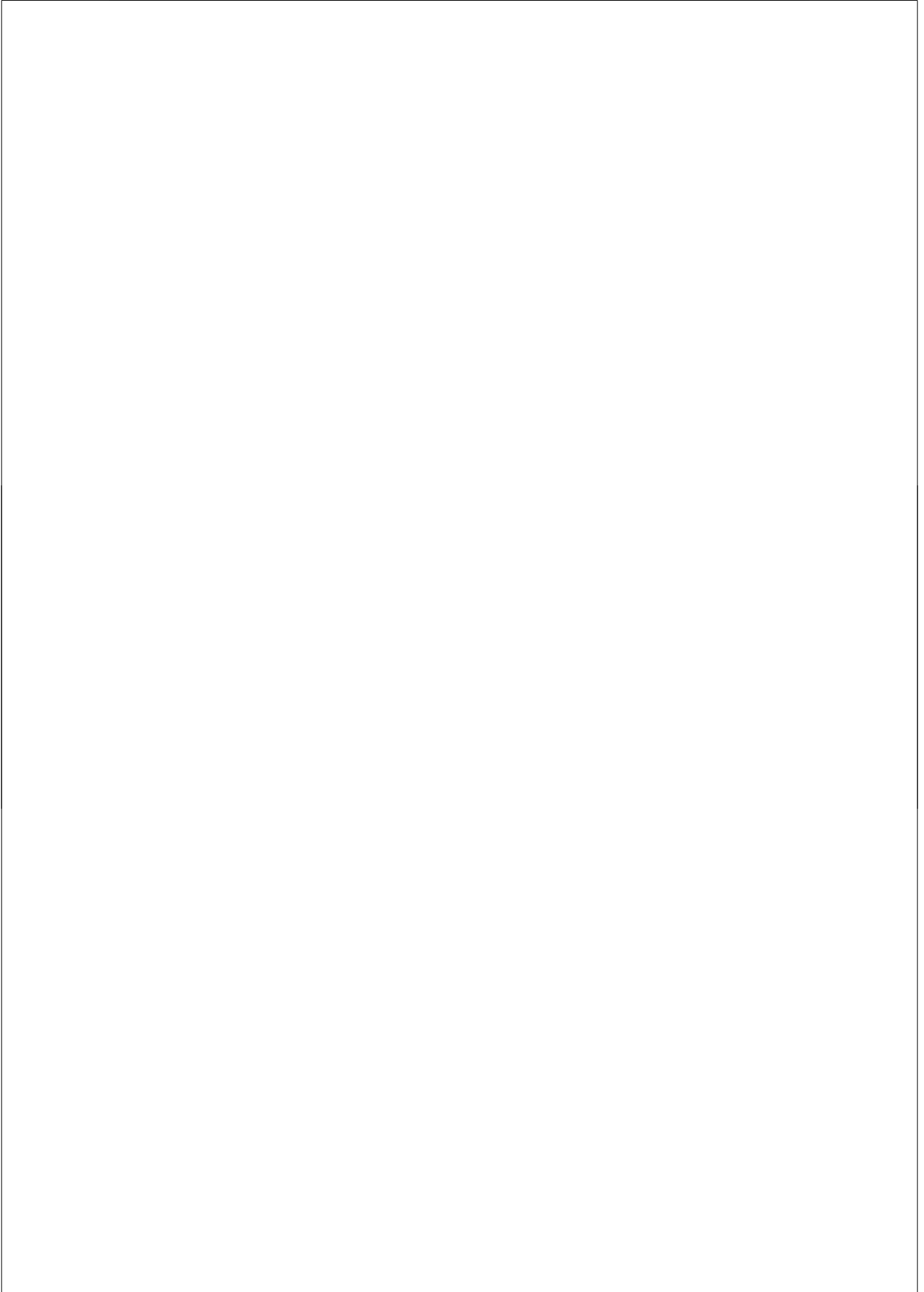
straling (Figuur 4).

In hoofdstuk 2 (Chaparro Molano & Kamp 2012a) laat ik een tijdsafhankelijke analyse zijn van de gas- en stofchemie in koude, gas-arme gedeeltes van protoplanetaire schijven. Tevens laat ik een methode zien om de snelheid van processen die aangedreven worden door UV-licht, dat afkomstig is van kosmische straling (Cosmic Ray induced UV, CRUV), te berekenen op een manier die consistent is met de extinctie door stof in een protoplanetaire schijf. Ik kom tot de conclusie dat in het midden van de schijf, op een straal groter dan 10 maal de afstand tussen de Aarde en de Zon, de thermische omstandigheden zijn voor de vorming van ijs-achtige substanties die overeenkomen met abundanties geobserveerd in kometen.

Ik verken de chemische evolutie van gasrijke gebieden van protoplanetaire schijven in hoofdstuk 3 (Chaparro Molano & Kamp 2012b). Verder verbeter ik de berekening van de snelheid van de processen die door het UV-licht van kosmische straling worden aangedreven door ook de effecten van locale gas extinctie mee te nemen. Ik zie dat de optische dichtheid van het gas in de gasrijke gebieden van het middenvlak ($r < 10$ AE) bijna 30% is van de totale optische dichtheid. CO, CO₂, SiO en OH blijken vanuit de gasfase de belangrijkste bijdrage te leveren aan de extinctie van UV-licht dat door kosmische straling wordt veroorzaakt.

In hoofdstuk 4 breid ik de methode voor de zelfconsistente berekening van CRUV reactiesnelheden, ontwikkeld in de vorige twee hoofdstukken, uit naar een 2 dimensionaal model van een schijf. Ik bestudeer de effecten van CRUV in de chemische evolutie van het gas en de ijssoorten en ontdek dat steady-state modellen de hoeveelheid ijs onderschatten. Verder bekijk ik de mogelijkheid dat de ijssoorten die eerder in de evolutie van de schijf gevormd zijn, dichter op het oppervlak van de stofkorrels zitten. Op die manier wordt er een gelaagde ijsmantel gevormd.

In hoofdstuk 5 vestig ik de aandacht op de gelaagde vorming van ijs op het oppervlak van bolvormige stofkorrels. Ik kom erachter dat in de meeste gebieden van het middenvlak van de schijf de stofkorrels een primaire ijsmantel hebben van ongeveer 300 monolagen dik. Op een afstand van 30 astronomische eenheden wordt een secundaire ijsmantel gevormd, waardoor de totale ijsmantel twee keer zo groot wordt. Deze groei van de mantel zorgt voor een groei van de totale stofkorrel, die van 0.2 μm kan toenemen tot bijna 0.4 μm . Een dergelijke verandering in de stofdistributiefunctie heeft zijn weerslag op de optische dichtheid van stof (en daarmee op het temperatuurprofiel van het middenvlak) en de effectiviteit van het kleven na een onderlinge botsing (hetgeen de coagulatie van stof bevordert).



Resumen en Español

Una de las pistas más evidentes que nos permite resolver el misterio de la formación del Sistema Solar es que las órbitas de los planetas son coplanares, rotando todas en la misma dirección. Este común denominador sugiere que la materia primordial que formó los planetas era un disco delgado y rotante. Pero, cómo podemos conectar la formación del Sol con la formación de los planetas? Tanto el fechado de cuerpos del Sistema Solar como las observaciones actuales de estrellas jóvenes, sugieren que el Sol se habría formado al mismo tiempo que el disco primordial. Esto significa que el Sol y sus planetas comparten un origen común: una *nube molecular* primordial compuesta de gas y polvo, con una extensión de decenas de años luz y con un peso de millones de masas solares. El colapso gravitacional de un fragmento de esta nube dio vida al Sol junto a su disco circunestelar, que luego evolucionó para formar el Sistema Solar como lo conocemos (Figura 1). Este modelo para la formación del Sistema Solar es históricamente conocido como la *hipótesis nebular*. Este nombre viene de la teoría desarrollada en el siglo XVIII por Swedenborg, Kant y Laplace, quienes argumentaron que el colapso de una simple nebulosa podría haber dado vida al Sistema Solar. En general, las observaciones de estrellas jóvenes con sus propios discos circunestelares, o discos *protoplanetarios* sugieren que ese proceso de formación no es exclusivo de nuestro Sistema Solar. Las estrellas de masa solar que están rodeadas por un disco son convencionalmente conocidas como *estrellas tipo T Tauri*. Generalmente, una estrella joven rodeada por polvo micrométrico o milimétrico muestra un exceso infrarrojo (IR) que se extiende a observaciones sub milimétricas. En este trabajo, nuestra meta es entretelar las teorías y observaciones de la evolución química y física de discos protoplanetarios junto con la formación del Sistema Solar.

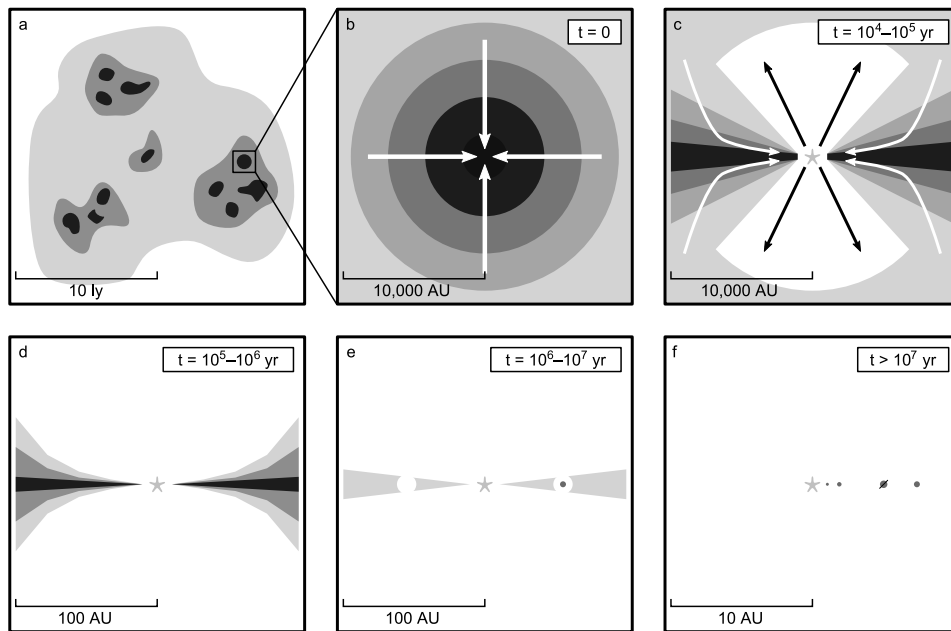


Figura 5.1: La formación del Sistema Solar. La nube molecular se fragmenta (a), y uno de dichos fragmentos se convierte en un núcleo oscuro (b), que forma una *protoestrella* en el centro del colapso. En el núcleo, un disco se forma alrededor de la protoestrella, conservando el momento angular inicial de la nube colapsante. En este momento, la protoestrella es oscurecida por una envoltura que es ópticamente gruesa (c). Queda un disco de acreción delgado, o *disco protoplanetario* luego de que la envoltura es tallada por caudales de materia (d). Luego de la acreción y fotoevaporación, queda un *disco de escombros* (e), y los planetas se pueden ya observar. Finalmente, los planetas limpian el polvo que queda en el disco y nace así un sistema planetario (f). Crédito de la imagen: Ioppolo/Visser/Hogerheijde.

De polvo a planetas

El polvo en el disco primordial crece gracias a un proceso conocido como *coagulación*, en el cual las partículas de polvo se aglomeran tras colisiones lentas gracias a fuerzas de adhesión microscópicas. Este proceso combinado con la *sedimentación* del polvo, en el cual el polvo se que ubica inicialmente sobre el plano de rotación del disco se mueve verticalmente hacia este plano, inicia el crecimiento de partículas micrométricas que se vuelven cuerpos de tamaño métrico. Si el asentamiento toma lugar, inestabilidades gravitacionales locales pueden acelerar el proceso de coagulación, que lleva a la formación de objetos de tamaño kilométrico conocidos como *planetesimales*, que son los bloques de construcción de los planetas. En regiones donde la temperatura del disco es suficientemente alta para prevenir la formación de hielos, se forman planetas rocosos como la Tierra. En el caso de planetas más masivos, más acreción de gas sobre la semilla del planeta, lleva a la formación de los planetas gaseosos, como los Jovianos.

Meteoritos y cometas

Los meteoritos y cometas son cuerpos del sistema solar que eran originalmente parte del disco protoplanetario del cual se formaron los planetas. Sin embargo, el proceso de crecimiento de polvo a planetas paró para ellos antes de que pudieran formar objetos más grandes. Los meteoritos pueden ser clasificados en tres clases de acuerdo a su composición: De piedra, de hierro, y meteoritos de piedra y hierro. Los meteoritos de piedra son el tipo más común (80 - 90%) seguidos de los de hierro (4 - 20%). A su vez, los meteoritos de piedra son divididos en dos grandes subclases: condriticos y acondriticos. El término *condritico* hace referencia a la presencia de *cóndrulos*, los cuales son aglomerados de polvo que experimentaron procesos térmicos ($T \approx 1600$ K) durante su formación, y miden desde unos pocos mm hasta ~ 1 cm. Los cometas son similares a algunos meteoritos condriticos en su composición mineral, pero contienen también hielos como H_2O , CO, CO_2 , y muchas especies orgánicas. Por su contenido de hielo, se piensa que fueron formados más allá de la órbita actual de Júpiter. Mediciones de la composición de los hielos cometarios muestran una muy buena correlación con las abundancias interestelares correspondientes. Sin embargo, esta correlación se rompe para el CO_2 y CH_4 , que son especies detectadas en cometas y no son muy abundantes en el medio interestelar. Esto descarta un origen interestelar para los cometas.

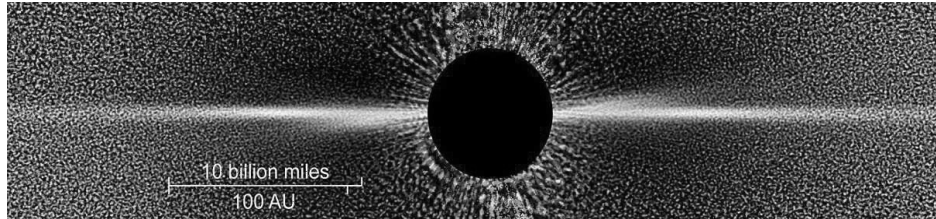


Figura 5.2: Imagen del Telescopio Espacial Hubble del disco circunestelar de β Pic (Crédito de la imagen: ESA).

Observaciones de discos

En 1983, el Satélite Astronómico Infrarrojo (IRAS) fue el primer intento a gran escala para observar fuentes galácticas e intergalácticas cuya emisión infrarroja fuese intensa. En ese estudio, algunas estrellas jóvenes mostraron un exceso infrarrojo muy fuerte. La hipótesis es que este exceso es causado por una envoltura de polvo caliente de tamaño micrométrico alrededor de la estrella. Una de las primeras estrellas cuyo exceso IR fue interpretado como una señal de un disco de polvo circunestelar, fue β Pictoris (Figura 2). Más observaciones de estrellas jóvenes de masa solar dotadas con discos circunestelares muestran que β Pic es representativa de discos de escombros, con bajo contenido de polvo. Por otro lado, se encontró que estrellas con discos circunestelares ricos en gas eran sus contrapartes más jóvenes, ahora conocidas como estrellas T Tauri. Las estrellas T Tauri muestran un exceso de IR más intenso, el cual es explicado por la presencia de un disco circunestelar masivo, rico en gas y polvo. El objeto conocido como T Tauri se ha convertido en el prototipo de todas las estrellas presecuencia principal de masa solar que están rodeadas por un disco de polvo y gas. Esta es la primera de muchas de su tipo encontradas en Taurus -Auriga, una región de formación de estrellas localizada a una distancia de 140 pc. La caracterización de los discos protoplanetarios se realiza por medio de la Distribución de Energía Espectral (Spectral Energy Distribution, SEDs), donde se combinan observaciones a diferentes longitudes de onda, cubriendo emisiones del infrarrojo cercano al lejano. De las propiedades generales y específicas de las SED, es posible reconstruir la estructura de un disco desde un punto de vista multizonal (Figura 3).

Rayos cósmicos y química en discos

Los rayos cósmicos son partículas de alta energía que son generadas isotrópicamente en eventos de choques de supernova a lo largo y ancho de la galaxia. Fueron detectados por primera vez a comienzos de siglo XX en experimentos con elementos

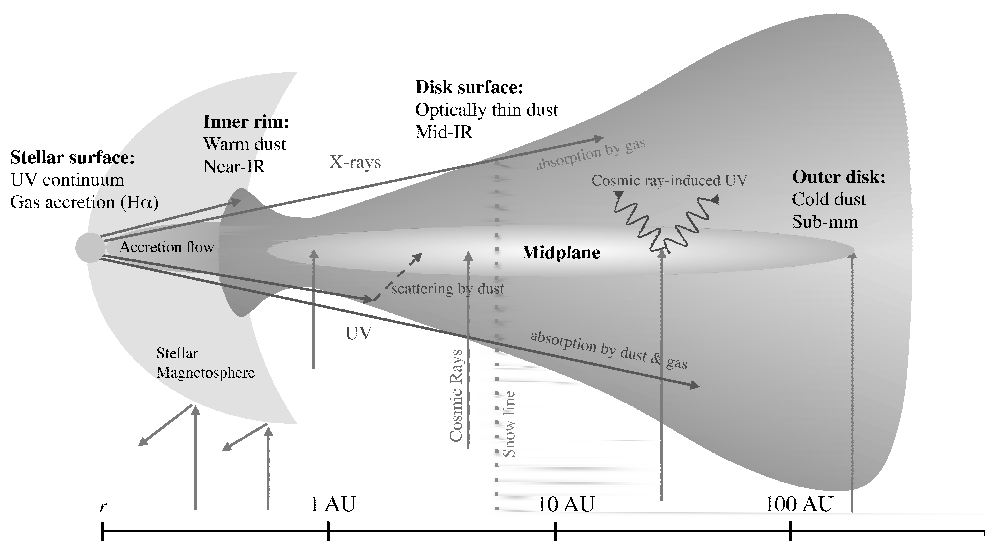


Figura 5.3: Estructura del disco y propiedades de emisión. La estructura química de los discos protoplanetarios puede ser dividida aproximadamente en tres capas. En la superficie del disco, la radiación estelar UV crea una capa caliente ($T > 1000$ K) de especies ionizadas y atómicas (C^+ , C, N, H, O). Debajo de esta capa, se forman moléculas (H_2 , CO, HCN, OH, H_2O , CO_2 , N_2) en el gas y sobreviven gracias a las temperaturas tibias ($T_i < 100$ K). En el plano central frío ($T < 80$ K), muchas especies del gas se condensan sobre granos de polvo (CO, CH_4 , CO_2). Es en esta región donde ocurre la formación de moléculas orgánicas simples detectadas en cometas (CH_4 y H_2CO). Figura basada en Dullemond & Monnier (2010).

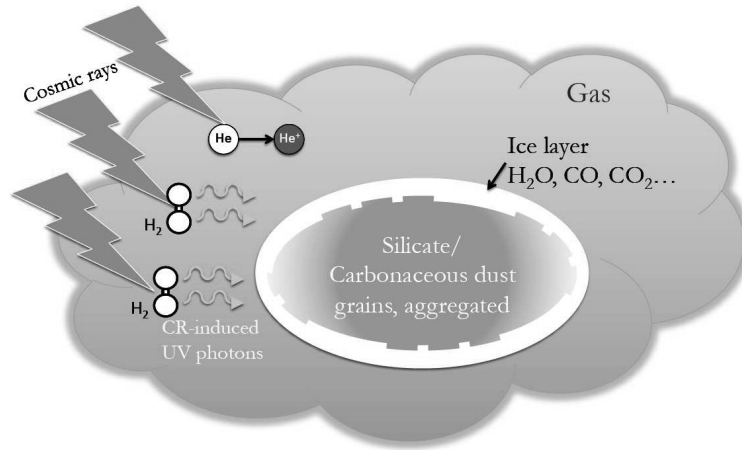


Figura 5.4: Gas, polvo y procesos inducidos por rayos cósmicos en el plano central de los discos protoplanetarios

radioactivos, cuando eventos de ionización ocurrieron al no haber muestras radiactivas presentes en la cámara experimental. En su mayoría son protones y núcleos atómicos, y su promedio de energía cinética es del orden de 1 GeV por nucleón. En discos protoplanetarios, se espera que jueguen un rol significativo en la ionización del material del disco y del calentamiento del gas. Estudiando cómo los rayos cósmicos afectan la evolución química en el plano central de los discos nos da una idea de cómo los hielos, y en particular las especies orgánicas son formadas en discos protoplanetarios.

Esta tesis

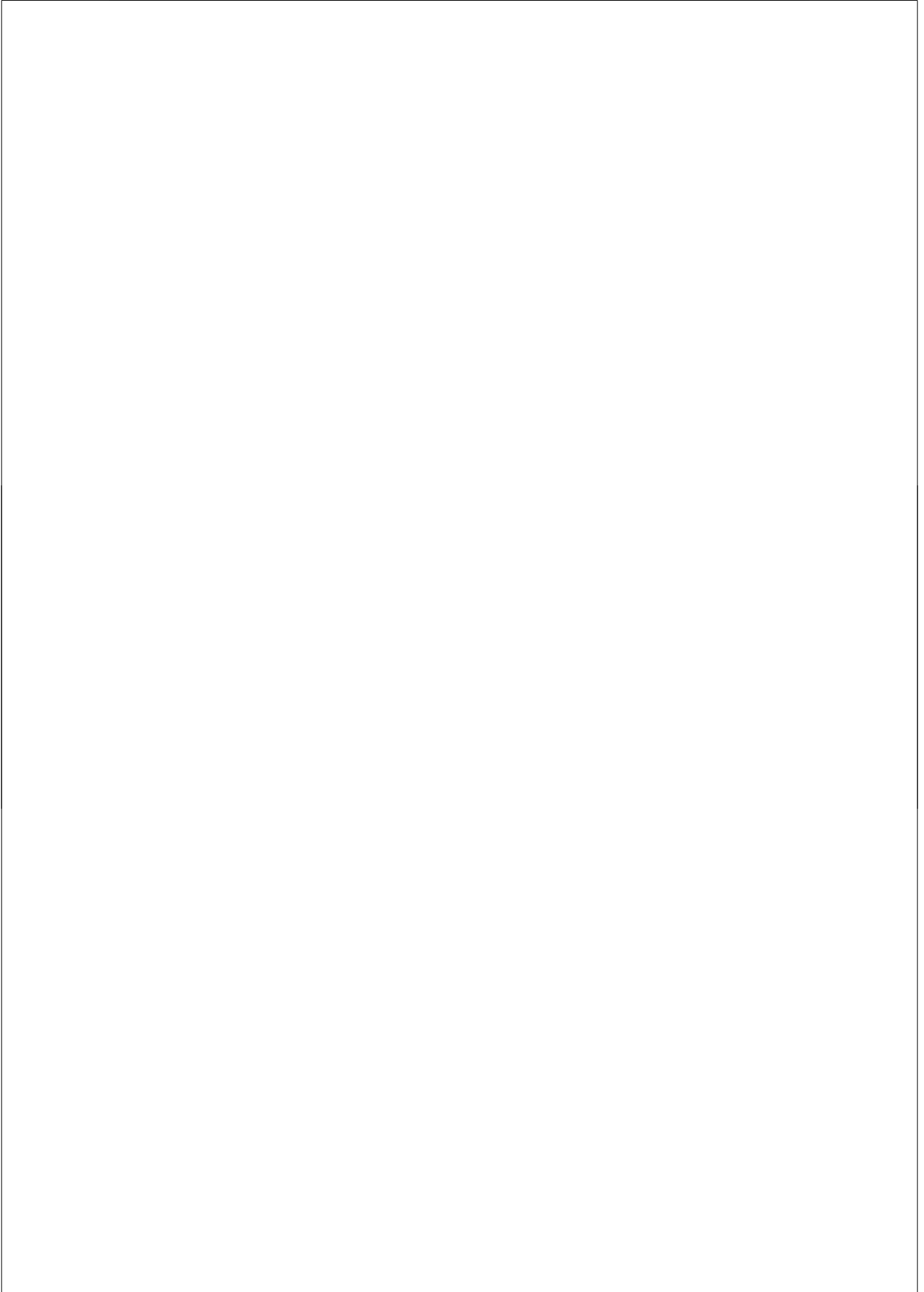
En esta tesis buscamos constreñir las condiciones químicas en el Sistema Solar temprano, analizando modelos de evolución química de discos protoplanetarios, comparándolos con el conocimiento actual de la composición fisicoquímica de cuerpos del Sistema Solar, como lo son los cometas. Para llegar a esto, requerimos modelos hidrostáticos y de transferencia radiativa para establecer la temperatura local, densidad y campo de radiación en el cual la química gas/grano evoluciona. La región de formación de planetas (y cometas) en los discos coincide con el plano medio, el cual está dominado por rayos cósmicos. Por esta razón también nos enfocamos en investigar el rol de los procesos inducidos por rayos cósmicos en la evolución química (Figura 4).

En el Capítulo 2 (Chaparro Molano & Kamp 2012a), presento un análisis temporal de la química gas/grano en regiones frías y pobres en gas en discos protoplanetarios. En este capítulo presento un método para estimar el efecto del campo UV inducido por rayos cósmicos. En particular, calculamos las tasas de fotoprocesos inducidos por rayos cósmicos de una manera consistente con la extinción del polvo. Encuentro que las condiciones térmicas en la región del plano central del disco a distancias radiales mayores que 10 UA en nuestro modelo son ideales para la formación de hielos cuya composición coincide con las abundancias cometarias observadas.

En el Capítulo 3 (Chaparro Molano & Kamp 2012b) exploro la evolución química de regiones ricas en gas de los discos protoplanetarios. Mejoro el cálculo de las tasas de fotoprocesos inducidos por rayos cósmicos del capítulo 2 incluyendo los efectos de extinción causada por el gas. Encuentro que la opacidad en las regiones ricas en gas del plano central del disco ($r < 10$ UA) es casi el 30% del total de la opacidad. También encuentro que CO, CO₂, SiO y OH son los principales contribuyentes en el gas de la extinción de UV generados por rayos cósmicos.

En el Capítulo 4 extiendo el método de cálculo para las tasas de fotoprocesos inducidos por rayos cósmicos desarrollado en los primeros dos capítulos para un modelo de disco bidimensional. Estudio los efectos de dichos fotoprocesos en la evolución química de especies en el gas y hielo, y encuentro que los modelos químicos de estado estacionario subestiman las abundancias de algunas especies en el hielo. También discuto la posibilidad de atrapar especies en el hielo que son formadas en etapas tempranas de la evolución de los discos. Esto ocurre en la capa más cercana a la superficie del grano de polvo, formando así un manto de hielo estratificado.

En el Capítulo 5 me enfoco en la formación por capas de hielos en la superficie de granos de polvo esféricos. Encuentro que en la mayoría de las regiones del plano central del disco, hay un manto primario de hielos que tiene un grosor de ~300 monocapas. A 30 UA, un manto de hielo secundario hace crecer el manto de hielo primario hasta alcanzar el doble de su tamaño. El crecimiento de este manto contribuye a incrementar el tamaño de granos de polvo, que puede crecer típicamente de un radio de 0.2 μm a casi 0.4 μm . Tal modificación en la función de distribución de grano impactará las opacidades del polvo (que dependen del perfil térmico del plano central) y la eficiencia de coagulación del polvo.



Bibliography

- Abgrall, H., Roueff, E., & Drira, I. 2000, *A&AS*, 141, 297
- Agol, E., Steffen, J., Sari, R., & Clarkson, W. 2005, *MNRAS*, 359, 567
- Agúndez, M., Goicoechea, J. R., Cernicharo, J., Faure, A., & Roueff, E. 2010, *ApJ*, 713, 662
- A'Hearn, M. F., Feaga, L. M., Keller, H. U., et al. 2012, *ApJ*, 758, 29
- Aikawa, Y. 2007, *ApJ*, 656, L93
- Aikawa, Y., Umebayashi, T., Nakano, T., & Miyama, S. M. 1997a, *ApJ*, 486, L51+
- . 1997b, *ApJ*, 486, L51+
- . 1999, *ApJ*, 519, 705
- Aikawa, Y., van Zadelhoff, G. J., van Dishoeck, E. F., & Herbst, E. 2002, *A&A*, 386, 622
- Allen, M. & Robinson, G. W. 1977, *ApJ*, 212, 396
- Amelin, Y., Krot, A. N., Hutcheon, I. D., & Ulyanov, A. A. 2002, *Science*, 297, 1678
- Andersson, S. & van Dishoeck, E. F. 2008, *A&A*, 491, 907
- Andrews, S. M. & Williams, J. P. 2007, *ApJ*, 671, 1800
- Arasa, C., Andersson, S., Cuppen, H. M., van Dishoeck, E. F., & Kroes, G. 2010, *J. Chem. Phys.*, 132, 184510
- Aresu, G., Kamp, I., Meijerink, R., et al. 2011, *A&A*, 526, A163
- Armitage, P. J. 2010, *Astrophysics of Planet Formation*
- Balbus, S. A. & Hawley, J. F. 1991, *ApJ*, 376, 214
- Bates, D. R. 1986, *ApJ*, 306, L45
- Bergin, E. A., Aikawa, Y., Blake, G. A., & van Dishoeck, E. F. 2007, *Protostars and Planets V*, 751
- Bischoff, A. 2001, *Earth Moon and Planets*, 85, 87
- Blum, J. 2010, *Research in Astronomy and Astrophysics*, 10, 1199
- Bockelée-Morvan, D., Crovisier, J., Mumma, M. J., & Weaver, H. A. 2004, *The composition of cometary volatiles*, ed. Festou, M. C., Keller, H. U., & Weaver, H. A., 391–423
- Bockelée-Morvan, G. 2010, in *Physics and Astrophysics of Planetary Systems*, EAS Publication Series No. 41, 313–324

BIBLIOGRAPHY

- Bouchy, F., Udry, S., Mayor, M., et al. 2005, *A&A*, 444, L15
- Brown, P. N., Byrne, G. D., & Hindmarsh, A. C. 1989, *SIAM J. Sci. Stat. Comput.*, 10, 1038
- Burke, J. R. & Hollenbach, D. J. 1983, *ApJ*, 265, 223
- Calvet, N. & Hartmann, L. 1992, *ApJ*, 386, 239
- Cameron, A. G. W. 1995, *Meteoritics*, 30, 133
- Carr, J. S. & Najita, J. R. 2008, *Science*, 319, 1504
- Cazaux, S., Cobut, V., Marseille, M., Spaans, M., & Caselli, P. 2010, *A&A*, 522, A74
- Cazaux, S. & Tielens, A. G. G. M. 2002, *ApJ*, 575, L29
- . 2004, *ApJ*, 604, 222
- Cecchi-Pestellini, C. & Aiello, S. 1992, *MNRAS*, 258, 125
- Chaparro Molano, G. & Kamp, I. 2012a, *A&A*, 537, A138
- . 2012b, *A&A*, 547, A7
- Charnley, S. B., Tielens, A. G. G. M., & Rodgers, S. D. 1997, *ApJ*, 482, L203
- Cheung, A. C., Rank, D. M., Townes, C. H., Thornton, D. D., & Welch, W. J. 1968, *Physical Review Letters*, 21, 1701
- . 1969, *Nature*, 221, 626
- Chiang, E. I. & Goldreich, P. 1997, *ApJ*, 490, 368
- Chiar, J. E., Adamson, A. J., Kerr, T. H., & Whittet, D. C. B. 1995, *ApJ*, 455, 234
- Collings, M. P., Anderson, M. A., Chen, R., et al. 2004, *MNRAS*, 354, 1133
- Crida, A. 2009, *ApJ*, 698, 606
- Crida, A., Morbidelli, A., & Masset, F. 2007, *A&A*, 461, 1173
- Cuppen, H. M. & Herbst, E. 2007, *ApJ*, 668, 294
- D'Alessio, P., Calvet, N., & Hartmann, L. 2001, *ApJ*, 553, 321
- Davis, C. J. & Eisloffel, J. 1995, *A&A*, 300, 851
- Desch, S. J. 2007, *ApJ*, 671, 878
- Dominik, C., Blum, J., Cuzzi, J. N., & Wurm, G. 2007, *Protostars and Planets V*, 783
- Draine, B. T. & Lee, H. M. 1984, *ApJ*, 285, 89
- Dulieu, F., Congiu, E., Noble, J., et al. 2013, *Nature*.
- Dullemond, C. P. & Monnier, J. D. 2010, *ARA&A*, 48, 205
- Evans, II, N. J., Dunham, M. M., Jørgensen, J. K., et al. 2009, *ApJS*, 181, 321
- Fayolle, E. C., Öberg, K. I., Cuppen, H. M., Visser, R., & Linnartz, H. 2011, *A&A*, 529, A74
- Fedele, D., Pascucci, I., Brittain, S., et al. 2011, *ApJ*, 732, 106
- Fedele, D., van den Ancker, M. E., Henning, T., Jayawardhana, R., & Oliveira, J. M. 2010, *A&A*, 510, A72
- Fegley, Jr., B. 2000, *Space Science Reviews*, 92, 177
- Fuchs, G. W., Cuppen, H. M., Ioppolo, S., et al. 2009, *A&A*, 505, 629
- Galwey, A. K. & Brown, M. 1999, *Thermal decomposition of ionic solids* (Elsevier)

BIBLIOGRAPHY

- Gammie, C. F. 1996, *ApJ*, 457, 355
- Gibb, E. L., Whittet, D. C. B., Boogert, A. C. A., & Tielens, A. G. G. M. 2004, *ApJS*, 151, 35
- Gillett, F. C., Forrest, W. J., & Merrill, K. M. 1973, *ApJ*, 183, 87
- Glassgold, A. E., Najita, J. R., & Igea, J. 2007, *ApJ*, 656, 515
- Goldreich, P. & Ward, W. R. 1973, *ApJ*, 183, 1051
- Gomes, R., Levison, H. F., Tsiganis, K., & Morbidelli, A. 2005, *Nature*, 435, 466
- Gorti, U. & Hollenbach, D. 2008, *ApJ*, 683, 287
- . 2009, *ApJ*, 690, 1539
- Gorti, U., Hollenbach, D., Najita, J., & Pascucci, I. 2011, *ApJ*, 735, 90
- Gould, R. J. & Salpeter, E. E. 1963, *ApJ*, 138, 393
- Graedel, T. E., Langer, W. D., & Frerking, M. A. 1982, *ApJS*, 48, 321
- Gredel, R., Lepp, S., & Dalgarno, A. 1987, *ApJ*, 323, L137
- Gredel, R., Lepp, S., Dalgarno, A., & Herbst, E. 1989, *ApJ*, 347, 289
- Greenberg, R., Bottke, W. F., Carusi, A., & Valsecchi, G. B. 1991, *Icarus*, 94, 98
- Guilloteau, S. & Dutrey, A. 1998, *A&A*, 339, 467
- Gullbring, E., Hartmann, L., Briceno, C., & Calvet, N. 1998, *ApJ*, 492, 323
- Habing, H. J. 1996, *A&A Rev.*, 7, 97
- Haisch, Jr., K. E., Barsony, M., & Tinney, C. 2010, *ApJ*, 719, L90
- Hartigan, P., Edwards, S., & Ghandour, L. 1995, *ApJ*, 452, 736
- Hartmann, L., Calvet, N., Gullbring, E., & D'Alessio, P. 1998, *ApJ*, 495, 385
- Hasegawa, T. I. & Herbst, E. 1993, *MNRAS*, 261, 83
- Hasegawa, T. I., Herbst, E., & Leung, C. M. 1992, *ApJS*, 82, 167
- Hayashi, C. 1981, *Progress of Theoretical Physics Supplement*, 70, 35
- Henning, T. 2008, *Physica Scripta Volume T*, 130, 014019
- Henning, T. & Semenov, D. 2008, in *IAU Symposium*, Vol. 251, *IAU Symposium*, ed. S. Kwok & S. Sanford, 89–98
- Herbig, G. H. 1968, *ZAp*, 68, 243
- Herbst, E. 1993, in *Dust and Chemistry in Astronomy*, ed. T. J. Millar & D. A. Williams (Bristol), 190
- Herbst, E. & Klemperer, W. 1973, *ApJ*, 185, 505
- Herbst, E. & van Dishoeck, E. F. 2009, *ARA&A*, 47, 427
- Hernández, J., Hartmann, L., Calvet, N., et al. 2008, *ApJ*, 686, 1195
- Hogerheijde, M. 1998, PhD thesis, Department of Astronomy, University of California
- Hollenbach, D., Johnstone, D., Lizano, S., & Shu, F. 1994, *ApJ*, 428, 654
- Hollenbach, D., Kaufman, M. J., Bergin, E. A., & Melnick, G. J. 2009, *ApJ*, 690, 1497
- Holloway, W. & Beeby, J. L. 1975, *Journal of Physics C Solid State Physics*, 8, 3531

BIBLIOGRAPHY

- Hueso, R. & Guillot, T. 2005, *A&A*, 442, 703
- Indriolo, N., Geballe, T. R., Oka, T., & McCall, B. J. 2007, *ApJ*, 671, 1736
- Ioppolo, S. 2010, PhD thesis, Ph. D. thesis, University of Leiden (2010)
- Ioppolo, S., Cuppen, H. M., Romanzin, C., van Dishoeck, E. F., & Linnartz, H. 2008, *ApJ*, 686, 1474
- Isella, A., Carpenter, J. M., & Sargent, A. I. 2010, *ApJ*, 714, 1746
- Jenkins, E. B. 2009, *ApJ*, 700, 1299
- Johansen, A., Oishi, J. S., Mac Low, M.-M., et al. 2007, *Nature*, 448, 1022
- Kalas, P., Graham, J. R., Chiang, E., et al. 2008, *Science*, 322, 1345
- Kamp, I. 2011, in *EAS Publications Series*, Vol. 46, *EAS Publications Series*, ed. C. Joblin & A. G. G. M. Tielens, 271–283
- Kamp, I. & Spaans, M. 2012, *Star and Planet Formation*, *Lecture Notes*
- Kelley, M. S. & Wooden, D. H. 2009, *Planet. Space Sci.*, 57, 1133
- Knez, C., Boogert, A. C. A., Pontoppidan, K. M., et al. 2005, *ApJ*, 635, L145
- Lada, C. J. 1987, in *IAU Symposium*, Vol. 115, *Star Forming Regions*, ed. M. Peimbert & J. Jugaku, 1–17
- Lee, H.-H., Bettens, R. P. A., & Herbst, E. 1996, *A&AS*, 119, 111
- Lee, L. C. 1984, *ApJ*, 282, 172
- Leger, A., Jura, M., & Omont, A. 1985, *A&A*, 144, 147
- Li, A. & Mann, I. 2012, in *Astrophysics and Space Science Library*, Vol. 385, *Astrophysics and Space Science Library*, ed. I. Mann, N. Meyer-Vernet, & A. Czechowski, 5
- Lisse, C. M., Wyatt, M. C., Chen, C. H., et al. 2012, *ApJ*, 747, 93
- Lodders, K. & Amari, S. 2005, *Chemie der Erde / Geochemistry*, 65, 93
- Machida, M. N., Inutsuka, S.-i., & Matsumoto, T. 2006, *ApJ*, 649, L129
- Maret, S., Ceccarelli, C., Caux, E., et al. 2004, *A&A*, 416, 577
- McCrea, W. H. & McNally, D. 1960, *MNRAS*, 121, 238
- McKeegan, K. D., Aléon, J., Bradley, J., et al. 2006, *Science*, 314, 1724
- Meeus, G., Montesinos, B., Mendigutía, I., et al. 2012, *A&A*, 544, A78
- Meijerink, R., Aresu, G., Kamp, I., et al. 2012, *A&A*, 547, A68
- Micelotta, E. R., Jones, A. P., & Tielens, A. G. G. M. 2011, *A&A*, 526, A52
- Milosavljević, M. 2008, Master's thesis, University of Belgrade, Faculty of Mathematics
- Min, M., Dullemond, C. P., Kama, M., & Dominik, C. 2011, *Icarus*, 212, 416
- Morbidelli, A., Levison, H. F., Tsiganis, K., & Gomes, R. 2005, *Nature*, 435, 462
- Najita, J. R., Carr, J. S., Strom, S. E., et al. 2010, *ApJ*, 712, 274
- Natta, A., Testi, L., Calvet, N., et al. 2007, *Protostars and Planets V*, 767
- Öberg, K. I., van Dishoeck, E. F., & Linnartz, H. 2009, *A&A*, 496, 281
- Ochkin, V. & Kittell, S. 2009, *Spectroscopy of low temperature plasma* (Wiley-VCH)

BIBLIOGRAPHY

- Ormel, C. W., Cuzzi, J. N., & Tielens, A. G. G. M. 2008, *ApJ*, 679, 1588
- Ormel, C. W., Dullemond, C. P., & Spaans, M. 2010, *Icarus*, 210, 507
- Padovani, M. & Galli, D. 2011, *A&A*, 530, A109
- Papoular, R. 2005, *MNRAS*, 362, 489
- Pinte, C., Harries, T. J., Min, M., et al. 2009, *A&A*, 498, 967
- Pontoppidan, K. M., van Dishoeck, E. F., & Dartois, E. 2004, *A&A*, 426, 925
- Prasad, S. S. & Tarafdar, S. P. 1983, *ApJ*, 267, 603
- Prialnik, D. 1997, *ApJ*, 478, L107
- Pringle, J. E. 1981, *ARA&A*, 19, 137
- Raymond, S. N. 2006, *ApJ*, 643, L131
- Raymond, S. N., Quinn, T., & Lunine, J. I. 2006, *Icarus*, 183, 265
- Riahi, R., Teulet, P., Ben Lakhdar, Z., & Gleizes, A. 2006, *Eur. Phys. J. D*, 40, 223
- Roberts, J. F., Rawlings, J. M. C., Viti, S., & Williams, D. A. 2007, *MNRAS*, 382, 733
- Semenov, D., Hersant, F., Wakelam, V., et al. 2010, *A&A*, 522, A42
- Semenov, D. & Wiebe, D. 2011, *ApJS*, 196, 25
- Semenov, D., Wiebe, D., & Henning, T. 2004, *A&A*, 417, 93
- Shakura, N. I. & Sunyaev, R. A. 1973, *A&A*, 24, 337
- Shaw, A. M. 2006, *Astrochemistry: From Astronomy to Astrobiology*
- Shen, C. J., Greenberg, J. M., Schutte, W. A., & van Dishoeck, E. F. 2004, *A&A*, 415, 203
- Shu, F. H., Adams, F. C., & Lizano, S. 1987, *ARA&A*, 25, 23
- Smith, B. A. & Terrile, R. J. 1984, *Science*, 226, 1421
- Smith, I. W. M., Herbst, E., & Chang, Q. 2004, *MNRAS*, 350, 323
- Snyder, L. E., Buhl, D., Zuckerman, B., & Palmer, P. 1969, *Physical Review Letters*, 22, 679
- Solomon, P. M. & Klemperer, W. 1972, *ApJ*, 178, 389
- Stahler, S. W. & Palla, F. 2005, *The Formation of Stars*
- Stantcheva, T., Shematovich, V. I., & Herbst, E. 2002, *A&A*, 391, 1069
- Sternberg, A. & Dalgarno, A. 1995, *ApJS*, 99, 565
- Sternberg, A., Dalgarno, A., & Lepp, S. 1987, *ApJ*, 320, 676
- Suzuki, T. K. & Inutsuka, S.-i. 2009, *ApJ*, 691, L49
- Taquet, V., Ceccarelli, C., & Kahane, C. 2012, *A&A*, 538, A42
- Teixeira, P. S., Zapata, L. A., & Lada, C. J. 2007, *ApJ*, 667, L179
- Thi, W.-F., Woitke, P., & Kamp, I. 2011, *MNRAS*, 412, 711
- Tielens, A. G. G. M. 2005, *The Physics and Chemistry of the Interstellar Medium*
- Tielens, A. G. G. M. & Hagen, W. 1982, *A&A*, 114, 245
- Tsiganis, K., Gomes, R., Morbidelli, A., & Levison, H. F. 2005, *Nature*, 435, 459
- Umeyashi, T. & Nakano, T. 1981, *PASJ*, 33, 617

BIBLIOGRAPHY

- van Dishoeck, E. F., Jonkheid, B., & van Hemert, M. C. 2006, *Faraday Discussions*, 133, 231
- van Zadelhoff, G.-J., van Dishoeck, E. F., Thi, W.-F., & Blake, G. A. 2001, *A&A*, 377, 566
- Visser, R. 2009, PhD thesis, Ph. D. thesis, University of Leiden (2009)
- Visser, R., Doty, S. D., & van Dishoeck, E. F. 2011, *A&A*, 534, A132
- Visser, R., van Dishoeck, E. F., Doty, S. D., & Dullemond, C. P. 2009, *A&A*, 495, 881
- Wakelam, V., Herbst, E., Loison, J.-C., et al. 2012, *ApJS*, 199, 21
- Wakelam, V., Smith, I. W. M., Herbst, E., et al. 2010, *Space Sci. Rev.*, 156, 13
- Walsh, C., Millar, T. J., & Nomura, H. 2010, *ApJ*, 722, 1607
- Walsh, C., Nomura, H., Millar, T. J., & Aikawa, Y. 2012, *ApJ*, 747, 114
- Watanabe, N. & Kouchi, A. 2002, *ApJ*, 571, L173
- Weidenschilling, S. J. 1977, *Ap&SS*, 51, 153
- . 1980, *Icarus*, 44, 172
- Weingartner, J. C. & Draine, B. T. 2001, *ApJ*, 548, 296
- Whittet, D. C. B., Gerakines, P. A., Tielens, A. G. G. M., et al. 1998, *ApJ*, 498, L159
- Whittet, D. C. B., Shenoy, S. S., Bergin, E. A., et al. 2007, *ApJ*, 655, 332
- Willacy, K., Klahr, H. H., Millar, T. J., & Henning, T. 1998, *A&A*, 338, 995
- Willacy, K. & Woods, P. M. 2009, *ApJ*, 703, 479
- Williams, D. A., Hartquist, T. W., & Whittet, D. C. B. 1992, *MNRAS*, 258, 599
- Williams, J. P. & Cieza, L. A. 2011, *ARA&A*, 49, 67
- Wilson, R. W., Jefferts, K. B., & Penzias, A. A. 1970, *ApJ*, 161, L43
- Woitke, P., Kamp, I., & Thi, W. 2009, *A&A*, 501, 383
- Woodall, J., Agúndez, M., Markwick-Kemper, A. J., & Millar, T. J. 2007, *A&A*, 466, 1197
- Woolfson, M. M. 1993, *QJRAS*, 34, 1
- Wulf, T. 1909, *Phys. Zeit*, 1, 152

Acknowledgments

The free soul is rare, but you know it when you see it - basically because you feel good, very good, when you are near or with them.
— Charles Bukowski, *Tales of Ordinary Madness* —

I think I should start from the beginning. 17 years ago, my dad and I were working on an art project for school, when a power outage interrupted us. During the outage, we had what I think was our first adult conversation. We talked about life, the future, but most importantly, we talked about science. My dad was convinced that physics was the path to understanding the world while acquiring the skills necessary to make it big in life. I'm not sure he was right, but that conversation resonated with me. It helped that he fostered my interest in science by buying me every Carl Sagan book that we could get our hands on. About a year later he died, and I was suddenly confronted with my future. So I decided to follow my dad's advice and study physics, and later astronomy.

Even when there's a strong driving force behind the pursuit of a dream, it's no easy task to avoid becoming jaded and cynical as the years go by. Fortunately, this pursuit was not a one man job. In particular, this thesis, which represents the culmination of the labor of four years, could not have come to fruition without the support of a host of wonderful people.

First and foremost, I want to thank Inga for being such an amazing advisor all these years. The realization of this research project was made possible by your dedication, steadfastness, and passion for science. All our scientific discussions were very en-

Acknowledgments

joyable, and you always had time for me when I got confused or steered off-track. Your feedback was always honest, constructive, and respectful. I am proud to have been part of your research group, and I'm looking forward to future collaborations. Thanks for being so welcoming and open to me and my family, and for helping me so much on a personal level when I was feeling low. Of course, I'm also thankful for all the great BBQs at your place: you and Uli make the best burgers this side of the Atlantic!

I want to extend my thanks to the members of the Protoplanetary Disk research group: Giamba, Linda, Rosina, Antonio, Stefano, and Silvia. I wish you guys all the best in your future endeavors. Same goes to Stéphanie and her group: Seyit and Leon: thanks for all the interesting "dusty" conversations we had. Leon, thank you so much for translating my summary into Dutch, and sorry for the long sentences!

The ISM group meetings have been a great venue for sharing ideas and learning from other people's work. Besides all present and past members of the ISM group, I want to specially thank all who have served as chairpersons: Matthijs, Seyit, Aycin, Giamba, Rowin and Leon. You guys have done a great job in keeping the group active and fun.

I am especially grateful to the reading committee for taking the time for reading my thesis and for their feedback: Harold Linnartz, Tom Millar, and Marco Spaans.

My thanks also go to a few people who were close to my research project and/or gave me helpful advice at some point or another during the PhD: Wing-Fai Thi, Peter Woitke, Stéphanie Cazaux, and Andrés Carmona.

I want to thank everybody who contributed to the logistics of this research project. Traveling to conferences and workshops was facilitated by LKBF and the Kapteyn Institute. The help provided by the Kapteyn support staff has been invaluable. My thanks go to Hennie, Jackie, Gineke, Christa, and Lucia, and to the computer support team of Wim, Eite, and Martin for all the help and for being super-patient to newbie PhD students such as myself.

I'd like to thank my colleagues at the Kapteyn Institute. You guys make the Institute a great working environment, conducive to good science and good fun. If I forget any of you please don't hold it against me! Old timers Facu, Anto, Jonathan, Beike, Matías, Boris, Peter, Juan Pablo, Aycin, Yanping, Parisa, Oscar, Esra - thanks for welcoming me into your ranks and making lunch, breaks, and in general, daily life at the Institute a very pleasant experience. Same goes to those who came after me: Zsofia, Burcu, Anastasia, Marius, Ajinkya, Aleksandar, Giacomo - I wish you the best of luck with your theses.

Andrea, Carlos, Harish: happy hours and apple/coffee/mate/smoke breaks wouldn't have been nearly half as fun if you three nerds hadn't been around. I'm really glad I was able to share so many laughs, so many conspiracy theories, so many South Park

references throughout these four years. My hat goes off to you gentlemen, it's been a pleasure!

Andrea, Dr. Cum Laude, when I first met you I thought you were a total jerk! Anyway, I want to thank you for being there and supporting me during so many happy and sad moments in my life in the past few years. Congratulations and best of luck with your new life with Claudia. Thanks for being my bro, bro.

Carlos, parcero, I can only hope that some of your work ethics and wicked sense of humor have rubbed off on me. How can I thank you for being such a good friend without sounding *gaaaay*? You know what? I don't care. I love you, man!

Harish, I could always count on you for making light of even the most serious of issues. Thanks, I guess? No, but seriously, your lightheartedness has really gotten me through some tough times. I'm really looking forward to seeing how uncomfortable you'll be while wearing the paranymph garb! And Iva, sorry for being such a bad influence on your hubby! But thanks for letting us borrow him for our weekdays shenanigans. Guys, thanks for all the delicious indo-bulgarian dinners and for being such good pals.

Giamba, first of all I want to thank you for being so patient with my snoring at all those conferences. You're a saint! Thanks for being such a cool travel partner. I wish you the best in your new life with Ada.

Maarten, I couldn't have asked for a better officemate. Throughout all the shared experiences of the PhD I could always count on you to hear me out when I wanted to vent, and you were always there to raise my spirits with a funny piece of news, a new gadget that you'd just bought, or a ridiculous Youtube video. Congrats on your new house, and good luck with your thesis!

Guobao, I have a bone to pick with you for making me look like a religious nut in your thesis acknowledgments. I want to set the record straight! However, I do want to thank you for being an all-around cool guy.

Koshy, you have mastered the art of being friends with anything that moves: you even bagged Carlos! That is no simple feat. Good luck with your career and with your arranged marriage that for some reason you keep denying.

Paolo, thanks for tolerating me and Andrea's often off-putting sense of humor. Congratulations on you beautiful family, and I wish you, Jenny, and Marco the brightest of futures.

Teresa, gracias por las cenas y asados compartidos. Oscar, gracias a (o a pesar de) tu particular sentido del humor, hemos tenido muy buenas conversaciones. A los dos les deseo buena suerte en su vida futura en Holanda.

Mariano, aunque no interactuamos a un nivel científico, he aprendido mucho de ti. Tu trato con tus estudiantes, y en general con los estudiantes del instituto es ejemplar. Te deseo lo mejor para el futuro, "con un ojo puesto en la historia y otro en el presente

Acknowledgments

y otro en el porvenir”.

To the steadfast members of the happy hour crew: Pratyush, Mark, Nancy, Katinka, Jan, Federico, Federico, and Robyn - thanks for all the fun, and see you at the AA meetings!

I also want to thank my friends from Leiden who opened the doors of their homes to me and my family: Christoph, Elisa, Fede, Lara, Juan. I hope I can do the same for you in the future.

Lucasito, nene querido, mugre vanidoso. Gracias por las visitas, las piedras, los Amsterdamer y Le Pantalon. Le dejo una cancioncita. *Mes amis étaient plein d'insouciance, mes amours avaient le corps brûlant, mes emmerdes aujourd'hui quand j'y pense, avaient peu d'importance, et c'était le bon temps!*

Ruben, Fabián, Carlos, gracias por su gran apoyo en los momentos más difíciles, y por siempre recibirme en Bogotá con tanto afecto.

Osaka, Jen, gracias por las visitas y por consentirnos tanto cuando vamos a Bogotá.

Alejandro, Elena, gracias por todo el apoyo, el cariño, las buenas cenas y las tertulias. Los voy a extrañar, chicos.

Isis, Vanesa, extrañare mucho tantas noches de rajás, sopas, rancheras, cumbias y tequila. Gracias por acompañarnos todo este tiempo en Groningen.

Doc, Javier, muchas gracias por todo el apoyo que nos han dado y por recibirnos en su hogar, sea en Bogotá, Medellín o Groningen, siempre nos han consentido mucho. Gracias a ustedes también conocimos a muchos buenos amigos a quien también quiero agradecer por estar muy cerca de mi familia y por apoyarnos: Jeanette y César, Noelia y Jason, Gemma y Edu. Alberto y Esther, felicitaciones por esa nena tan hermosa que es Clarita. También quiero agradecer a André y a Simona por ser tan buenos compañeros de juego de Violeta. ¡Pórtense bien con sus papás!

Al parche colombiano en Groningen: Mayer, Vicky, Manu, Daniel, Andrés, David, Alejandro, Gabriela, Catalina (y por extensión Raúl), Silvia, Sara, Juana, Johana, y Gabriela, gracias por mantener unida la comunidad de estudiantes colombianos y por tantas fiestas bacanas.

¡Cómo no voy a agradecer a los muchachos de Física, que prácticamente me criaron! Carolina, Oscar, ustedes han sido mis amigos incondicionales por más de quince años. Gracias por tenerme tanta paciencia y por todas las visitas mutuas entre Groningen y Bruselas. Extiendo mi gratitud por los largos años de amistad a Robin y Nancy, por los paseos a Girardot, por los asados, por las visitas a Leiden y Groningen, y por recibirnos con tanto cariño en París. Gabriel, Andrea, gracias por sus visitas y por estar tan pendientes de nosotros. Mauricio, a pesar de tantos agarrones (virtuales y reales) tan horribles me alegra poder seguir contando con usted a través de la distancia. Arturo, a pesar de que hace mucho tiempo no nos vemos, agradezco

mucho su apoyo en los momentos difíciles. Harol, estas líneas no me alcanzan para agradecer todos estos años de amistad incondicional. Gracias por estar al lado de mi mamá cuando las circunstancias no permitieron que yo estuviera presente. Gracias infinitas por acompañarme, a mí y a mi familia en los momentos más duros.

Quiero agradecer a toda mi familia por el cariño que me han dado. En especial agradezco a mi tía Bernarda por su entrega y devoción por mis papás, por mí, por Adriana y por Violeta. Este trabajo también va dedicado a ella. Margarita, gracias por ser tan buena hija con mi mamá y con mi tía. Nancy, Rodrigo, gracias por recibirme con cariño en Barcelona tantas veces. Espero algún día poder ir con toda la familia.

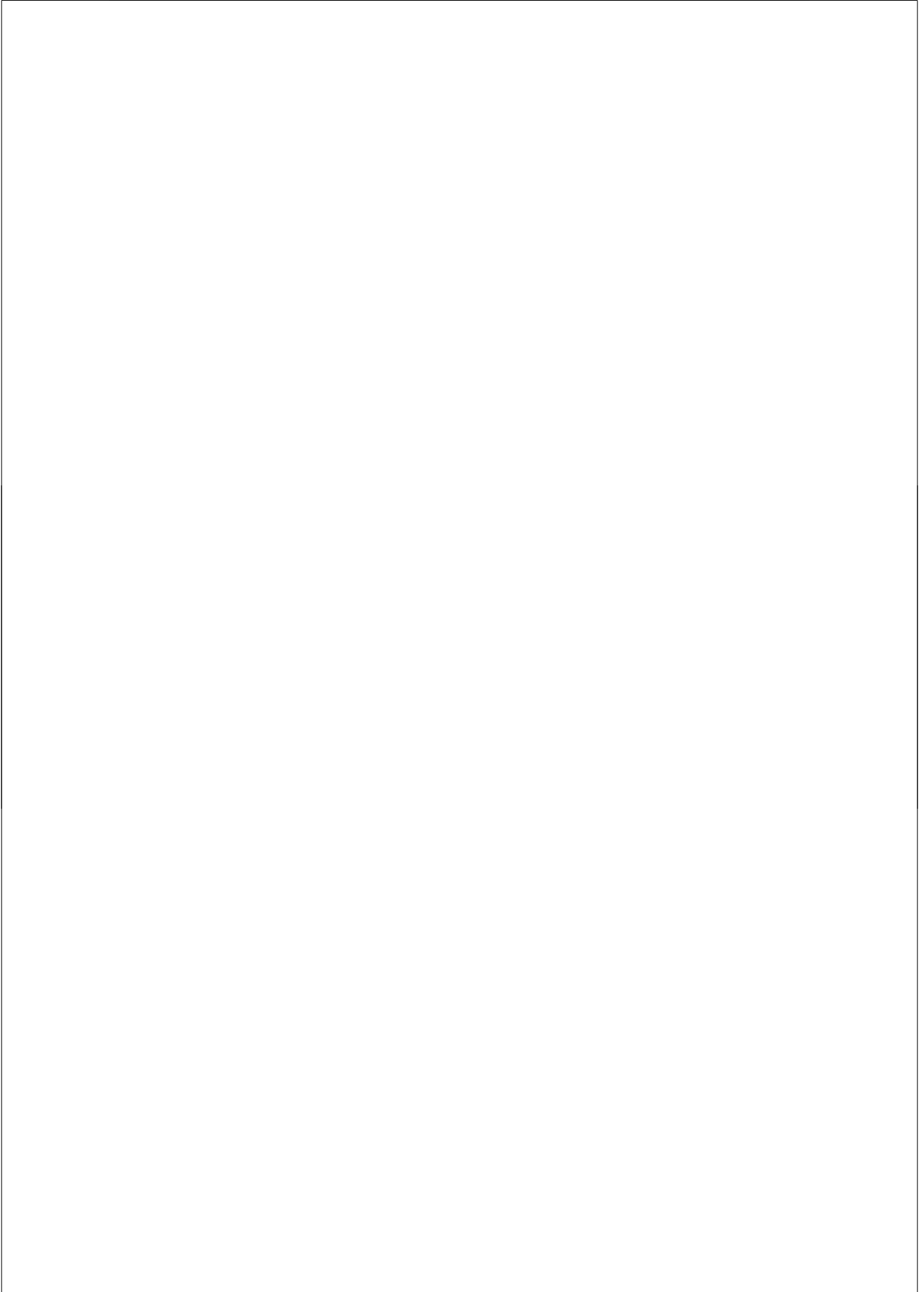
Gonzalo, Nubia, gracias por ser tan buenos suegros, papás y abuelos. Gracias por acogerme como a un hijo dentro de su hogar. Gracias por todo el apoyo, por el cariño, y por supuesto, por Adriana. Gonzo, gracias por visitarnos y por ser tan buen tío de Violeta. ¡Ya casi seremos vecinos!

Mamá, papá, aunque ustedes nunca van a leer estas líneas, quiero agradecerles por enseñarme a amar sin límites, a disfrutar la vida y a salir adelante sin importar las circunstancias. Sus vidas y su hogar lleno de amor son legados más valiosos que cualquier cosa material. Papá, me enseñaste a aventurar, a viajar y a darle prioridad a la vida familiar. Mamá, tu me diste y me sigues dando fuerzas para seguir adelante. Este hogar que tengo lo debo a tus enseñanzas y a tu ejemplo.

Violeta, mi chiquimuñecabebé, eres un rayito de sol que me enamora todos los días. Sigue siendo tan hermosa y tan carepuchi siempre.

Adriana, eres mi sol, mi hogar, mi vida. Este trabajo y esta vida que hemos armado juntos te los debo a ti. Una noche en Tibasosa te dije que estar contigo es como un sueño, y tú me contestaste: “entonces es un sueño bonito”. Por todos los años que nos queden, quiero seguir soñando, contigo a mi lado.

Germán Chaparro Molano
Groningen, April 2013.



your life is your life
don't let it be clubbed into dank submission.
be on the watch.
there are ways out.
there is a light somewhere.
it may not be much light but
it beats the darkness.
be on the watch.
the gods will offer you chances.
know them.
take them.
you can't beat death but
you can beat death in life, sometimes.
and the more often you learn to do it,
the more light there will be.
your life is your life.
know it while you have it.
you are marvelous
the gods wait to delight
in you.

The Laughing Heart, Charles Bukowski

